Studies of various alkali metal oxides containing calcium silicate glasses as substrate for solar cell application

A

Thesis

Submitted for the partial fulfilment

of the requirements for the award of degree of

Doctor of Philosophy

By

Neetu Bansal
(Registration No. 901512005)

Under the supervision of

Dr. Kulvir Singh
(Professor & Associate Dean R&SP)

&

Dr. Bhaskar Chandra Mohanty
(Associate Professor)

THAPAR INSTITUTE
OF ENGINEERING & TECHNOLOGY
(Deemed to be University)

School of Physics and Materials Science

Thapar Institute of Engineering & Technology,

Patiala-147004 (Punjab), India

(Deemed to be University)

(November-2020)

Declaration

I hereby declare that the work which has been presented in the thesis entitled ***"Studies of various alkali metal oxides containing calcium silicate glasses as substrate for solar cell application"*** *is an authentic record of my own research work carried out for the partial fulfilment of the requirements for the award of the degree of Doctor of Philosophy in School of Physics and Materials Science, Thapar Institute of Engineering & Technology (Deemed to be University), Patiala (Punjab), India under the supervision of* ***Dr. Kulvir Singh*** *And* ***Dr. Bhaskar Chandra Mohanty****. The matter submitted in this thesis has not been submitted in part or full in any other university or institute for the award of any degree.*

Date: 26/11/2020
Place: Patiala

Neetu Bansal
(901512005)

This is certified that the above statement made by the candidate is correct and true to the best of my knowledge and belief.

Dr. K. Singh
Professor & Associate Dean R&SP

Dr. Bhaskar C. Mohanty
Associate Professor

School of Physics and Materials Science
Thapar Institute of Engineering & Technology
(Deemed to be University)
Patiala-147004 (Punjab), India.

Dedicated

To My

Husband &

My Darling Son

Acknowledgement

The Doctorate of Philosophy is a journey of lifetime where not only intellectual, but spiritual as well as emotional grooming of the being is accomplished. This realization is incomplete without the surrounding aura of the magnificent people around you, who contribute in one way or the other to nurture you into a better person. This day has arrived after immense waiting that I got the opportunity to express my gratitude towards everyone who stood by my side in the course of this realization.

First and foremost, I am deeply indebted to my supervisors, ***Dr. Kulvir Singh*** *and* ***Dr. Bhaskar Chandra Mohanty****, who have guided me through the ups and downs in this entire journey of never-ending learning. Their deep understanding, motivation and personal attention has provided a smooth base throughout the tenure of PhD. They have helped me to bestow a better shape to my complete work into a dissertation.* ***Dr. Kulvir Singh,*** *my Guruji, like a father has always motivated me towards a better understanding of the concepts and problems through his solution-oriented techniques. His noble thoughts and conviction has lead me to perform well throughout my journey. The heuristic approach of* ***Dr. Bhaskar Chandra Mohanty*** *entailed me to the analytical thinking, enabling me to grasp the rich complexity of concepts. His capacity to combine with an immediate empathy and commitment towards co-workers and others engaged in struggle will always inspire me.*

The track to my doctorate glazed with the financial assistance from Project under Women Scientist Scheme ***(SR/WOS-A/PM-88/2016)****, Department of Science & Technology, Govt. of India. I heartfully appreciate this initiative of GOI to empower Women Scientists struggling through their individuality. Help from various research and academic institutions is highly acknowledged which provided their facilities to carry out the characterisation of materials such as* ***Panjab University, CSIO, IIT Roorkee, IIT Kanpur, NPL Delhi, UGC-DAE CSR Indore.***

I take the privilege to thank ***Dr. Prakash Gopalan*** *(Director), Thapar Institute of Engineering & Technology, Patiala for providing me resources in the institution and needful help during various stages of my work. I am thankful to* ***Dr. Rafat Siddique*** *(Dean R&SP) and* ***Dr. Om Prakash Pandey*** *(HSPMS) for their whole-hearted support and blessings. I thank my IRB Committee members,* ***Dr. Neetu Singh, Dr. Puneet Sharma and Dr. S.D. Tiwari*** *for their helpful suggestions and comments during my progress presentations. I whole-heartedly thank* ***Dr. Manoj Kumar Sharma****,* ***Dr. Bhupendra Chudasama, Dr. D.P. Singh, Dr. Somendu Jana*** *and all the faculty members of SPMS for their timely help, guidance and moral support through different phases of this journey.*

I sincerely thank ***Mr. Purshottam Kumar Singh*** *for his valuable suggestions and help at the technical front of sample preparation and characterization. A special word of thanks goes to* ***Mr. Pardeep Kumar, Mr. Vijay, Ms. Neelam Sadana, Mr. Jant Singh, Mr. Indermani Mishra, Mr. S.P. Verma, Mr. Lalji Verma*** *and* ***Ms. Amandeep Kaur*** *for their valuable official and technical support.* ***Ms. Era, Mr. Ghamshyam Maurya, Mr. Mukesh Aggarwal*** *and* ***Mr. Pardeep Bhatia*** *of SAI Labs, TIET, Patiala for their help and services in carrying out the characterizations.*

I specially thank ***Mrs. Kusum Singh*** *and* ***Mrs. Sanjukta Pradhan*** *for their constant moral support and motivation. I cannot forget the motivation and passion for research instilled in me by* ***Prof. Devinder Mehta,*** *and* ***Mr. Girish Chandra Mohanta,*** *which gave me the courage to begin this journey. Their blessings and zeal for hard work has always enlightened my path.*

I express my immense gratitude towards my seniors and mentors ***Dr. Gurbinder Kaur*** *and* ***Dr. Satwinder Singh*** *for holding my hand while taking initial steps to the world of research with their moral support and guidance in developing attitude for research.* ***Dr. Pooja Singla, Dr. Parveen Jha, Dr. S.K. Arya*** *and* ***Dr. Devender Kumar*** *have always provided their guidance in difficult situations evolving through this journey.*

This journey of dissertation would have been terrible without the unlimited support, valuable discussions and suggestions from my friends and colleagues ***Dr. Indu Gupta, Dr. Gaurav Sharma, Shivani Jindal, Savidh Khan, Kaushlendra Pandey and Santhosh Kumar Mahadevan.*** *Without their help this work could never be completed. I would like to thank* ***Shivani Punj, Jyoti Jhangra, Shivi Kalra, Paramvir Kaur, Manmeet Kaur, Trisha Walia, Taranvir Kaur*** *and* ***Vimi Dua*** *for creating a conducive environment in the holy place of work (our Ceramic Research Lab and Thin Film Lab). I cannot forget the extreme love and help that I got from my contemporary research fellows,* ***Dr. Ayush Gupta, Chhavi Pahwa, Dr. Amandeep Kaur, Piyush Sharma, Dr. Mir Rameez, Shivani Bansal, Raveena Chaudhary, Rishu Arora, Pallavi Gupta*** *and many others.*

My train friends ***Lt. Ms. Charanjeet Kaur, Ms. Pardeep Kaur, Ms. Nishi Seth, Ms. Sunita, Ms. Rama, Ms. Inder, Ms. Amandeep Kaur, Ms. Mamta, Ms. Manpreet Kaur, Ms. Harpreet Kaur, Dr. Rajvir Kaur, Ankita*** *and our little heart* ***Tanvir Kaur*** *have always made my daily four hour immensely tiring journey cheerful and fun-filled, which always relaxed and energized me to work harder on each front.*

I whole-heartedly with immense gratitude dedicate my thesis to my loving and caring family without whom I could not reach this point in my life. I express my sincere devotion to my father(in-law) ***Sh. Rajinder Pal Garg*** *and my mother(in-law)* ***Smt. Sunita Rani*** *who always lived each day from beginning till completion with a dream of their daughter (-in-law)getting a degree of Doctorate.*

Their blessings have left no stone unturned in my path of research. Parents can never be thanked in words. Prayers and sacraments of my grandfather ***Lt. Sh. Kidar Nath Bansal,*** *parents* ***Sh. Khushwant Rai Bansal*** *and* ***Smt. Kiran Bansal*** *have always enlightened my path of life. Love and support of my brothers* ***Mr. Manav Bansal*** *and* ***Dr. Rajnish Garg****, my sisters (-in-law)* ***Ms. Ruchika Bansal, Ms. Monika Garg*** *and* ***Ms. Anjana Bala*** *have always motivated me to keep on moving.*

I do not find enough words to express immense appreciation for my husband ***Er. Rajan Garg,*** *who devoted each day to me, taking care of the complete family and my darling son in my absence. He has always stood as a pillar by side, never letting me fall down, in the toughest times. He has lived every "happy n hard" moment during this journey with me each single day. Rather than thanking, I profoundly apologize to my son* ***Dhairya Garg*** *and my niece* ***Sanchi Garg,*** *for not being with them, when they needed me the most. I lost all their childhood memories in this endeavour towards accomplishing a Doctorate. Today Dhairya has grown so sensible that he, instead, pampers me in the tough times. Both the father-son duo has been angels in my life cheering me through all odds, standing on the other side waiting for me to reach my destination.*

Besides this, several near and dear friends & relatives have helped me in successful completion of this work. It is impossible to name everyone in the limited words. I humbly apologize for the same. I whole-heartedly thank every person who is not mentioned above, but contributed to my thesis in one or the other way.

Above all! I thank the ***Almighty*** *beneath the blue sky, Who always empowered me with His heavenly blessings, and made me feel His presence every time I felt low!!!*

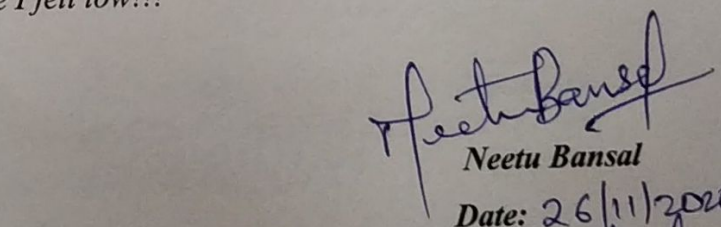

Neetu Bansal

Date: 26/11/2020

Place: Patiala

List of publications

Publications from thesis

1. **Neetu Bansal**, Kaushlendra Pandey, K. Singh, Bhaskar C. Mohanty, "Growth control of molybdenum thin films with simultaneously improved adhesion and conductivity via sputtering for thin film solar cell application", Vacuum 161 (2019) 347-352. https://doi.org/10.1016/j.vacuum.2018.12.050 **(2.515)**

2. **Neetu Bansal**, Bhaskar C. Mohanty, K. Singh, "Designing composition tuned glasses with enhanced properties for use as substrate in Cu_2ZnSnS_4 based thin film solar cells", Journal of Alloys and Compounds 819 (2020) 152984. https://doi.org/10.1016/j.jallcom.2019.152984 **(4.175)**

3. **Neetu Bansal,** Mukul Gupta, Bhaskar C. Mohanty, K. Singh, "Evaluating the role of composition and local structure on alkali out-diffusion in glasses for thin film solar cells," Journal of American Ceramic Society (2020) 1-9. https://doi.org/10.1111/jace.17491 **(3.502)**

4. **Neetu Bansal,** Bhaskar C. Mohanty, K. Singh**,** "Modelling the diffusion of alkali ions from synthesized and commercially available soda lime silicate glasses to Mo-thin film: a comparative study," (communicated)

Other SCI Publications

5. **Neetu Bansal**, Girish C. Mohanta, K. Singh, "Effect of Mn^{2+} and Cu^{2+} co-doping on structural and luminescent properties of ZnS nanoparticles", Ceramics International, 43 (9) (2017) 7193-7201. http://dx.doi.org/10.1016/j.ceramint.2017.03.007 **(3.450)**

6. **Neetu Bansal**, Gurbinder Kaur, K. Singh, "Braunite phase embedded Y_2O_3 /MnO_2-Al_2O_3-CaO-SiO_2 glass ceramics and their properties", Materials Research Bulletin 98 (2018) 34-40. http://dx.doi.org/10.1016/j.materresbull.2017.09.065 **(3.355)**

7. Satwinder Singh Danewalia, Supreet Kaur, **Neetu Bansal**, Savidh Khan, K. Singh, "Influence of TiO_2 and thermal processing on morphological, structural and magnetic properties of Fe_2O_3/MnO_2 modified glass-ceramics", Journal of Non-Crystalline Solids 513 (2019) 64-69. https://doi.org/10.1016/j.jnoncrysol.2019.03.013 **(2.600)**

8. Satwinder Singh Danewalia, Savidh Khan, Sandeep Kaur, **Neetu Bansal**, Gaurav Sharma, K. Singh, "Effect of transition metals (MO-TiO_2, MnO_2, Fe_2O_3 and ZnO) on crystallization and electrical conductivity of SiO_2-CaO-Na_2O-P_2O_5-based glass-ceramics", Ionics 26 (2019) 2959-2967.https://doi.org/10.1007/s11581-019-03311-y **(2.289)**

9. **Neetu Bansal,** Anandita Arora, Satwinder Singh Danewalia, K. Singh, "Synthesis, characterization and bioactivity of fluoride containing borosilicate glass matrix composite", Silicon (2020) https://doi.org/10.1007/s12633-020-00562-7 **(1.210)**

Papers presented in Conferences

1. Structural and thermal properties of alkali oxide containing calcium silicate glasses for photovoltaic application, at **International Symposium on Functional Materials-2018** held on 13-15 April 2018, at Shivalik View, Chandigarh.
2. Composition tuned glasses as substrate for inorganic thin film solar cells, at **International Conference on Materials for Energy Applications** held on 6-8 Dec 2018, at SS Jain Subodh PG College, Jaipur.
3. Assessing conduction and diffusion behaviour of alkali ions in calcium silicate glasses, at **International Conference on Electron Microscopy & Allied Analytical Techniques** held on 7-9 Jun 2019, at Himachal Pradesh University, Shimla.

Index

List of Figures

List of Tables

List of Abbreviations

BCC	Base centred cubic
BO	Bridging oxygen
CIGS	$CuInGaSe_2$
CIGSe	$CuInGaSe_2$
CIS	$CuInSe_2$
CZTS	Cu_2ZnSnS_4
CZTSSe	$Cu_2ZnSn(SSe)_4$
DC	Direct current
DTA	Differential thermal analyser
EDS	Energy dispersive x-ray spectroscopy
FE-SEM	Field emission-ccanning electron microscopy
FS	Field strength
FTIR	Fourier transform infrared
FWHM	Full width at half maxima
GRP	Glass fibre reinforced Plastic
GS	Glass substrate
HP	High pressure
HPD	High pressure deposited
ICDD	International centre for diffraction data
IPA	Isopropyl alcohol
KCS	Potassium calcium silicate
LCS	Lithium calcium silicate
LED	Light emitting diode

LP	Low pressure
LPD	Low pressure deposited
MAE	Mixed alkali effect
MDS	Molecular dynamic simulation
MGFE	Mixed glass former effect
NBO	Non-bridging oxygen
NCS	Sodium calcium silicate
NK	Na-K
NL	Na-Li
PDT	Post deposition treatment
SCCM	Standard cubic centimetre per minute
SEM	Scanning electron microscopy
SIMS	Secondary-ion mass spectroscopy
SLG	Soda lime glass
SOFC	Solid oxide fuel cell
TDA	Thermal dilatometric analysis
TEC	Coefficient of thermal expansion
TFSC	Thin film solar cell
TG	Thermo gravimetric
TV	Tele vision
UV	Ultra-violet
XPS	X-ray photoelectron spectroscopy
XRD	X-ray diffraction
ZSW	Centre for solar energy and hydrogen research Baden-Wurttemberg

Abstract

Extensive research is going on in the field of thin film solar cells (TFSCs) to improve its efficiency and reduce the cost. Various groups observed that the film grown on soda lime glass (SLG) substrate had a <112> oriented texture with absence of aggregate structures and aggregate boundaries due to (i)compressive stress between the film and substrate because of a better matched coefficient of thermal expansion (CTE), and (ii) contamination of absorber layer with sodium (Na) diffused from SLG substrate. Various theoretical, chemical and simulation models are proposed to explain that Na acts as a catalyst in the absorber layer to passivate the Se vacancies and reduce the defect trap states, which directly influence and improve the efficiency and performance of the TFSC. The extent of this effect is further explored by depositing a NaF layer of various thicknesses on different substrates and concluded that performance is best at 0.14 at% Na diffusion through SLG. Influence of Li and K pre and post-deposition is found to enhance the performance of cells.

Therefore, a glass substrate of a TFSC must have:

(i) Glass transition temperature (T_g)> 550°C

(ii) presence of Na, K, Li

(iii) CTE ~ 5-8×10^{-6} K^{-1}

(iv) Low cost

The present thesis describes the preparation of the alkali oxide containing calcium silicate glasses, wherein sodium oxide is systematically replaced by lithium and potassium oxide, via melt quench technique. The structural, optical, mechanical, thermal and electrical properties of the as-prepared glasses are studied using to determine their suitability as substrate for thin-film

solar cells. The synthesized glasses were prepared as substrate to deposit Molybdenum thin film to study the diffusion of alkali ions from glass to Mo-film. The thesis is divided into six chapters with a list of cited references at the end of each chapter.

Chapter 1 presents an introduction to glasses, its characteristic features, components of glasses and their effect on glass structure and their properties. Various engineering applications of glasses are discussed in detail, concluded with the need and importance of glass in thin film photovoltaics. The evolution of thin film photovoltaics to fulfil the highly escalating energy needs of the whole world is elaborated. Various components of thin film solar cells are discussed highlighting the importance of substrate materials and Mo as back contact electrode. Finally, the suitability of glass as substrate material is described in terms of specific properties such as mechanical strength, thermal stability, coefficient of thermal expansion, electrical properties and cost effectiveness.

Chapter 2 presents the detailed literature survey related to the type of substrate materials employed for the thin film solar cells so far. Role of alkali ion incorporation in CIGS/CZTS based thin film solar cells is reviewed in view of its effect on the efficiency of thin film solar cells. Conventionally used substrate materials for thin films are reviewed to conclude that alkali oxide containing glass is the most promising and cost-effective mode. A brief review of alkali oxide containing glass compositions is presented to study their effect on the desired properties for substrate materials. On the basis of the complete literature review, objectives of the thesis are determined and presented at the end of this chapter.

Chapter 3 elaborates the information of glass compositions and the raw materials taken to synthesize them. The procedure followed for the synthesis of glasses using melt quench technique is given in detail. The preparation of substrate for thin film deposition, from

synthesized glasses is also discussed in detail. The characterization techniques employed for studying the properties of glass samples are discussed in detail such as X-ray diffraction (XRD), Fourier transform infrared-spectroscopy (FTIR), X-ray photoelectron spectroscopy (XPS), differential thermal analyser (DTA), Impedance Analyser, UV-vis spectroscopy, Vickers hardness testing technique. Details of Sputtering machine used to deposit the Mo-film, field-emission scanning electron microscopy (FE-SEM) used to determine the thickness and morphology of the Molybdenum thin film are discussed. Secondary ion mass spectroscopy (SIMS) used to study the alkali diffusion from glass to thin film is also elaborated in this chapter.

Chapter 4 deals with the results and discussion part of the present work. The chapter is divided into two parts. Part I focuses on the effect of variation in type of alkali oxide contained in glass composition on the structural, mechanical, optical, thermal and electrical properties of glasses which is investigated in detail using various characterization techniques. Self-diffusivity of alkali ions within glass is estimated using impedance spectroscopy technique. The size of the alkali ion does not directly affect the structural, optical and electrical properties of the glasses. The diffusivity of sodium ions in sodium oxide containing glass is the highest.

Part II consists of the detailed investigation of effect of presence of another alkali oxide with sodium oxide in glass composition on various properties of the glasses in light of mixed alkali effect. Systematically substituting the sodium oxide by smaller sized lithium oxide and bigger sized potassium oxide into the present composition of glasses exhibits typical non-linearity in properties with respect to variation in composition. Its prospective effect on transport properties of alkali ions in glasses is given. The mixed alkali effect within glass enhances the conductivity with the substitution of lithium oxide, however, deteriorates on the introduction of potassium oxide in the glass composition.

Chapter 5 reports the growth and optimization of Molybdenum (Mo) thin film using DC magnetron sputtering under the influence of different sputtering parameters. The bilayer Mo-film with appropriate thickness, structure, morphology, adhesion and resistivity is optimized as the deposition power of 75W for 40 min high pressure deposition followed by 20 min low pressure deposition.

Chapter 6 elaborates the diffusion of different alkali ions from glass substrate to Mo film using SIMS. It shows that, as the self diffusion of Na in sodium oxide containing glass is highest, the extent of out-diffusion of Na ions from glass to Mo film is the highest. The out-diffusion of Li and K ions is low. Further, it presents the comparative study of sodium ion diffusion from commercially available soda lime glass and synthesized sodium calcium silicate (NCS) glass, respectively to the Mo-film deposited onto it and found that the extent of diffusion in NCS glass is higher than commercially available SLG.. The lattice and grain boundary diffusion coefficients for alkali ions are estimated by fitting the diffusion profile using error function and Whipple's Analysis. Profile in the interfacial region is fitted to estimate the interfacial access of alkali ions. The diffusion mechanism of alkali ions follow Harrison's type B diffusion kinetics. The composition of substrate material is found to critically influence the out-diffusion of alkali ions to the overlayers.

Chapter 7 elucidates the conclusion of the entire work done in the present thesis and future scope of the current study. The major conclusion of this work is that, based on all types of preliminary investigations, the synthesized glasses fulfil the requirement of properties to be suitably used as substrate for thin film solar cells, with suitable mechanical strength, glass transition temperature higher than 540°C, coefficient of thermal expansion close to SLG, and matches well with that of the Mo/CZTS thin films. The Mo-film optimized using sputtering

conditions is appropriate for use as back contact electrode of the CZTS/CIGS based thin film solar cell with thickness of 1 micron, (110) oriented BCC structure, leafy morphology, good adhesion and resistivity of the order of 10^{-4} Ωcm. Single alkali ion in glass composition shows better diffusivity in case of Na and Li ions as compared to mixed alkali glasses. Comparative study of Na diffusion from SLG and NCS glass shows that the extent of diffusion in NCS glass is higher than SLG. Thus, our synthesized NCS glass is a suitable and promising candidate for the application as substrate for thin film solar cell.

Future scope of the study includes the comparative study of grain boundary characteristics of the CZTS film deposited onto SLG and synthesized glasses, and to study the effect of composition on the performance of solar cell deposited onto the synthesized substrates.

Chapter 1 Introduction

1.1. Introduction of glasses

Glass is an important material in modern life, found in every nook and corner, such as in windows, decorative pieces, lights and bulbs, mirrors, spectacles, a screen of the cell phone, etc. Besides all these, it forms an integral part of almost all the optoelectronic devices. Glass has evolved as a necessity for the civilized society owing to its versatile physical, optical, mechanical, thermal, and dielectric properties, which render it suitable for various applications. However, the properties are a function of materials characteristic components, their volume, and thermal history.[1–4]

Glass and amorphous solids are subclasses of non-crystalline solids. However, glass exhibits glass transition temperature (T_g) with a very short-range order (~3-10 Å) of structural units spanning to a broad range of angles between cation polyhedral.[5,6] It can be better understood from the enthalpy temperature diagram [**Fig. 1.1**] shown below:[5]

The inorganic glass components are melted at a high-temperature melting point ($T>T_m$). When the melt is cooled, the structural rearrangement of atoms leads to an abrupt fall in enthalpy to form long-range ordered crystals as shown in **Fig. 1.2 (a)**. However, induced cooling of the liquid at a faster rate without a sudden drop in enthalpy leads to the formation of a super-cooled liquid, in which the structural rearrangement is discontinued. This results in a randomized structural arrangement of amorphous material as shown in **Fig. 1.2 (b)**.

The viscosity of the supercooled liquids increases sharply up to 10^{12} Pa.s at the glass transition temperature. Thus, glasses are known to exhibit viscoelastic behavior on heating and solidify on cooling at the glass transition temperature.[2]

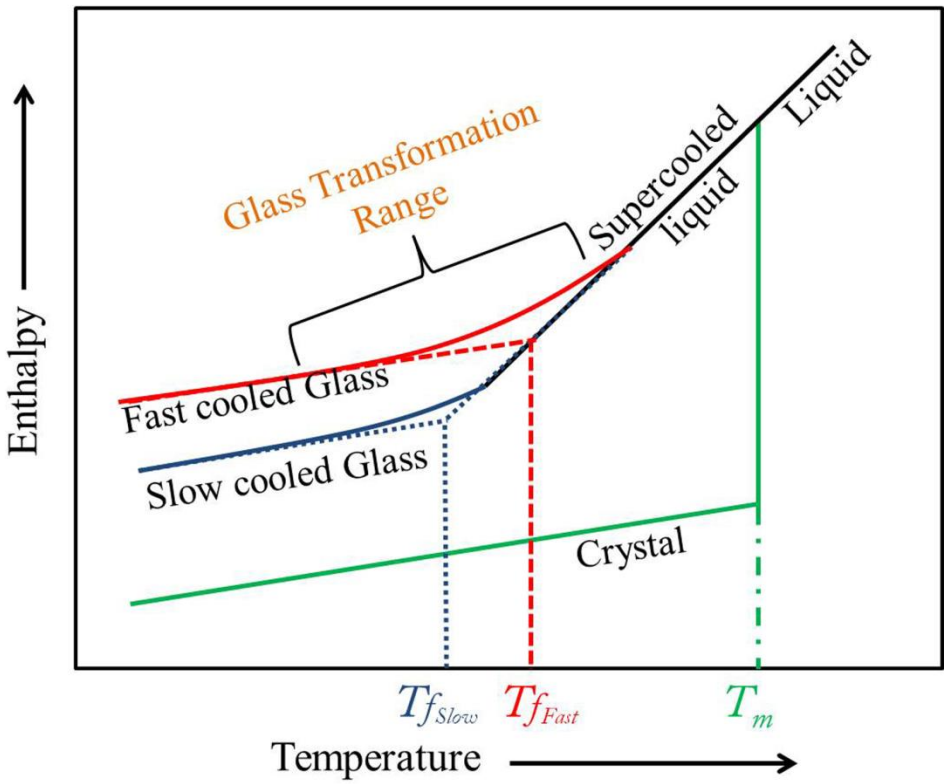

Figure 1.1: *Enthalpy-temperature diagram of crystal and glass with respect to different cooling rates.*[5]

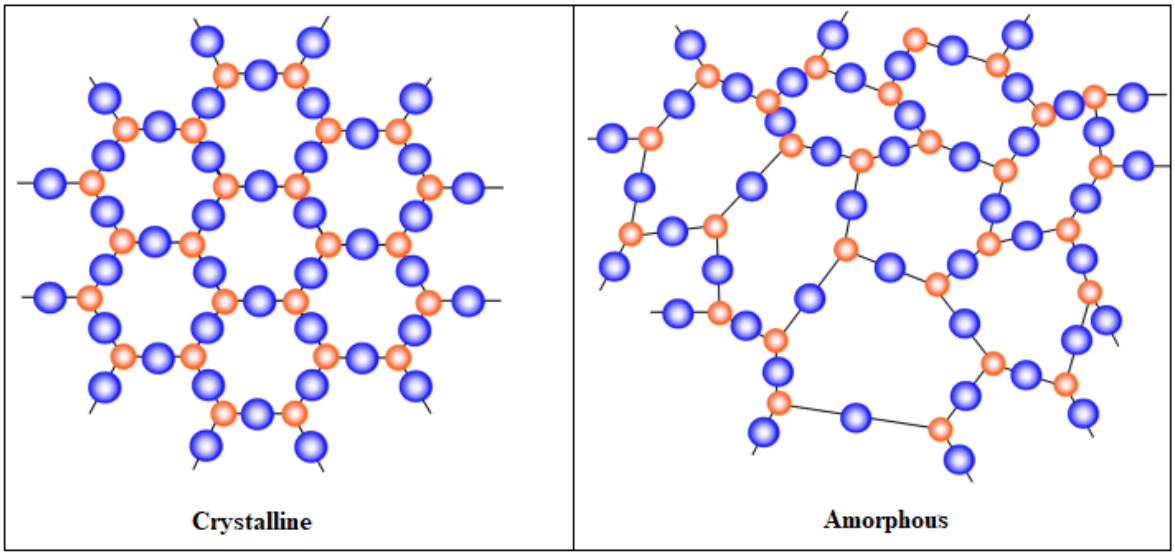

Figure 1.2: *(a) Crystalline and (b) amorphous structure of polyhedral units formed due to the cooling of melt at different rates.*

1.2. Components of glasses

Inorganic glasses are composed of oxides of various elements such as silicon, germanium, vanadium, phosphorus, boron, etc. The components of a typical glass are classified into four types [**Fig. 1.3**] based on the role played by them in the formation of the glass structure.

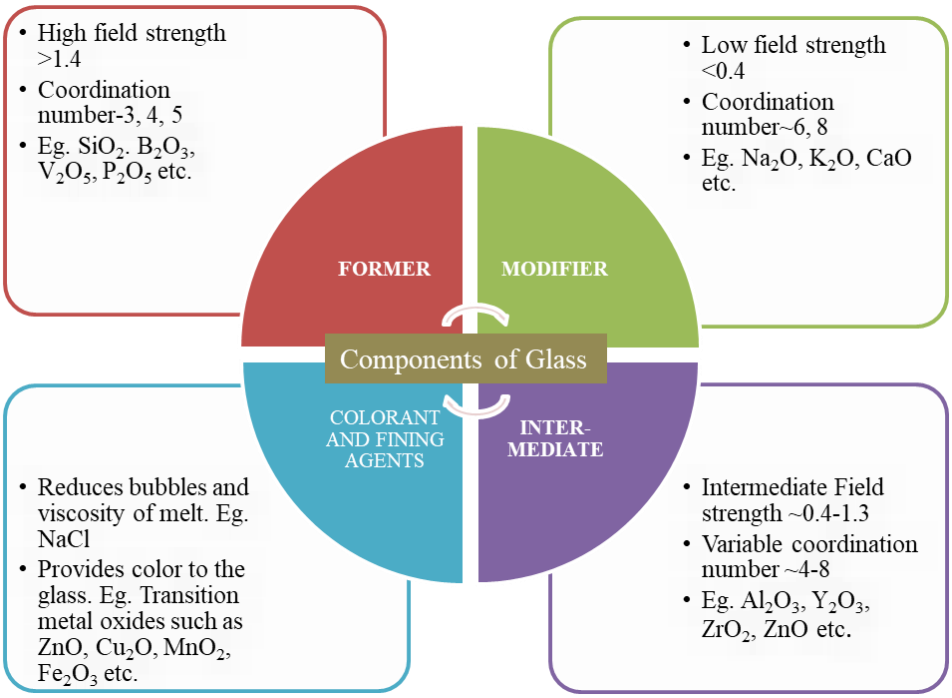

Figure 1.3: *Typical main components of glasses, their role, and properties.*

The properties of glasses are tailored by varying the composition and amount of various component oxides. The glass network former, with high field strength and bond dissociation energy (~80-180 kcal/mol), form triangular or tetrahedral units within the glass network.[7] The former cation is coordinated with oxygen anion where oxygen acts as a bridge between the two network cations such as Si-O-Si, B-O-B, P-O-P, etc. These oxygen ions are termed as bridging oxygens (BOs) in the nomenclature of glass science. Inorganic oxide glasses are commonly known by the name of their network former components such as silicate glasses, borate glasses, borosilicate glasses, etc.[5] Another component of the glass is a modifier, which modifies the structure of the glass network by breaking the cation-oxygen bond of former cations to create

non-bridging oxygens (NBOs). Depending upon the concentration and valence state of the modifier cation, the amount of NBOs varies, which modifies the properties of the glasses. The higher mobility of modifier cation influenced by their low field strength (as mentioned in **Fig. 1.3**) and increased number of NBOs significantly affect the transport properties of the glasses, such as energy bandgap, conductivity, and diffusivity. Examples of some of the commonly used modifier oxides are Li_2O, Na_2O, K_2O, CaO, MgO, SrO.[8] Intermediates are the other important components of glass, which are the oxides having a field strength between 0.4-1.3. These can act either as a glass former or as a modifier in glass structure depending upon their percentage in the glass composition. For example, Al_2O_3 up to 5 mol% composition acts as a former whereas at higher concentrations helps in modifying the local glass structure.[9] However, its role depends on the initial constituent of glasses. The most commonly utilized intermediates are Al_2O_3, Y_2O_3, ZrO_2, etc. These have a coordination number lying from 4 to 8. Intermediates help in selective tailoring of glass properties. For instance, Y_2O_3 containing glasses are known to have high mechanical strength, fracture toughness, and enhances the thermal stability of the glasses also.[10,11] Furthermore, the fining agents and colorants are used as additives to the glass composition in a small concentration of 1-3 wt%. Fining agents such as NaCl, KCl, As_2O_3, Sb_2O_3 is added to the composition to minimize the bubbles in the glass and reduce the viscosity of the melt. Colorants, as the name suggests, provide color to the otherwise transparent glasses. Oxides of transition (3-d) and rare earth (4-f) elements act as colorants in glasses, for example, iron, manganese, copper, gold, silver and many others.

1.3. Properties of glasses

Glasses do not possess long-range order and granular structure. Because of this, the properties of glasses are different than their crystalline counterparts. Moreover, the presence of

multiple components in glasses with different individual properties imparts a blend of properties. In the following, the various properties of glasses are presented.

(i) Optical properties: Glasses find numerous applications based on their optical properties such as transparency, reflectivity, absorptivity, and refractive index. These properties are strongly influenced by the glass composition. The higher the NBOs, the higher is the refractive index of the glass.[12] The cooling rate of the glass during formation also affects the optical transparency of the glass materials. Glass cooled at a faster cooling rate possess higher transmittance. Transmittance and reflectance of solar radiation at a specific wavelength describe the feasibility of the use of the glass for various optical applications. For instance, the refractive index of commercially available soda-lime glass (SLG) ~ 1.5 with a transparency of ~90%.[13]

(ii) Mechanical properties: The mechanical strength, hardness, fracture toughness, and elastic modulus of the glasses are significant parameters for any application. For example, glasses used in windows and aircraft should possess high fracture toughness. The hardness and elastic modulus of the glass is dependent on the structure and bonding of ions in the vitreous network. Stronger the bonds in the glass network, the higher the hardness. However, fracture toughness is dependent on the environmental, physical, and thermal treatment of the glass materials, along with strong dependence on the glass composition. Thermal shocks lead to glass cracking and failure.[14] Surface treatment with chemicals/acids also reduces fracture toughness of glasses. Glasses are hard and brittle materials with hardness~4-8GPa, which is higher than metals and lower than ceramics.[15–17] Na_2O modified glasses usually possess hardness~5GPa, while Y_2O_3 contained glasses exhibit hardness~7-8GPa.[10,18,19]

(iii) Thermal properties: Since glasses are widely applicable components in various devices such as lasers, solid oxide fuel cells (SOFCs), thin film solar cells (TFSCs), etc., the thermal

stability of glass becomes an important parameter at high processing and operating temperature of devices.[20,21] In high-temperature SOFCs working at 800-1000°C, glasses are used as sealants.[9,22,23] The prolonged operation at high temperatures may result in a device failure due to possible phase transitions and coefficient of thermal expansion (TEC) mismatch. Similarly, the glass substrate used in film solar cells is desired to have a TEC matched with the absorber layer of the TFSC and should possess a glass transition temperature higher than the thin film processing temperature.[24,25]

(iv) Electrical properties: Glasses are generally categorized as insulators/dielectrics due to the presence of non-conducting or insulating nature of glass network formers like silicates, borates, and phosphates. However, the introduction of modifier oxides induces ionic conductivity in the glass network due to the mobility of the alkali or oxide ions. Alongside, the water molecules adsorbed on the glass surface lead to dissociation of protons from Si-OH bonds leading to protonic conduction.[26] The ionic hopping from one site to another is responsible for this ionic conductivity. In general, the higher the NBOs in glass, the higher is the ionic conductivity.[27,28] On the other hand, the presence of intermediate oxides, which tend to exist in multiple oxidation states, induces electronic conductivity in glasses.[29,30] These properties render glasses suitable for electronic devices such as solid-state batteries.

1.4. Application of glasses

As discussed above, various glass properties are a function of the structure and composition of glass, which further verifies its suitability for particular applications. Different applications have specifically desired properties. To throw light on this aspect, various fields of application of glasses are given below.

(a) Optics: The vast field of optics is entirely based on glass materials, along with other transparent optical ceramics. The transparent nature of glasses along with diverse optical properties makes them an essential component in various optical applications like optical fibers, light-emitting diodes (LEDs), lamps, lenses for optical corrections, light concentrators, and so on.[31–33] Glasses with varying compositions exhibit tailored refractive index, bandgap, and dispersion properties which make them an important component of optical instruments.[32,34] Glasses have also been used in displays from the cathode ray tube-based televisions (TV) to liquid crystal displays and LED TVs.

(b) Industry: Glasses find applications in many industries. Nuclear waste glasses have emerged as a chemically durable method to immobilize radioactive waste.[1,35,36] The glass textile industry produces glass fibers to create reinforced material composites with high strength and durability like glass fiber reinforced plastics (GRP), glass fiber reinforced concrete, polymers, and sheets.[1,14] Laboratory equipment and glassware are made from borosilicate glasses due to their high resistance towards corrosion, chemical attack, or thermal shock. Glass cookware and utensils make the kitchen most dazzling. The food cooked or heated in glassware is considered safest due to the chemical and thermal inertness of the glass materials. Furthermore, glasses and their wastes are also being used in the construction industry.[4]

(c) Biomaterials: Ever since the discovery of bone-bonding in 'Bioglass®' and 'bio-active glass' by Hench *et al.*, glasses and glass-ceramics are widely tested and researched for biological problems. [37,38] Bioglasses and glass-ceramics are found to be useful in replacing soft tissues in the ear, nose, and throat to cure damaged parts, in dentistry for tooth implants, maxillofacial repair, bone-grafting in orthopedics, hyperthermia treatment of cancer, and so on.[3] Bioglass 'Ceravital®' has appeared as a suitable alternative to metal implants in replacing the soft tissues

in ears, to cure conductive loss in hearing. [39] Suitable tested and certified bioglasses have been developed for denture construction like Biosilicate® and Biogran®. The coating of different glasses on various orthopedic implants not only increases their mechanical properties but also reduces the degradation and leaching of implants.[40]

(d) Electronics: Glass is used in one form or the other in electronic and microelectronic devices due to its versatile nature and eases to tailor the properties according to need and application. While glass is used in displays for most of the devices, it is used as a substrate and dielectric material in integrated circuits.[41,42] It is used as a sealant in solid oxide fuel cells (SOFCs) to seal different layers of SOFC together, due to its high thermal stability and TEC.[43,44] Glasses are used preferentially as the substrate in film solar cells due to its good mechanical strength, and thermal stability and as superstrate due to its high optical transmission and low cost. The SLG is the most commonly used substrates for thin film solar cells and has yielded the highest efficiency for the $CuInGaSe_2/Cu_2ZnSnS_4$ based thin film solar cells to date.[45] The importance of the glass in the photovoltaic industry and in particular in TFSCs is discussed in detail in the following section.

1.5. Glass as a critical component in thin film photovoltaics

In view of the increasing energy needs and the environmental threat arising from the consumption of fossil fuels for energy, there has been intense research on non-exhaustible and clean energy sources. In recent years, thin film photovoltaic has emerged as a key technology that promises to deliver affordable clean electricity from solar energy and hence, to mitigate the energy crisis to a significant extent. More recently, Cu_2ZnSnS_4 (CZTS) and it's Se alloyed counterpart $Cu_2ZnSn(SSe)_4$ (CZTSSe) have emerged as leading absorber candidates. In addition to the earth abundant, non-toxic, and inexpensive constituents, CZTS reveals an absorption

coefficient as high as 10^4 cm^{-1} and a tunable bandgap (ranging from 1 to 1.5 eV) that can favorably match with the solar spectrum.[46,47] Thus, CZTS appears to be both economically and ecologically viable without serious constraints from raw materials. In the last few years intensified research on CZTS has progressed its energy conversion efficiency from about 6.8% in 2008[48] to beyond 12% just in a few years.[49]

A typical CZTSSe based solar cell consists of a number of layers, each having a thickness in the range of 1-2 µm as shown in **Fig. 1.4**. The p-type absorber (CZTSSe) and the n-type buffer layer (CdS) are sandwiched between the bottom and top electrodes along with the window layer (ZnO). While Molybdenum (Mo) is the most potential candidate for the bottom electrode, the Aluminium (Al) grid acts as a top contact, which is both connected to the battery for charge storage. The key factors required to maximize the efficiency are the efficient carrier generation and their transport and collection at the electrodes. For instance, the upconversion mechanism induced by the rare earth doped glasses are observed to enhance the generation of electron-hole pairs in Si-based solar cells in the infrared region of solar radiation.[50]

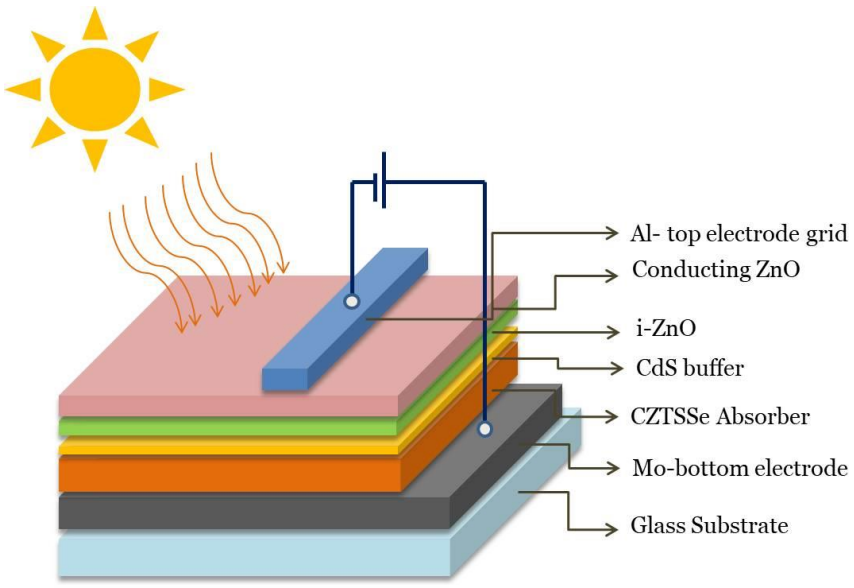

Figure 1.4: *Schematic diagram of thin film solar cell.*

Thin film solar cells being devices of multiple layers (as shown by a schematic in [**Fig. 1.4**], properties of individual layers, and integrity of the interfaces across them seriously affect the device performance.[51–53] Among all the components, the substrate plays a critical role in that it provides the mechanical support to the device and is expected to withstand the thermal treatments necessitated for the growth of the absorber and other layers. The substrates for the CZTS and $CuInGaSe_2$ (CIGS) based thin film solar cells must have (i) a high T_g so that it does not deform during the heat treatment (typically ~550 °C) required for the phase formation of CZTS or CIGS and (ii) an appropriate TEC matching with that of the overlayer to avoid the device failure due to volume change in both the components.[24] As mentioned earlier, SLG has been the most widely used substrate for the CIGS and CZTS thin film devices. Besides being thermally stable, SLG acts as a source of sodium (Na) that out-diffuses to the absorber layer via the bottom electrode (typically ~1 μm thick Mo film). The diffusion of Na from the SLG substrates to the absorber layer (i.e., CZTS or CIGS thin films) has been accepted as a key factor in enhancing solar cell efficiency[54–57] via suppressing the formation of undesirable donor-type Se vacancies,[58] passivating the grain boundaries due to creation of the acceptor-type NaIn defects (where Na occupies the In vacancies in CIGS thin film),[59] forming oxides (a Cu-deficient condition[60]) which can reduce surface recombination between CIGS and CdS layers,[61,62], etc. Expectedly, the devices with substrates without any alkali ions have performed poorly than those with substrates having alkali ions.[63–65] It may be noted that recently as an alternate method of supplying alkali ions, some groups have carried out post-deposition treatment of alkali metal compounds in CIGS solar cells.[45,57,58] Nevertheless, as evidenced from numerous reports, many of the CIGS and CZTS solar cells based on absorber layers grown on SLG and relying on the diffusion of Na from the substrate to the overlayers have yielded very

high efficiencies, for example 20.3% for CIGS and 12.6 % for CZTS (the highest efficiency, till date).[49,66] Furthermore, besides routinely yielding an acceptably good efficiency, the conventional route (i.e., diffusion of Na from substrates) offers a scalable approach as it simplifies the process steps considerably. However, the diffusion of Na from the substrates through back contact (bottom electrode) to the absorber layer is limited by the microstructure and packing density of the bottom electrode.[67,68]

1.5.1. Mo layer as the bottom electrode

The bottom electrode is expected to have excellent ohmic contact with the absorber layer and low resistivity for efficient charge transfer, while chemical inertness and strong adhesion to the substrate are highly desired for the structural integrity of the device. These properties, however, are strongly influenced by the parameters of the thin film deposition processes. Molybdenum (Mo) thin films have been widely used as a back electrode in CZTS and $CuInGaS_2$ (CIGS) based thin film solar cells.[69,70] Traditionally, sputter deposition has been the most popular choice for the growth of the Mo thin films in solar cell applications.[67,71] In the sputtering process, the deposition conditions such as chamber pressure, power, deposition time, substrate temperature, etc. are shown to affect the structure-property correlation of the Mo films.[72–74] For example, the increase in deposition power yields better crystallinity and lowered resistivity of the Mo films.[75] The deposition power regulates the sputter yield and the energy of the sputtered species, and hence, the rate of arrival of the depositing species on the substrate surface, which in turn determines the adhesion of the films, surface morphology, and electrical properties.[72,76] Separately, the pressure variation of the order of 0.1-1 $x10^{-3}$ Torr is reported to affect the kinetic energy of the sputtering ions, and hence the packing density of the film.[68,72] For the Mo thin films, deposition at high pressure yields films with excellent adhesion but with

relatively higher resistivity primarily because of micro-cracks in the films, whereas the low pressure deposition leads to lower resistivity but very poor adhesion.[67,71] Consequently, there have been attempts to grow bilayer- first using high pressure followed by that at low pressure, thus taking advantage of both pressure regimes.

Studies in SLG/Mo/CIGS depict a clear dependence of Na diffusion on the morphology and microstructure of the Mo films.[77] The Na doping level in the CIGS absorber is reportedly proportional to the concentration of Na ions that accumulated at the interface between the CIGS and the Mo layer, and the extent of Na accumulation depends strongly on the surface characteristics of Mo back contact layers.[57,78] Thus, it is very important to grow conducting Mo films with high control on the microstructure that can provide a better diffusion path for Na from the substrate to the absorber layer.

1.6. Requirement of a glass substrate in CZTS based thin film solar cells

The diffusion of alkali metal atoms from the SLG substrate reportedly affects the grain boundaries, grain size, defect states, texture, and orientation of the absorber layer, which enhances the efficiency of the solar cell by ~5%.[79] This highlights that the substrate not only provides mechanical support to the module but also qualitatively and quantitatively affects its performance. The typical requirements, summarized from the above discussion, for the substrates for potential integration in CZTS thin film based solar cells include the following points.

i. It should be thermally and mechanically stable in a high vacuum (reducing atmosphere) and high temperature during the processing of the cells.
ii. It should be cost-competitive.
iii. The TEC must be comparable to other components, more importantly with the absorber layer, of the solar cell.

iv. It should have a smooth surface so that it does not adversely affect the other components.

In the following, a few key parameters are described which should be considered while developing the substrates for solar cells, especially for the CIGS and CZTS based ones.[80]

(i) Glass transition temperature

Generally, the growth process of the high performance CZTS thin films involves a temperature of ~500°C for the fabrication of thin film solar cells. The glass transition temperature (T_g) is, therefore, required to be higher than the processing temperature of the thin films, or the processing duration must be short enough to ensure that softening or bending of the substrate does not take place or the substrate does not chemically react to the growing absorber materials. While preparing a glass by melt-quench technique, the variation in the glass composition of the melt can tailor the T_g.[5] On the other hand, fictive temperature T_f depends on the cooling rate, which corresponds to T_g when the cooling rate is around 10 K/min.

(ii) Chemical composition

The composition of the substrate material plays a major role in deciding the characteristic properties of the substrate as well as the quality of the absorber layer deposited on it. Literature reports have shown that the presence of alkali metal (Li, K, Na)[63,81,82] in the SLG has improved the performance and efficiency of the chalcopyrite based thin film solar cells. Sodium from the substrates is found to diffuse into the absorber layer and acts on to passivate the Se vacancies present.[83] On the other hand, the composition of the glass can affect the properties of the glass material, such as its transformation and softening temperature, hardness, density, etc. Silica and boric oxide in a glass act as a network former for the structure of glass, while alkali oxides play the role of flux to lower the processing temperature of the glass, but on the other hand, it adversely affect the mechanical and thermal properties of glass. To counter the degradation in

properties of the glass, property modifiers such as alkaline earth oxides or transition metal oxides are added in a small amount.[5] Thus a batch of composition is decided keeping in mind the desired properties of the glass material.

(iii) Coefficient of thermal expansion (TEC)

The thermal expansion of the substrate must be adapted to the absorber layer material, in order to avoid ablation or cracking of the subsequently deposited films on it. TEC of CZTS (kesterite) ~ 6.14×10^{-6}/K and for CZTS (stannite) ~ $4.14\times10^{-6}K^{-1}$,[84] ~ 9.6×10^{-6} K^{-1}.[85,86] The TEC of the Mo layer that acts as the bottom electrode is 5.1×10^{-6} K^{-1}. The Mo layer is deposited directly on the substrates, on which the growth of the CZTS/CIGS proceeds. The TEC of the usually available SLG substrate is > 10×10^{-6} K^{-1}. However, it can be tailored by modifying the composition of the glass material. Strong network formers, generally, have a negative TEC due to a strong structure which can absorb thermal expansion by bending of bonds. The addition of alkali oxides increases the TEC due to the modification in structural units which makes the system more rigid. However, introducing an appropriate amount of alkaline earth oxides decreases the TEC due to the replacement of low field strength alkali ions by high field strength divalent alkaline earth metal ions. Thus an appropriate TEC can be achieved by optimizing the composition of the glass substrate.

(iv) Cost

The cost of the substrate must not exceed the contribution of 50% to the total module cost. The cost parameter also restricts the material and techniques used to prepare the glass so as to minimize the cost of the obtained product, including the post-processing treatment such as cutting, grinding, polishing, and cleaning to prepare it to be used as a substrate.

Table 1.1: *Desired properties, their details, and design challenges for glass as the substrate in solar cell application.*[1]

Properties	**Details**	**Challenges**
Mechanical Properties	• Enhanced strength with a minimum density • Improve fracture toughness	• Stronger glasses and glass–ceramics • Mechanical treatments to improve strength and resistance at environmental events (sand storms, etc.)
Thermal Properties	• Thermal expansion characteristics of the system • Thermal stability during film growth process	• Heat treatment and controlling cooling kinetics.
Chemical Properties	• Maximized resistance to environmental conditions	• Improved resistance at corrosion to acid rains or environmental salinity
Manufacturing Properties	• Viscosity that complements specific manufacturing process	• New manufacturing techniques for customized designs and compositions

Overall, the strength, coefficient of thermal expansion, chemical durability, manufacturability, etc. are important parameters to be considered while evaluating the suitability of material as a substrate for CIGS or CZTS based solar cells.[2] The engineering conditions for glasses as a substrate in solar cells are given in **Table 1.1**.[1]

These basic properties, along with the ability to alter the characteristics by varying the composition of the glass, make it most suitable to be used as a substrate for solar cells. Considering that the composition of the glass **(Section 1.1)** strongly influences the eventual properties of the glasses, designing composition-tuned glasses becomes a key issue. In the following chapter, a brief review of the literature relevant to the designing of a glass substrate for thin film solar cells is presented.

Chapter 2 Literature review

In this chapter, detailed literature relevant to this study is presented. In the context of thin film solar cells, the type of substrate materials and the importance of incorporation of alkali atoms in thin film solar cells are reviewed. The different methods employed for the alkali ion incorporation into thin films are compiled to conclude that diffusion from the alkali oxide-containing glass is the most promising and cost-effective mode. A brief review of alkali oxide containing glass compositions is presented to study their effect on the desired properties for substrate materials. Finally, the mechanisms of alkali-diffusion in glasses are reviewed to find the gaps in the study. On the basis of the literature review, the objectives of the thesis are determined and presented at the end of this chapter.

2.1. Role of alkali ion in CIGS or CZTS based thin film solar cells

While most of the efforts in realizing high efficiency CIGS or CZTS based thin film solar cells are focussed on the optimization of these absorber layers, for example, on obtaining phase pure films with a compact large-grained microstructure,[87,88] more recently several other factors including the presence of alkali ions are identified to have a critical influence on the performance of the cells.[24,89–92] For instance, Na beneficially alters the grain boundary properties, thereby allowing the development of efficient cells from polycrystalline CIGS.[93] The incorporation of Na has been achieved through its out-diffusion from the Na-containing substrate or diffusion from a Na-precursor layer (for example, by depositing NaF prior to the deposition of the absorber layer) or via post-deposition treatments of alkali ions during sulfurization or selenization.

The impact of the presence of Na ions on the absorber layer has been examined by several research groups. For example, Hedstrom *et al.* performed a set of experiments to

investigate the performance of ZnO/CdS/CIS thin film solar cells grown on different substrates such as soda-lime float glass, borosilicate glass, sintered-alumina, and sapphire.[83] They found that among all substrates, the soda-lime float glass resulted in a pronounced orientation of <112> textured CIS ($CuInSe_2$) films, which in turn is expected to improve the efficiency of the solar cells. Contamination of CIS layer with approximately 10% Na, presumably from out-diffusion from the SLG substrate, critically influenced the formation of polycrystalline film structure. The presence of Na in CIGS thin films was also revealed from the XPS (X-ray photoelectron spectroscopy) studies by Ruckh *et al.* along with the formation of Se-O, In-O, and Ga-O bonds.[63] These studies indicated that the improved characteristics of the CIS/CIGS films (deposited on SLG substrates) are influenced by the diffusion of Na from the SLG substrate to the overlayers.

The catalytic effect of Na on the surface oxidation of semiconductors during the growth of CIGS thin films is understood from the chemical model by Kronik *et al*.[94] and Cahen *et al*.[95] Kronik *et al.* proposed that the presence of Na acts as a catalyst for the physisorbed oxygen on the CIGS surface and grain boundaries to increase its polarisation, resulting in O^{2-} ions, which then passivate the selenium (donor) vacancy by making an In-O bond. Mungan *et al.* modeled the influence of Na on the CIGS solar cells to test the major parameters, viz the passivation of defects leading to an increase in carrier density; modification in a concentration gradient of Ga, and effect on the orientation of grains of the absorber.[54] Their simulation results led to the conclusion that the effect on passivation of defect states to enhance the carrier density is the most prominent one among the others. Wei *et al.* presented a theoretical study on the effects of Na on CIS by calculating the ground state properties of $NaInSe_2$, $CuInSe_2$, and co-related binary components using the first principle.[96] According to this model, Na eliminates the defects

present in CIS to raise the hole density and lowers the Fermi-energy by removing the carrier traps. However, excess of Na removes Cu vacancies and reduces hole density, which has a negative effect on the solar cell performance.

The 'Na concentration effect' was further investigated by employing alternate methods of alkali-incorporation to the absorber layer, such as pre deposition of NaF precursor layer of different thickness prior to the absorber layer, or post deposition treatment of Na ions during sulfurization. For instance, Igalson *et al.* studied the electrical properties of CIGS devices with NaF layer of varying thickness deposited on the SLG substrate with alumina barrier and compared it with those of baseline SLG substrate.[64] They found that when the amount of Na available for diffusion is not sufficient enough during the growth of the absorber layer, an exceptionally enhanced p^+ layer develops, which caused deterioration of the performance of the solar cell in the form of losses in open-circuit voltage and fill factor. It is concluded that the presence of Na improves its morphology along with a reduction in the undesired p^+ layer at the hetero-interface. While reviewing the effect of Na on the single crystal and polycrystalline CIGS films, Rockett concluded that Na affects the organization of point defects on the surface of the CIGS thin films during its growth.[97] This acts as a surfactant, improves the surface, and hence the bulk quality of the thin films. The device performance is found to be majorly affected by the point defects which act as carrier collection centers. It is proposed that Na enhances the concentration of holes by modifying the concentration of defects and preventing them to organize as clusters. Na(1+) occupies In(3+) vacancies to create Na_{In} defects which enhances the hole concentration. Ishizuka *et al.* have fabricated CIGS solar cells on glass substrates with varied thickness of sputter-deposited SLG thin films before the Mo contact layer in order to study the effect of various concentrations of Na during the growth process of the CIGS thin

film.[56] An increase in the Na concentration was found to decrease the grain size of CIGS film with <112> oriented texture. Along with this, the concentration gradient of Ga was found to be more with the increase in Na, which resulted in a decrease in the bandgap of the absorber. Also, the *p*-type conductivity of the layer was found to be enhanced with compensation of point defects in the presence of Na along with O, which is attributed to the formation of an acceptor level. Erslev *et al.* studied the metastable kinetics of CIGS solar cells based on SLG substrate and compared them with that of devices grown on SLG substrates with a SiO_2 diffusion barrier.[98] They reported two main effects, namely, defect state passivation by Na close to CIGS/CdS interface and change in metastable kinetics observed on exposing the solar cell to white light. It is found that the presence of Na increases the density of acceptor centers as well as the free carriers, whereas the change in free carrier density is not that prominent in the case of solar cells without Na. Moreover, the Urbach energy calculation shows that the presence of Na reduces the structural disorder, created by the presence of the Cu_{In} antisites. The increase in the hole concentration in the absorber layer with the increase in Na concentration is also shown by Li *et al*.[99] Na renders the acceptor level deeper in the energy band diagram. Consequently, there was an increase in V_{oc}. Bodeg Ard *et al.* performed a series of experiments to compare the efficiency of solar cell devices grown using NaF precursor layer with varying thickness on SLG substrate with and without a Na diffusion barrier of silica or alumina.[100] Their studies revealed that the effect of Na on the electrical properties of solar cell saturates at a point, as NaF layer of thickness > 200 Å on alumina barrier substrate (efficiency~15.4%) and on SLG substrate (efficiency~14.7%). The amount of Na in CIGS is estimated to be ~ 0.14 at%, with or without NaF on SLG substrate. From these studies, we conclude that, the incorporation of Na ions in

absorber layer improves the quality of the absorber layer and enhances the device performance irrespective of the method of incorporation.

Along with the Na-ions, the incorporation of Li, K, and other heavy alkali ions (Rb, Cs) have also yielded significant results. Bodeg Ard compared the efficiency of solar cells with LiF precursor layer in place of NaF and observed that the efficiency is no better than the baseline SLG substrate solar cell.[100] Probst *et al.* had designed a method to make the chalcopyrite absorber layer solar cell to be independent of the alkali metal ions diffusing from the substrate by depositing a diffusion barrier layer (TiN, Al_2O_3, SiO_2, Si_3N_4, ZrO_2 or TiO_2) on the SLG substrate and doped the absorber layer with alkali ions (Li, Na, K) via a post deposition treatment in order to fuse alkali atoms in a controlled amount (~ 10^{14}-10^{17} alkali metal atoms per square centimeter of the absorber layer).[101] They achieved a solar cell efficiency of 10%. Chirila *et al.* obtained a 20.4% efficient solar cell by post deposition treatment of K of the CIGS absorber layer already having Na.[82] It is observed that K replaces Na from the absorber film via the ion exchange mechanism and supports the diffusion of Cd in the Cu-depleted absorber surface layer, which leads to the enhancement in the quality of the heterojunction formed between CIGS/CdS. ZSW group has recently reported the record efficiency of 21.7%[45] and 22.6% [102] for CIGSe based thin film solar cells influenced by the post-deposition treatment (PDT) of heavy alkali ions (K, Cs, Rb) during the CIGSe growth process grown on SLG substrate.

"The literature review presented above clearly indicate that the CIGS and CZTS solar cells based on absorber layers grown on SLG and relying on the diffusion of Na from the substrate to the overlayers have yielded enhanced efficiencies, for example, 20.3% for CIGS and 12.6% for CZTS (the highest efficiency, till date).[49,66] Furthermore, besides routinely yielding an acceptably good efficiency, this conventional route (i.e., diffusion of Na from substrates)

offers a facile approach as it simplifies the process steps considerably. It may be mentioned here that the incorporation of other alkali ions viz Na, K, Rb has also resulted in better solar cell efficiencies.

In the next section, the typical substrates used in the thin film solar cells have been reviewed to establish the relevance of this study (i.e., to design a substrate).

2.2. Substrate materials

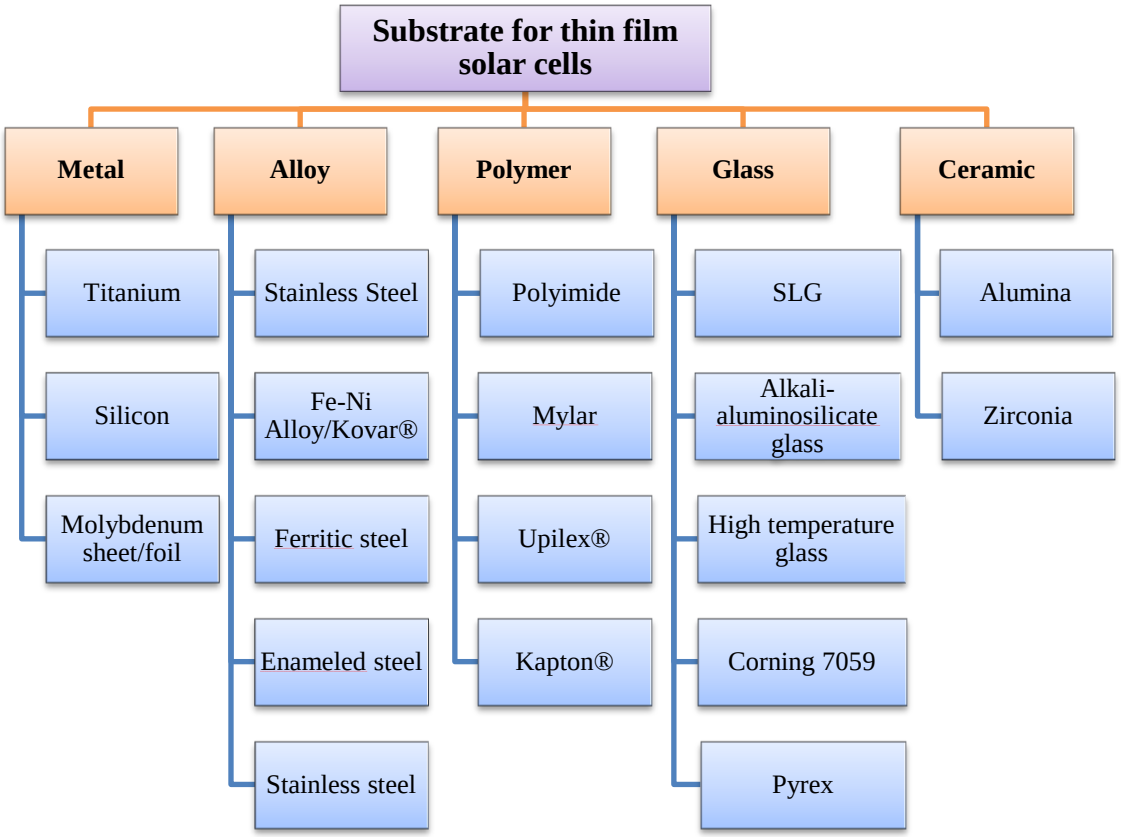

Figure 2.1: *Classification of commonly used substrate materials in thin film solar cells.*

The substrate is an integral part of thin film solar cells. A film stands on the substrate for its mechanical strength and support to the device. The basic requirements of substrate material, as discussed in **section 1.4**, limit the use of any material to be suitable as a substrate. In literature,

one can find a variety of substrates used in CZTS (or CIGS) based thin film solar cells, as shown in **Fig. 2.1.** The commonly employed substrate materials and their properties are tabulated in **Table 2.1**.

Table 2.1: *Commonly used substrates their properties for thin film solar cells along with their record efficiencies for CIGS based thin film solar cells.*[52,65,103–106]

Substrate Material	Density (g/cc)	TEC (ppm/°C)	Challenges	Efficiency (%)
SLG	4.5	8-9	Cannot withstand temperature>550°C	20.3
Alkali free aluminosilicate glass	-	-	Requires PDT of alkali ions	21.7
Corning 7059 (alkali free)	-	4.6	Low TEC	18.7
Titanium (Ti)	4.5	8.6	Requires NaF precursor	17.9
Aluminium (Al)	2.7	23-24	Low cost, lightweight, but high TEC	--
Molybdenum	10.2	4.8-5.9 (20-600°C)	High density and costly	11.7
Copper tape	8.9	16.6	High density and TEC	9.0
Ferric Cr- Steel	7.7	10.5	Requires Fe/Cr diffusion barrier	9.6
Thin glass	2.5-2.7	4.5-7.2	Low mechanical strength and brittle	-
Polyimide	1.4	20-40	Low operating temperature	20.4
Upilex®	1.4	12-24 (20-400°C)	<500°C operating temperature	18.7
Kapton®	1.4	17 (20-200°C)	<500°C operating temperature	--
Ni/Fe alloy eg. Kovar®	8.2	5.9-11	Phase transformation at T>400°C; requires diffusion barrier	10.6
Stainless Steel	8	10-11	Fe diffusion provides adverse effects	17.7
Zirconia-based Ceramic sheet	5.7	9.9	Requires Na precursor	17.7

Metallic and alloyed substrates such as titanium, aluminum, silicon, stainless steel, and molybdenum sheets or foils have been largely employed as substrates for CIGS solar cells. Metallic substrates can be used up to the processing temperature of 600 °C, without undergoing device failure.[105] However, several issues negatively affecting the device performance have been observed for the metallic and alloyed substrates. For example, the efficiency obtained for solar cells deposited onto metallic substrates (Ti) is found to be lower than on SLG, which is attributed to the poor quality of the absorber layer due to Na deficiency. It necessitated the deposition of a NaF layer to compensate for the Na deficiency. However, for a thicker NaF layer, the overlayers get peeled off due to poor adhesion.[103] Furthermore, undesired diffusion of impurity ions from metallic and alloyed substrates such as Fe from Fe/Ni alloy, Fe and Cr from stainless steel, and Ni and Co from ferritic steel substrates reduced the cell efficiency. To reduce this diffusion of impurity atoms, a diffusion barrier such as Cr, ZnO, or Al_2O_3 was required to be deposited onto the substrate prior to the growth of the CIGS layer.[103,105,107,108] There have also been additional problems such as back contact cracking and poor adhesion of films for the films grown on metallic substrates, which required more specialized processing to circumvent these problems.[109] In an alternate approach, Na silicate (SiO_x:Na) composite deposited using a sol-gel technique is used as a diffusion barrier as well as a source of Na to enhance the performance of CIGS solar cells on an unalloyed steel substrate.[110] For the steel-NaF sample, the positive contribution of Na (the "Na effect") is counterbalanced by the negative effect of Fe impurities homogeneously dissolved in the CIGS grains.[65] The record efficiency for flexible CZTS solar cells is 8% on Mo foil as a substrate with the NaF precursor layer deposited as an alkali source.[111] Sun *et al.* reported an efficiency of only 4% for CZTSSe based solar cells on titanium substrate achieved with the incorporation of Sb in CZTSSe layer.[112]

Apart from metals, polymer substrates such as polyimide, kapton®, upilex®, mylar, etc. have also been used as substrates due to their lightweight, low cost, smooth surface, and chemical inertness leading to a versatile use of solar cells in mobile devices, aircraft, window-panes, etc.[106] However, low thermal stability, poor mechanical strength, and a high coefficient of thermal expansion need a low-temperature growth of thin films. This demands a low temperature (< 500 °C) processing of CIGS or CZTS thin films, often resulting in low-quality absorber layers. Alternatively, some groups have employed lift-off processes to prepare solar cells on plastic substrates. Tiwari *et al.* reported a lift-off process to obtain an efficiency of 12.8% for CIGS solar cells on polyimide Kapton®. In this lift-off approach, a dissolvable NaCl buffer layer is deposited in-between glass substrate and Mo-coated polyimide which is dissolved in water, in order to separate the solar cell stack from the glass substrate.[113] Basol *et al.* has reported a device efficiency of ~8% for CIS based thin film solar cell deposited on Mo-coated Kapton® substrate.[114] The efficiency could be improved in the cases where efficient incorporation of alkali ions was carried out.[106,115,116]

On the other hand, rigid glasses, especially SLG have been the excellent choice as substrates in thin film solar cells. The efficiency of thin film solar cells on SLG substrates has been better than those grown on non-glass substrates using exactly the same deposition process.[52,117] The main reason for the better efficiency of the cells on the SLG substrates is due to the Na ions those out-diffuse from the SLG substrates as SLG acts as a reservoir of Na. Owing to the presence of the Na ions, a better growth pattern of the CIGS films is observed on the SLG substrate in comparison to those on the borosilicate glass, sintered-alumina, and sapphire substrates.[83] For the “alkali-free” glass substrates, an additional process step to facilitate Na incorporation into the absorber layer in the form of deposition of a NaF layer was required. For

example, Salome *et al.* reported 17.7 % efficiency on NaF deposited CIGSe solar cells on alkali-free glass from Corning Inc., which is comparable to that obtained on SLG (~17.6%).[118] On the other hand, Haarstrich *et al.* reported CIGSe solar cells on special high temperature sodium-containing glasses from AG Schott, Mainz with an efficiency of 17.6%.[119] Owing to the beneficial impact of Na, the SLG expectedly has exhibited high efficiency of 20.3% for CIGS and 12.6% for CZTS solar cells (highest to date), respectively.[49,66] Although, a record efficiency of 20.8% and 22.6% is reported for CIGSe grown on "high-temperature alkali-free aluminosilicate glass" the process included a post-deposition treatment (PDT) of alkali ions (K and Rb, respectively).[45]

The presence of other alkali's (i.e., K and Li) other than Na are expected to show similar beneficial effects.[120] A few groups have investigated the role of these alkali ions on the quality of the films by incorporating those ions externally via pre/post-deposition treatments of the absorber layers.[45,82,121,122] While the conventional route (i.e., diffusion of alkali ions from the substrate) offers a scalable approach as it simplifies the process steps considerably, detailed studies on the synthesis of glasses with varied compositions that can support the out-diffusion of alkali ions are very scarce and forms the basis of this thesis.

2.3. Glasses containing alkali oxides

As discussed above, the glass substrates with specific properties are highly desired for thin film solar cells and the desired characteristics are highly dependent upon the composition. Alongside this, the particular requirement for alkali diffusion in solar cell thin films needs to be fulfilled. In view of these requirements, the composition-property correlation of various alkali and alkaline-earth oxide modified silicate and borosilicate glasses are reviewed and given in **Table 2.2.**

Alkali oxide containing glasses have been studied for decades, but still remain to be a hot topic of research owing to their properties which make them versatile for use in various fields of applications. The review in Table 2.2 highlights the strong dependence of optical, thermal, mechanical, and electrical properties on the composition of glasses. With the change in the type of alkali oxide, the glass transition temperature varies from 450-650 °C. Alkali oxide content introduces ionic conductivity in the silicate glasses. The percent composition of SiO_2 and B_2O_3 determines the network strength and the relative range of values for TEC and hardness. CaO acts as an additive in sodium silicate glasses to alter the network and enhance diffusion. The mixed alkali effect leads to the non-linearity in properties that are affected by the transport mechanism of alkali ions. Although numerous alkali oxide containing compositions have been studied for various applications, designing of glasses that can facilitate the diffusion of alkali ions from it to the overlayer in CIGS/CZTS thin film solar cells is rarely found.

Table 2.2: *Overview of composition-property correlation of alkali and alkaline earth modified borate, silicate, and borosilicate glasses presented in a chronological manner.*

Modifier	Composition	Study	Remarks	Ref.
Na, K	$(1-x)Na_2O$-xK_2O-$2SiO_2$; x= 0 to 1	Alkali leaching in mixed alkali glasses	Diffusion coefficient for alkali ions varied with composition as $D_K>D_{Na}$ for $x>0.6$ and $D_K<D_{Na}$ for $x<0.6$	[123]
Li, Na	$20Na_2O/Li_2O$-$80SiO_2$	IR reflectivity	Peaks corresponding to Si-O-Si and Si-NBO linkages were identified in the presence of Li and Na modifiers.	[124]
Na	$KSiO_2$-B_2O_3-RNa_2O; $R=Na_2O/B_2O_3$; $K=SiO_2/B_2O_3$; K=0.5 to 6; R=0.2 to 5	Structural variation using XPS	Na_2O was proportionally distributed to silicate network and tetrahedral borate units explained by a new sharing model.	[125]
Na	Na_2O-CaO-P_2O_5-K_2O-MgO-B_2O_3-SiO_2	Structural studies using FTIR and XPS	Shifting of Si2p and O1s to lower binding energy owing to addition of Na modifier ions	[126]
Na	$9.4Na_2O$-$25.4B_2O_3$-$65.2SiO_2$-xCaO; x= 0 to 15	Ca as additive in sodium borosilicate glasses	For Ca<3.3%, the behaviour of Ca is similar to Na. On increasing Ca>3.3% Si-O-CaO-B or Si-O-CaO-Si units were formed. Four coordinated boron units become saturated.	[127]
Na	$72.6SiO_2$-10.2CaO-$15.9Na_2O$-$1.3Al_2O_3$	Diffusion and leaching mechanism of Na ions	Diffusion mechanism was not purely Na-self diffusion. Inter-diffusion process was influenced by proton exchange mechanism. $D=2.4\times10^{-18} m^2/s$ and activation energy 79.8kJ/mol obtained from solution of diffusion equation.	[128]
Li	xLi_2O-$(1-x)(0.5B_2O_3$-$0.5SiO_2)$; xLi_2O-$(1-x)(0.5B_2O_3$-$0.5P_2O_5)$	Conductivity	Max ionic conductivity of 2.4×10^{-8} S/cm at RT. Phase formation due to heat treatment at 600°C lead to increase in conductivity. Lithium borosilicate	[129]

			system had stable glass forming ability and chemical properties;	
Na	SiO_2-B_2O_3-Na_2O; $12<Na_2O<35$	Conductivity	E_a varied from 0.67 to 0.91eV with decreasing Na content. T_g~770-840K	[130]
Li, Na, K	$62SiO_2$-25-B_2O_3-$1.2Al_2O_3$-5.4CaO-6.4-R_2O; $62SiO_2$-25-B_2O_3-$1.2Al_2O_3$-5.4CaO/MgO/ZnO-3.2-Na_2O-$3.2Li_2O$; R=Li, Na, K	Dielectric and thermal properties	T_g varies from 495 to 540 °C Dilatometric softening temperature (T_d) upto 705 °C TEC varies from 5.4-6.7, Dielectric constant~5-6 (at 10MHz) Resistivity ranges in $0.73\text{-}1.17\times10^{13}$ ohm-cm	[131]
Li, K	$(30-x)Li_2O$-xK_2O-10CdO/ZnO-$59B_2O_3$; x= 0 to 30	Mixed Alkali effect from IR and Raman Spectroscopy	T_g increases non-linearly IR band intensities corresponding to BOB linkages exhibit non-linear variation Various BO_4 tetrahedra, boroxol ring and pentaborate bands identified	[132]
Na	$x$$Na_2O$-$(100-x)SiO_2$; x=22.5, 39.8, 43.1	Arrangement of structural units using multinuclear NMR	Na is homogeneously distributed in the silicate network with sites close to NBOs as well as BOs The bond angle of Si-O-Si linkages reduces with the presence of Na in the periphery	[133]
Na, Li	$81SiO_2$-$12B_2O_3$-$(6-x)Na_2O$-0.5 CaO-$0.5Al_2O_3$-xLi_2O	Viscosity	Viscosity and hence T_g of glasses reduces with increase in concentration of Li	[134]
Na	$(75-x)SiO_2$-xB_2O_3-10CaO-$15Na_2O$; x=0,15,37,50,75	Density and micromechanical properties	B15 with 15 mol% B_2O_3 exhibits highest T_g (843K), density (2.55g/cc) and Vicker's Hardness (6.1GPa)	[135]
K	$55SiO_2$-$10K_2O$-$(35-x)$CaO-xMgO	Optical bandgap	E_g~3.7eV, higher electronegativity of MgO caused higher E_g	[136]

Na	SiO_2-B_2O_3-Na_2O; 12<Na_2O<35	Hardness and toughness	With the decrease in Na, T_g~500-580°C; Elastic modulus-72-82GPa; Poisson ratio-0.212-0.264; Glasses with higher former concentration exhibited higher hardness (7.2GPa)	[137]
Li, Na, K, Cs	55SiO_2-24B_2O_3-20R_2O	Thermal properties and Ionic conductivity	With the increase in size of alkali ion, T_m~1373-1573K; T_g~781-873K; E_a~0.67-0.98eV	[138]
Li	55SiO_2-30B_2O_3-*x*Y_2O_3-(15-*x*)Li_2O	Thermal and optical properties	With replacement of Li_2O by Y_2O_3, E_g~3.6-3.9eV; T_g~550-610°C; For 15 mol% Li_2O, T_g was close to 535°C;	[139]
Na	(70-*x*)SiO_2-*x*Na_2O-15CaO-10Al_2O_3-5TiO_2; 10<*x*<25	Optical and thermal properties	T_g varied from 595 to 683°C with decrease in Na concentration TEC varied from 8.13-9.12ppm/K Optical band gap E_g~ 4.5eV lied in insulating range	[140]
Li	*x*Li_2O_3-5Al_2O_3-(95-*x*)B_2O_3; *x* = 5to 25	Thermal and physical properties	Phase separation was suppressed for 10-15 mol% Li_2O along with increase in T_g and T_s	[141]
Na, Cs	*x*Na_2O-*y*Cs_2O-3B_2O_3; *x=0 to 1, x+y=1*	Local structure investigation in light of mixed alkali effect	Average coordination number of Na (6) and Cs (8-9) cations decreased with increasing Cs/(Na+Cs) ratio Fraction of 4 coordinated boron reduces while that of 3-coordinated boron increases on replacing Na by Cs.	[142]
Li	40Li_2O-40B_2O_3-20SiO_2-Li_2SO_4	Electrical conductivity	T_g~470C; T_c-630°C for base composition With addition of Li_2SO_4 conductivity increased, and glass ceramics were formed with lowered T_g	[143]
Na	(75-*x*)SiO_2-*x*Al_2O_3-25Na_2O, *x*=0,5,10,15,20,25	Role of NBO's	No. of NBO's/tetrahedral decreased to zero with increase in Al_2O_3 concentration as each Na compensated for the conversion of trigonal coordination of Al to tetrahedral Hardness increased non linearly from 3.6 to 6 GPa	[144]

			Area under Q^4 bands increased while that for Q^2,Q^3 decreased	
Ca	30-SiO_2-30B_2O_3-10Y_2O_3-(30-*x*)CaO-*x*ZrO_2; *x*=2.5 to 10	Optical and dielectric properties	Higher CaO concentration induced lower density, higher optical band gap and high dielectric constant	[29]
Na, K	30CaO-25Na_2O-45P_2O_5	Electrodiffusion and chemical diffusion using Bombardment induced ion transport	K^+ bombardment induced ion exchange with inward diffusion of K and outward electrodiffusion of Na and Ca ions. Out-diffusion of Na and Ca ions was concentration dependent. Chemical diffusion was accompanied by the change in local structure for phosphorus oxide network. The inter-diffusing ions were blocked by the already present cation on diffusion front.	[145]
Li, Ca	0.4[(1-*x*)Li_2O-*x*CaO]-0.6[(1-*y*)B_2O_3-*y*SiO_2]	Mixed modifier effect	Negative non-linearity in 4-coordinated Boron resulted in similar effect in T_g, T_s and Hardness. Non linearity in dielectric constant and activation energy were attributed to the inhibited modifier transport while substituting Li_2O with CaO.	[146]
Na, Ca	73SiO_2-5Al_2O_3-(22-*x*)Na_2O-*x*CaO; *x*=0,7,11	Glass network effect on water transport in glass	Diffusion/water transport is influenced by the complexity of glass network and composition. While presence of calcium strengthened the glass network and reduced the density of bottlenecks to enhance diffusion, the introduction of boron caused the chemical interaction	[147]
Mg,Ca, Sr, Ba	25RO-20Al_2O_3-55B_2O_3	Hardness and crack resistance	T_g~554-636°C Higher field strength of alkali-earth modifiers resulted in higher hardness and increase in T_g owing to stronger modifier-NBO bond	[16]

Na-K	$22.7R_2O$-$77.3SiO_2$; N_2O/K_2O=0,0.5,1; R=Na_2O or K_2O	Origin of MAE from MDS and structural properties	Local environment in silicate glass had highly coordinated K-O polyhedra compared to four coordinated Na-O polyhedra which disturbed the ion migration Fraction of Si-O ring size with n=13 was highest for K100 glass with higher cavity volume ratio. Smaller size cavity in N50K50 glass prevented the migration of K-ions.	[148]
Na	$0.33Na_2O$-$0.67[xB_2O_3$-(1-*x*)2SiO2]; *x=0 to 1*	Mixed glass former effect in Na-ion conduction	Negative mixed glass former effect (MGFE) on the conductivity of Na^+ ions (up to 300°C) with positive effect on density, T_g and mechanical moduli of sodium borosilicate glasses	[149]
Na-K	*x*Na_2O-(20-*x*)K_2O-$30V_2O_5$-$50TeO_2$; *x=0,5,10,15,20*	ac conductivity and dielectric studies in light of mixed alkali effect	T_g~233-238°C; dielectric constant ~ 1.5 to 5 with change in frequency; Dielectric and conductivity indicated the presence of dynamic processes dependent of temperature and composition. *x*=10 mol% glass exhibited minima in T_g attributed to mixed alkali effect. Correlated barrier hopping mechanism responsible for transport mechanism in glasses.	[150]

2.4. Motivation

The literature review presented above shows the positive impact of the incorporation of alkali atoms such as Na, K, Li on absorber layers in CZTS or CIGS based thin film solar cells. The diffusion of the Na from the substrate to the overlayers has been shown to be a facile route of incorporation of Na in the absorber layer and has routinely yielded high efficiency for the solar cells. However, such a study is not available for K and Li. Despite the simplicity and the potential of this approach (i.e., diffusion of the alkali ions from the substrate to the overlayers) of alkali ion incorporation, there have been very limited studies related to the synthesis and preparation of specialized glasses for solar cell/ microelectronic applications. No study has been carried out to investigate the effect of Li, Na, and K systematically, as well as individually, or in combinations (mixed alkali effect), on the Mo layer for solar cell applications. Based on the literature survey, the objectives of the present research proposal are given below.

2.5. Objectives

- To synthesize $65SiO_2$-$5B_2O_3$-15CaO-(15-x)Na_2O-(x)Li_2O/K_2O (x=0-15) glasses.
- Structural, physical, thermal, and optical properties of these glasses will be studied using XRD, FTIR, TGA/DTA, dilatometry, and UV-Visible spectroscopy.
- As prepared glasses will be used as a substrate to deposit Mo layer and study the response of various constituents on diffusion alkali cation in the Mo layer.

Chapter 3 Experimental details

This chapter contains the experimental techniques used for the preparation of glasses as substrates and Mo thin film for the desired study. This chapter also contains details of the various techniques used for the characterization of the glasses and thin films.

3.1. Synthesis of glasses

The glasses with composition $65SiO_2$-$5B_2O_3$-15CaO-(15-*x*) Na_2O-*x*R_2O (R= Li, K) (*x*=0, 5, 10 and 15) were synthesized using the melt-quench technique. The detailed composition of synthesized glasses is given in **Table 3.1** below.

Table 3.1: *Composition of synthesized glasses in mol% along with their sample ID.*

Sample ID	**SiO_2**	**CaO**	**B_2O_3**	**Li_2O**	**Na_2O**	**K_2O**
NCS	65	15	5	0	15	0
NL05	65	15	5	5	10	0
NL10	65	15	5	10	5	0
LCS	65	15	5	15	0	0
NK05	65	15	5	0	10	5
NK10	65	15	5	0	5	10
KCS	65	15	5	0	0	15

Chemicals used such as silicate (SiO_2), calcium oxide (CaO), boron trioxide (B_2O_3), sodium carbonate (Na_2CO_3), lithium carbonate (Li_2CO_3), and potassium carbonate (K_2CO_3) were of analytical grade from Loba Chemie, with the purity of all the chemicals ≥ 99%, in powder form. NaCl is used as a fining agent with an extra 3 wt%. The homogeneous mixing of raw materials in stoichiometric proportions is carried out using agate mortar pestle for 1 hour (h) in acetone medium. The grounded mixture of glass batch is poured into alumina crucibles and kept for drying overnight at 120 °C in the oven. The alumina crucibles were rinsed with dil. HCl followed by distilled water and dried in the oven at 120° prior to use. The reagents were thoroughly mixed and kept in a

programmable high resistive furnace for melting at 1550 °C. The graphical representation of the furnace program is as shown in **Fig. 3.1**

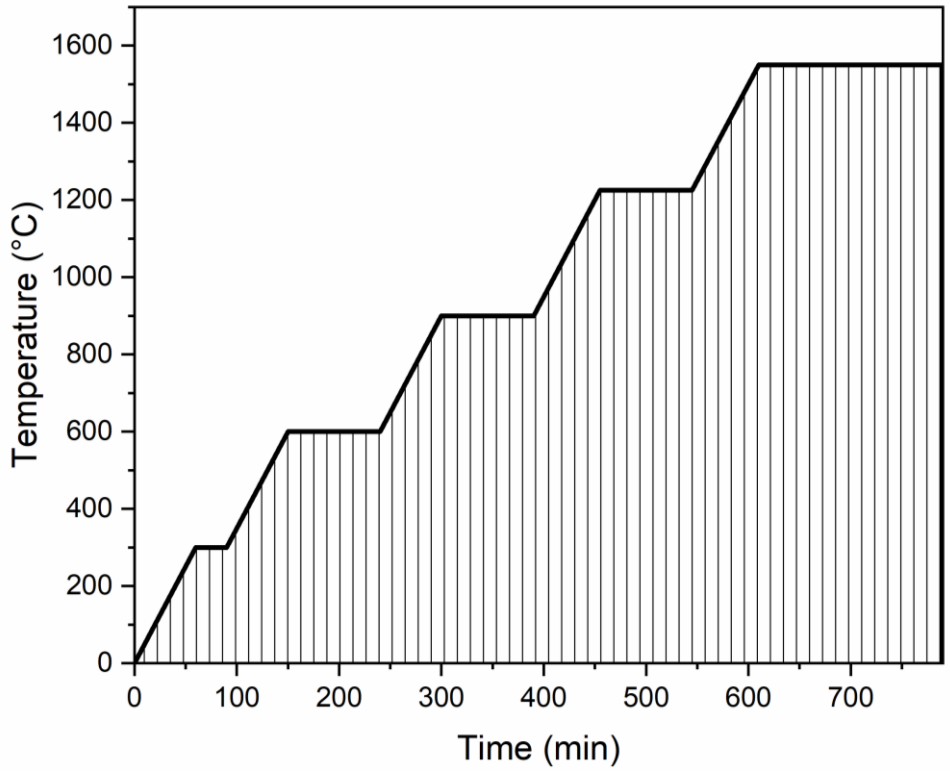

Figure 3.1: *Schedule followed for the melting of glass samples.*

The furnace was so programmed to heat at the rate of 5°C/min with a holding of 90 minutes at 300, 600, 900, and 1225°C to allow decomposition of carbonates into oxides. The resultant evolution of CO_2 (g) helps in the homogenization of the reagent mixture.[5] The glass batch was finally melted at 1550 °C held for 30 min, followed by splat quenching between copper plates. The glasses so obtained are annealed in a pre-heated oven at 400°C for 6 h for releasing the stress induced while quenching. For some of the investigations, the glass frits so obtained are finely grounded in an agate mortar pestle to form a fine powder.

The composition of commercially available SLG has been estimated using Scanning Electron Microscopy-Energy Dispersive X-Ray Spectroscopy (SEM-EDS), as $74SiO_2$-7CaO-$15Na_2O$-4MgO.

3.2. Preparation of substrates

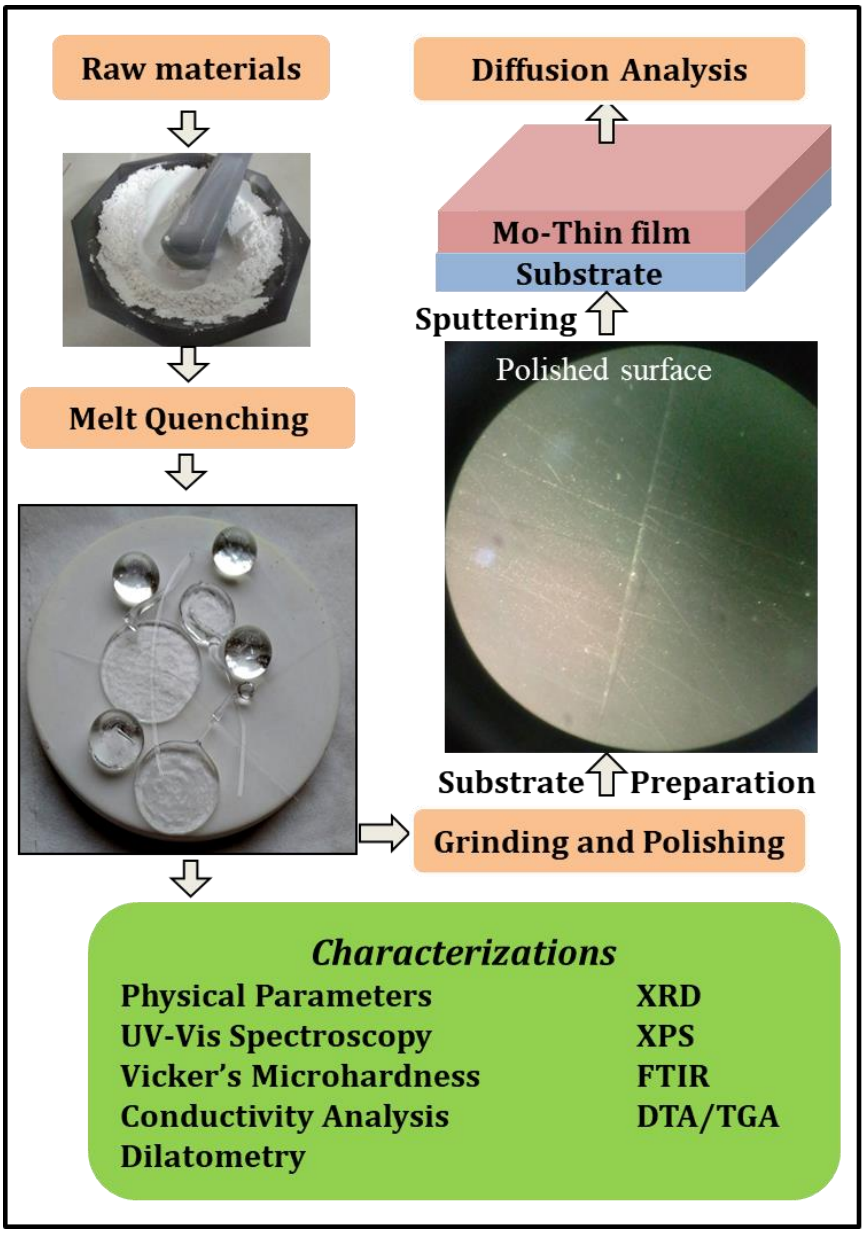

Figure 3.2: *Flow chart representing the method of glass preparation and characterization.*

The annealed glass pieces were cut into pieces using a diamond cutter (Buehler Isomet) and ground on an emery sheet of 400/600/1000/1200/1500/2000 grades consecutively, to achieve a smooth surface. The mirror-like surface finish was obtained by polishing them with a diamond paste of 6-micron grade followed by 1micron for 20 min. The polished glass samples were cleaned with ethanol, followed by ultrasonic cleaning for 10 min, and final cleaning with isopropyl alcohol (IPA) to be employed as a

substrate for sputter deposition of the molybdenum thin film. The flow chart of the complete process is given in **Fig. 3.2.**

3.3. Characterization of synthesized glasses

3.3.1. Measurement of density

The density of the as-quenched glass samples is measured using microbalance on the basis of Archimedes' principle using xylene as buoyant:

$$\boldsymbol{\rho_{sample}} = \frac{\boldsymbol{w_a}}{\boldsymbol{w_a - w_b}} \times \boldsymbol{\rho_{xylene}} \quad \textbf{(3.1)}$$

Where ρ_{sample} is the density of the sample, ρ_{xylene} is the density of xylene, w_a is the weight of sample in air, and w_b is the weight of the sample in xylene.

3.3.2. X-ray diffraction (XRD) study

XRD measurements were carried out for the analysis of the structural characteristics of the samples. In the present study, the XRD of the finely powdered glass samples was carried out by, using PANalytical X'Pert PRO system with Cu- K_α radiations (λ=1.5406Å) @ scan rate of 2° min^{-1} in the range of 10-80° diffraction angle. For amorphous materials, the XRD pattern exhibits a broad hump, while for crystalline materials, sharp peaks are observed at Bragg's angle (2θ) corresponding to the diffraction planes characteristic of the crystal structure of the material. The crystallite size (D) can thus be determined using Debye Scherrer's equation

$$\boldsymbol{D} = \frac{\boldsymbol{K\lambda}}{\boldsymbol{\beta cos\theta}} \quad \textbf{(3.2)}$$

where, K is the dimensionless shape factor (~0.9), λ is the wavelength of the monochromatic x-ray, β is the full width at half maxima (in radians) and θ is the Bragg's angle. It is further employed to find out the strain in the crystal structure to due synthesis parameters.

3.3.3. Fourier transform infrared (FTIR) spectroscopy

The FTIR spectroscopy is an advanced method of data acquisition based on the interference pattern generated by the interaction of infra-red radiations with a given sample. The collected data are transformed into a spectrum. Infrared radiation incident on the sample gets partially absorbed and partially transmitted. The spectrum so-obtained represents the bands corresponding to the molecular vibrations of specific chemical bonds which are a fingerprint of the particular bond. Thus, we can identify the types of chemical bonds present in the material. The FTIR spectroscopy of the present glass samples is performed using Nicolet iS10 spectrophotometer over the range of 400-2000 cm^{-1} by making pallets using KBr.

3.3.4. X-ray photoelectron spectroscopy (XPS)

The XPS is a surface sensitive technique to precisely estimate the chemical state of elements. The sample material is irradiated with X-rays (hν) to eject out photoelectrons from the core-levels of the element. The kinetic energy (KE) of the ejected photoelectrons is measured to calculate the binding energy (BE) given by

$$\boldsymbol{BE = h\nu - KE - \emptyset_s} \qquad \textbf{(3.3)}$$

where, $\emptyset_s$is the spectrometer work function. The binding energy of electrons in the inner shell is a unique feature of an element, and its values are tabulated well in literature.[151] Thus, a shift in the BE of any element provides information about its chemical state in the material network. However, a shift in peak is also observed due to the sample charging effect. To compensate for this shift, a correction is applied. C1s peak due to the presence of carbon monolayer in vacuum on the surface of the samples has standard binding energy of 284.8eV. Therefore, it is adjusted to this value to correct the BE for other elements.

In the present work, XPS was performed on selected glass samples using an X-Ray Photoelectron Spectrometer (model: PHI VersaProbe II with AES). The XPS measurements were carried out with monochromatic AlKα radiation (hν=1486.60 eV). The purpose of XPS analysis was to understand the effect of different alkali ions on the chemical state of elements in the random glass structure.

3.3.5. UV-vis spectroscopy

The UV-vis spectroscopy is based on the interaction of samples with electromagnetic radiations in the ultraviolet, visible, and near-infrared regions. The absorption, reflection, and transmission of UV-vis radiations incident of the sample depend on the electronic transitions occurring within the sample. The elements or compounds absorb radiations corresponding to the optical bandgap energy of the material and various electronic transition or defect states. On the other hand, the reflection and transmission spectrum gives information about the optical properties of samples such as % reflection and transmission of visible radiations.

In the present dissertation, the polished glass samples are used to perform UV-visible spectrophotometry in transmittance mode using SHIMADZU (U-2600) spectrophotometer with a spectral range from 190-800 nm. Beer-Lambert's relation is used to calculate the absorption coefficient from transmittance with the change in wavelength

$$\boldsymbol{\alpha = \frac{1}{d}\left(\ln\left(\frac{1}{T}\right)\right)} \qquad \textbf{(3.4)}$$

where, α is the absorption coefficient, d is the thickness of the sample and T is the transmittance[152].

Tauc's equation is applied to calculate the direct optical band gaps in the present glasses. $[\alpha h\nu]^n$ versus band energy (hν) is plotted to obtain the optical band gap value for

direct-allowed transitions with n=2 by extrapolating the straight-line portion to $[\alpha h\nu]^n = 0$. Refractive index for the glasses is studied from the transmittance spectra as below

$$\boldsymbol{n = \left[1 + (1 - T^2)^{1/2}\right]/T} \qquad \textbf{(3.5)}$$

3.3.6. Differential thermal analysis (DTA)

The DTA is an analytical technique used to study the thermal phase transitions in the given material. In this differential technique, thermal characteristics of a sample are measured with reference to standard material, resulting in exo- and endothermic characteristic peaks in differential temperature plotted with respect to the temperature, corresponding to the crystallization and melting of the sample respectively. Moreover, the thermal transition before crystallization is a characteristic of glass transition temperature.

In this dissertation, thermogravimetric/differential thermal analyzer (TG/DTA) from Perkin Elmer (model: Diamond Pyris) equipment is used to estimate the glass transition temperature (T_g) of the glasses. Thermal analysis of powdered glass samples was performed at a heating rate of 10°C/min from 50 to 800 °C under N_2 atmosphere.

3.3.7. Thermal dilatometric analysis (TDA)

The linear and volumetric expansion of a sample with respect to temperature is measured using Dilatometer. It is a sensitive instrument based on the measurement of linear expansion in the material with respect to time and temperature. The variation in the slope of the curve denotes the transition temperature of the material, and the slope of the straight line corresponds to the coefficient of thermal expansion (TEC) of the sample. For glass samples, the dilatometric analysis provides various thermal characteristics such as TEC, dilatometric glass transition temperature (T_g), and dilatometric softening temperature (T_d).

In this work, the dilatometric analysis was carried out using Netzsch DIL 801 L dilatometer in the temperature range of 100-600°C at the heating rate of 5°C/min. The

synthesized glass samples of thickness 2-3mm and diameter~5cm were polished on both sides to carry out the dilatometric measurement.

3.3.8. Vicker's microhardness testing

The mechanical properties such as hardness (H) and fracture toughness (K) of the ceramic samples are analyzed using Vicker's microhardness tester. In this technique, the known value of the load is applied to the sample for a fixed time duration (a few seconds) with the help of an indenter. The size of the indent is measured to calculate the hardness.

In this dissertation, Vicker's microhardness tester (Mitutoyo, Japan) is used to test the hardness of the samples using a diamond indenter with a pyramidal base of the apical angle of 136°, by applying a 300g of load with an indentation span of 15sec. Vicker's microhardness (H) is calculated for the samples using

$$\boldsymbol{H = \frac{1.8544 \times F}{d^2}} \qquad \textbf{(3.6)}$$

where, F is load in kgf (0.3 kgf) and d is the diagonal length of the indentation in mm.

3.3.9. Impedance analysis

Impedance spectroscopy is a powerful technique to investigate the frequency and temperature dependence of the electrical properties of the ceramic samples. The disk-like sample mounted between the electrodes act as an RC circuit. The resistive-capacitive measurement gives the output in the form of real and imaginary permittivity and impedance. The ac conductivity is thus obtained with respect to frequency and temperature, to understand the transport properties of ions in the glass material.

In the present work, a set of polished glasses is Platinum coated on both sides using a 3000-FC auto fine coater from JEOL to form a parallel plate capacitor with prepared glasses as a dielectric medium. The electrical properties of the glasses were studied using an impedance analyzer from SOLARTRON (SI-1260). The frequency and

temperature dependence of relative permittivity and conductivity were studied in the frequency range of 100Hz-1MHz at temperatures ranging from 25-600°C, respectively.

3.4. Sputter deposition of Mo film

The Mo films were deposited by DC magnetron sputtering using a water-cooled high purity (99.99%, Tredmann Pvt. Ltd., Taiwan) target of 2-inch diameter on to soda-lime glass substrates held at room temperature. In this sputter system, the substrates were inclined by about 30° with respect to the normal of the sputtering target. The distance between the centers of the target and substrate was about 10 cm. The substrate holder was rotated at 8 rotations per min about its axis. A turbomolecular pump backed by a rotary pump was used to evacuate the chamber to base pressure lower than 5.0×10^{-6} mbar. The deposition was carried out at various DC power ranging from 50-100 W and at Ar pressure of either 2.6×10^{-2} mbar (high pressure deposition, HPD) or 2.6×10^{-3} mbar (low pressure deposition, LPD). The details of single and bi-layered Mo films are listed in **Table 3.2**. The flow of Ar into the chamber was controlled by a mass flow controller at 30 standard cubic centimeter per minute (SCCM) and the sputtering pressure was maintained by adjusting the throttle valve.

Table 3.2: *Sputter-deposition conditions of Mo-thin films.*

Sample ID	**Deposition condition***		
	DC power (W)	**HPD time (min)**	**LPD time (min)**
100 W (20/0)	100	20	0
100 W (20/30)	100	20	30
75 W (20/30)	75	20	30
50 W (20/30)	50	20	30
50 W (30/30)	50	30	30
75 W (20/40)	75	20	40

The substrate was ultrasonically cleaned first in deionized-water for 10 min and then in isopropyl alcohol. The substrates were then dried by blowing hot air. For a direct comparison of Na depth profiles, we have deposited Mo films on the commercial SLG substrates and on synthesized glass substrates (as mentioned in T**able 3.1** and section 3.2 above). In most of the CZTS based thin film solar cells, a post-sulfurization of about 500 °C has been required to form phase pure high-crystalline CZTS films. In view of this, some of the samples (i.e., bi-layered Mo on glass substrates) were vacuum annealed at 500 °C in flowing Ar.

3.5. Characterization of the Mo thin films

3.5.1. Field emission scanning electron microscopy (FESEM)

The FESEM is a sophisticated technique to study morphology of the samples. The sample of conducting nature is perturbed by a beam of electrons of the energy range 10-30keV. Sample-electron interaction leads to the emission of secondary electrons caused by inelastic scattering, back-scattered electrons resulting from elastic scattering, and x-rays emitted from the inner core of the sample. The secondary electrons are used to create an image of the surface morphology of the sample showing grains and grain boundaries to the magnification of 5kX to 60kX. In the present dissertation, the surface and cross-sectional microstructure of Mo-thin films coated on the top surface with gold coating was studied using FESEM (Hitachi SU8000).

3.5.2. Secondary ion mass spectroscopy (SIMS)

The SIMS is a sophisticated technique to measure the variation in elemental concentration over the depth of a sample. The SIMS was studied using a TOF-SIMS 5-100 (ION-TOF GmbH) system. Bismuth is used as a primary gun and O_2/Cs as the sputter gun. The resistivity of the films is calculated by a linear four-probe setup.

The deposited Mo film is vacuum annealed at 500 °C for 1hr to facilitate the ion-exchange mechanism. The depth profile of all the elements (Na, Mo, K, Li, Si, B) from substrate source to Mo film is studied using Hiden Analytical secondary ion mass spectrometer workstation (FG-300), equipped with oxygen sputter gun with 400 nA target current, 5 kV acceleration voltage and detector operated in positive ion mode. The raw data of intensity counts of ions with sputter time is converted into sputter depth estimated from the Mo-thickness of 1micron obtained from cross-sectional FESEM, attaining a resolution of ~2 nm. The measurement is carried out from Mo film on top towards the glass substrate.

The raw data obtained from SIMS consisted of the elemental depth profile of 6Li, 23Na, 41K, 32Si, and 97Mo representing the intensities/counts of particular elements from the surface of Mo-film towards the substrates. The raw intensities are normalized with respect to that of 97Mo for the purpose of comparison between different substrates. Selection of 97Mo for the purpose of normalization is due to the uniformity of Mo signal in the Mo-films, deposited onto each substrate in the exactly same condition and treatments, thus minimizing the error in relative intensities of specific alkali ions. The normalization step compensates for the analytical and instrumental artifacts that occur due to a slight variation in the sputter rate of the ions from a mass spectrometer on different samples. The relative intensity of particular alkali ion w.r.t. Mo at depth *x* is calculated as:

$$Normalized\ Li = \left[\frac{6Li}{97Mo}\right]_x = \frac{I_{Li}}{I_{Mo}}$$

$$Normalized\ Na = \left[\frac{23Na}{97Mo}\right]_x = \frac{I_{Na}}{I_{Mo}}$$

$$Normalized\ K = \left[\frac{41K}{97Mo}\right]_x = \frac{I_K}{I_{Mo}}$$

Where, I is the intensity of the respective element from raw data at a particular depth (*x*).

Chapter 4 Properties of synthesized glasses

As outlined in the previous chapters, this work aims to prepare the glasses with systematic intentional incorporation of Na/Li/K for their possible use as substrates in CIGS (or CZTS) based solar cells. Since, the diffusion of alkali ions and mechano-thermal properties of the glass substrates are strongly influenced by the local structure of the glass. So an in-depth understanding of the structural variation due to the incorporation of Li, Na, and K has played an important role to develop suitable substrate for thin film solar cells. In view of this, structural, thermal, mechanical, and electrical properties of synthesized glasses have been discussed in this chapter.

4.1. Effect of various glass constituents

4.1.1. Physical parameters

In order to understand the effect of local structure and composition of glasses on its physical, mechanical, optical, and dielectric properties, various theoretical parameters are calculated from the glass composition. The molar volume (V_m) of the glasses is estimated from molecular weight and density using the standard formula given below.[153]

$$V_m = \frac{\rho_{sample}}{Mol.\ wt.} \quad (4.1)$$

It is further used to calculate the ionic concentration of alkali ions present in glasses using the following equation:

$$N = \frac{N_A \times mol\%\ of\ cation \times valency}{molar\ volume} \quad (4.2)$$

Furthermore, the inter-ionic radius (referred to as the ionic radius between the respective alkali cation and oxygen anion) is also calculated from 'N' using equation (4.3).

$$r_i = (1/N)^{1/3} \quad (4.3)$$

The obtained values for the above mentioned physical parameters are given in **Table 4.1**. The table also contains the R-notation indicating the nature of a particular alkali ion present in the corresponding glass sample along with its field-strength (FS), estimated by

Quintas *et al.* for alkali ions in silicate glasses.[154] Field strength (Z/a^2, where 'Z' is formal valency and 'a' is the internuclear distance) of a modifier-ion is significantly responsible for alteration in the glass network. Lithium ion among the alkali ions exhibits the highest field strength owing to smaller ionic radii, whereas it decreases with the increase in ionic radii.

***Table 4.1**: Sample labels along with nature of alkali ion present (R), their corresponding field strength (FS) and physical parameters like molecular weight (M), density (ρ), molar volume (V_m), respective alkali-ion concentration (N) and inter-ionic radius (r_i).*

Sample ID	**R**	**FS/Å^2**	**M/gmol^{-1} ±0.0001**	**ρ/g cm^{-3} ±0.01**	**V_m/cm^3 ±0.01**	**N/(×10^{23})cm^{-3} ±0.01**	**r_i/(×10^{-7})cm ±0.001**
LCS	Li	0.26	55.4923	2.56	21.63	4.17	0.133
NCS	Na	0.18	60.2441	2.55	23.60	3.82	0.137
KCS	K	0.12	65.0773	2.50	25.97	3.47	0.142
SLG	Na	--	59.2330	2.53	23.41	3.84	0.137

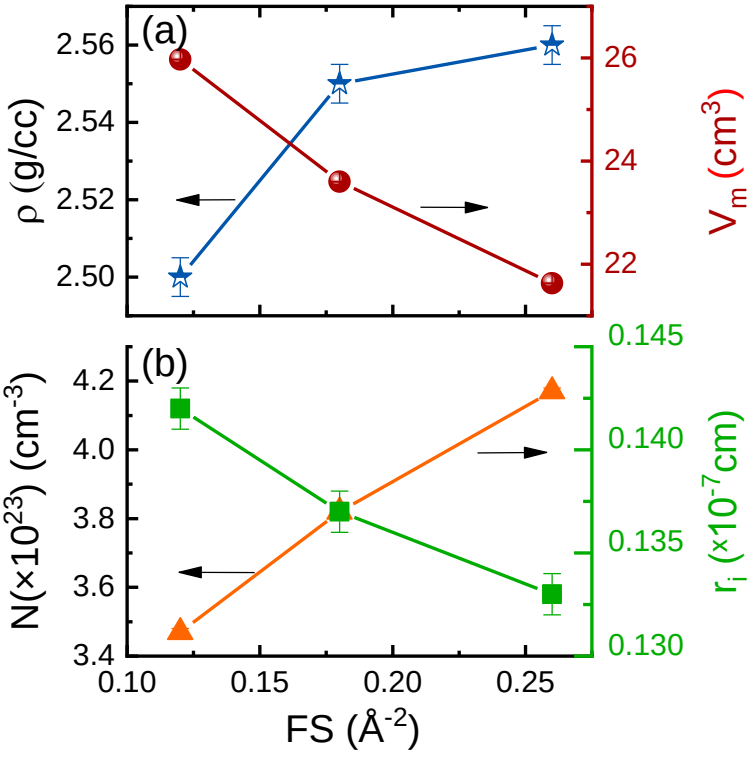

***Figure 4.1**: Effect of alkali ion field strength on (a) density (ρ) and molar volume (V_m); (b) alkali ion concentration (N) and inter-ionic radius (r_i).*

As shown in **Fig. 4.1(a)**, the density of the glasses is found to increase with the increase in field strength (FS) for different alkali oxide containing glasses, whereas the molar volume decreases. The alkali ion concentration per unit volume of the glasses is found to decrease with the substitution of heavier alkali ion, whereas the inter-ionic radius increases **[Fig. 4.1(b)].** The lower the field strength of the cation, the higher is the inter-ionic radius. These values are in close agreement with similar soda lime silicate glasses and commercially available SLG, as mentioned in **Table 4.1**.[130,135] These parameters are discussed in detail in the following sections.

4.1.2. XRD analysis

Figure 4.2 represents the XRD patterns of the synthesized glasses along with SLG. The patterns are characterized by a broad halo in the region 20-30° confirming the amorphous nature of the present glasses. The broadness of the halo is more for NCS glass, as compared to other glasses. This shows that the NaO containing glasses have a more heterogeneously distributed glass network of $[SiO_4]^{4-}$ units.

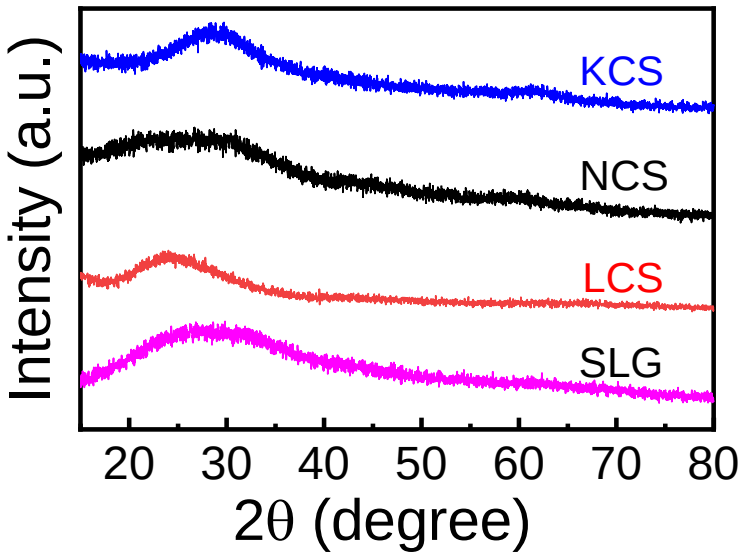

***Figure 4.2**: XRD patterns of different alkali oxide containing glasses and SLG.*

As modifiers are known to create non-bridging oxygens (NBO's) in the structure, the difference in field strength of Li, Na, and K ions **[Table 4.1]**[154] leads to distorted

asymmetrical local glass structure creating phase-separated regions.[155] As the field strength of modifier ions increases, it enhances the tendency of phase separation in the present glasses **[Fig. 4.1].** In comparison to the synthesized glasses, SLG exhibited a well-shaped broad halo, representing a uniform distribution of local structural units. In order to investigate devitrification in representative NCS glass, heat treatment was carried out at three different temperatures determined from DTA i.e. 735, 785, and 935 °C, respectively for 1 hour each. The XRD pattern of the heat treated glasses **[Fig. 4.3]** did not exhibit any devitrification up to 735 °C. Heat treatment at 785°C indicated some change in the XRD pattern that might be related to the growth of minor nanocrystalline phases characterized by the appearance of a halo around Bragg's angle of 40-50° and 55°. On treatment at 935 °C, the growth of the wollastonite phase ($CaSiO_3$) is observed in the glass matrix which nucleates within the silicate network due to lower mobility of Ca ions.[156–158] The role of Ca in silicate glass structure is further discussed in forthcoming sections.

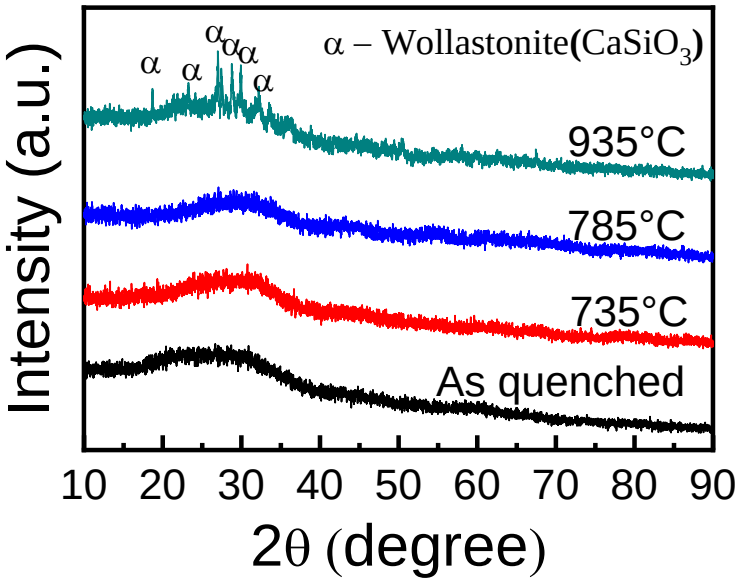

***Figure 4.3**: XRD pattern of as-quenched, and heat treated NCS glass at different temperatures.*

4.1.3. Fourier transform infrared (FTIR) spectra

The FTIR absorption spectra of the samples are presented in **Fig. 4.4**. The figure indicated several absorption bands in the mid-infrared region from 1600-400 cm^{-1} i.e fingerprint region. The broadband at 400-600 cm^{-1} corresponds to the Si-O-Si and O-Si-O bending mode vibrations in the SiO_4^{4-} structural units.[159] The asymmetric band ~600-800 cm^{-1} is assigned to the symmetrical stretching vibrations in Si-O-Si, Si-O-B, Si-O-Ca bonds present in different structural groups in the glasses.[158] A broad and intense band ~900-1200 cm^{-1} illustrates the asymmetric stretching vibrations of SiO_4 tetrahedral units as well as trigonal and tetrahedral borate units.[159–161]

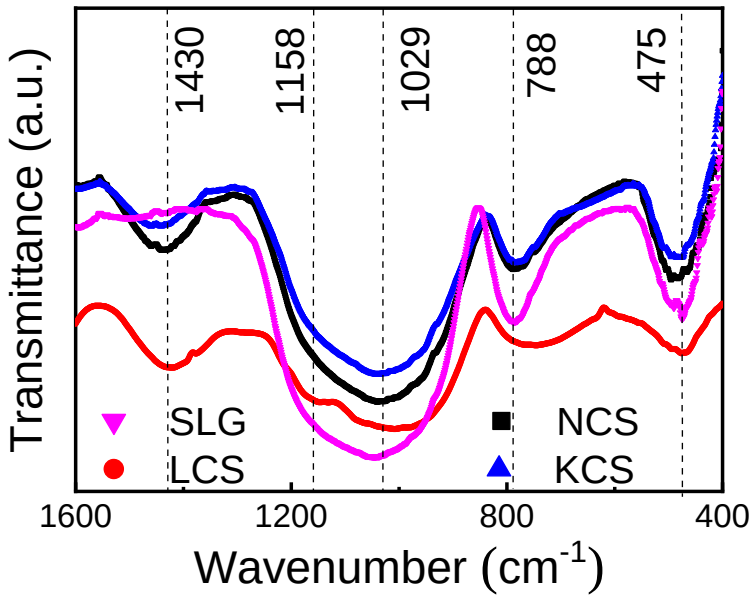

Figure 4.4: *FTIR spectra of the synthesized glasses with band labels corresponding to different vibration modes.*

In order to resolve the bands corresponding to different structural units, the deconvolution of the bands was performed by Gaussian fitting of FTIR spectra **[Fig. 4.5].** A small band ~1400 cm^{-1} observed only in the synthesized glasses is assigned to the stretching vibration of the B-O bond due to NBO attached with $[BO_3]$ arising from the boric oxide present as glass former in a small percentage.[162] The peak at 1165 cm^{-1} is assigned to the Si-O-Si bond stretching due to Q^4 units. The bands s corresponding to

1050, 970 and 930 cm^{-1} correspond to the silicate structural units with 1, 2, and 3 NBOs namely Q^3, Q^2, and Q^1 units.[163,164] These bands are found to shift towards lower wavenumber with the decrease in ionic radii of the modifier ion, i.e. highest for KCS and lowest for NCS. It indicates the weakening of the Si-NBO bond due to the presence of high field strength Li ions compared to low field strength K-ions. The bands close to 900-1050 cm^{-1} are overlapped by the stretching vibrations of B-O bonds present in [BO_3] and [BO_4] units.[160,165] A band around 670-700 cm^{-1} is attributed to bending vibrations of Si-O-B bridging bonds which is present in synthesized glasses only.[165] The band around 760 cm^{-1} is assigned to the symmetric stretching vibrations of Si-O-Ca bonds illustrating the modifying nature of Ca ions.[163,164] The band close to 800 cm^{-1} is assigned to the symmetrical stretching of Si-O bond due to bridging oxygens[160] present in SiO_4 tetrahedral. The shift in the band at ~1430 cm^{-1} towards higher wavenumber with an increase in the ionic radii of the alkali ion indicates the strengthening of the O-B-O bond stretching vibrations due to the presence of bigger alkali ion. The presence of short-range ordered trigonal [BO_3] and tetrahedral [BO_4^-] borate groups along with tetrahedral silica[127] in the synthesized glasses is evident from the FTIR spectral analysis as compared to the tetrahedral vitreous structure of silicate units in the commercial SLG. The network modifier ions such as R^+/Ca^{2+} induce an effective positive charge field in the periphery of the bridging oxygen, resulting into the weakening of the Si-O-Si bond, and creating Si-O-Na/Li/K bonds. Thus, the synthesized glasses are expected to exhibit a more disordered structure and a variable amount of different structural units of silicates and borates leads to phase separated glass structure.[155].

In the present glasses, SiO_2 and B_2O_3 exist as network formers while CaO and R_2O as modifiers. While SiO_2 forms tetrahedral structural units of [SiO_4^{4-}], B_2O_3 exists as trigonal (BO_3^{3-}) and tetrahedral (BO_4^{5-}) units. The modifier units in the form of CaO are

expected to occupy the interstitial sites within the glass network creating NBOs. However, R^+ ions (R denotes the alkali ions) have the tendency to get attached with the B^{3+} ion to transform into tetrahedral BO_4^{5-} units. As the mol% of R_2O is greater than that of B_2O_3, R^+ ions partially occupy the interstices to create non-bridging oxygens (NBOs) in the network, and partially modify the borate network from $[BO_3^{3-}] \rightarrow [BO_4^{5-}]$ as proposed in **Fig. 4.6**.[8] Further modification in the glass structure is subjected to the ionic radii, cationic field strength **[Table 4.1]**[154], and mobility of the respective alkali ions.

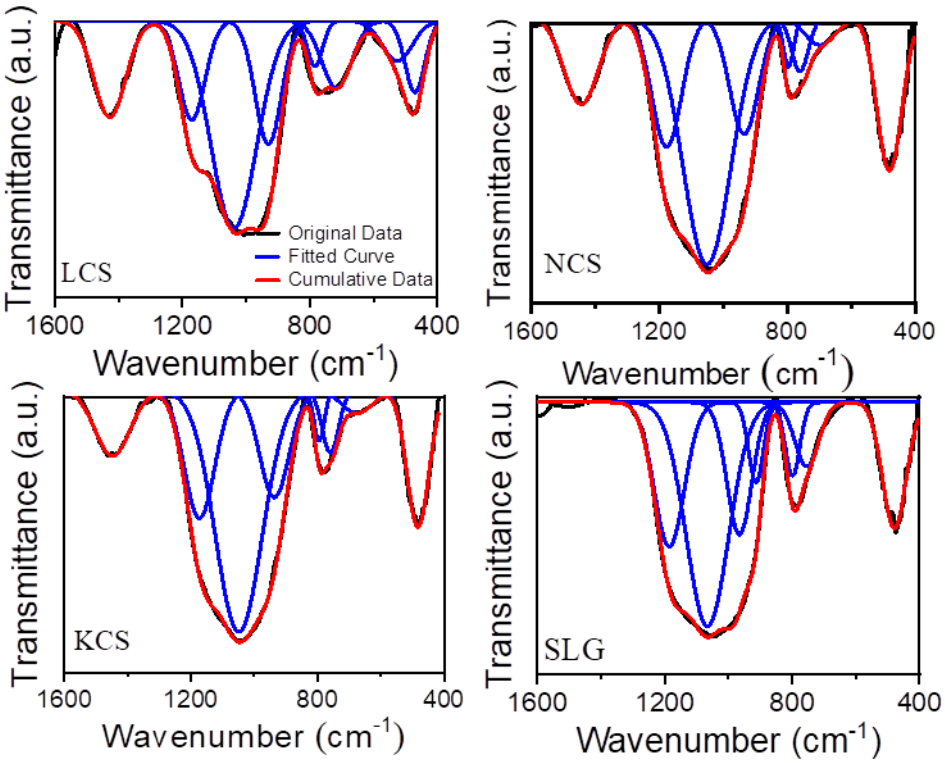

Figure 4.5: *Gaussian deconvolution of the FTIR spectra of different glasses.*

The R^+ ions break the Si-O-Si, Si-O-B, and B-O-B bridging bonds and create NBOs, which enhances disordering in the glass network. The diffusion of ions in disordered (modified) glass structure occurs by random jumps of ions from one position to another exchanging positions with their neighboring ions.[166] The alkali ion donates its electron to the NBO creating a cationic vacancy close to the NBO. Thus, the transport of alkali ion from one cationic site to another occurs under the influence of different

gradients such as temperature, electric field, and concentration. The proposed diffusion path of the alkali ions is illustrated in **Fig. 4.6**. The experimental evidence of the diffusivity of alkali ions is derived from the electrical properties of the glasses as described in **section 4.1.8.**

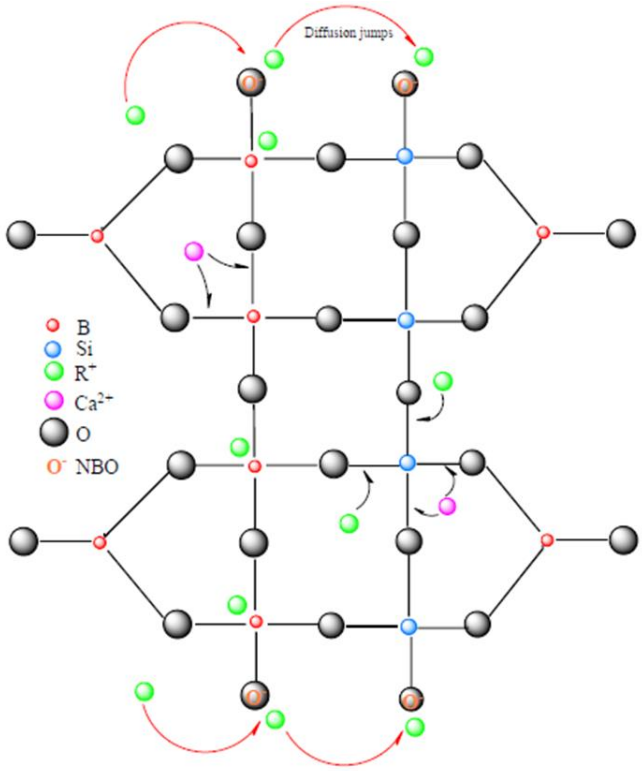

***Figure 4.6**: The proposed molecular structure of present glasses; Curved arrows in red represent the diffusion jumps of alkali ions from one site to another.*

As R_2O occupies the interstitial sites in the open network of tetrahedral silicate and borate units, the substitution of Li_2O by Na_2O and K_2O decreases the density **[Table 4.1]** of the glasses. The molar volume **[Fig. 4.1]** increases from Li incorporated glasses to the K incorporated ones. Li being smaller in size and with high cationic field strength results in the compactness of the volume occupied, with the lowest inter-ionic radii. The reduction in the size of the defect site tends to increase the density. The dependence of density on the cationic field strength of modifier ions has been previously reported by Kaur et. al.[8] K being a heavier ion, the density of the system should increase. However, in the present case, it decreases slightly. Moreover, the atomic

packing density is also found to decrease from LCS >NCS> KCS, as detailed in **section 4.1.5.** The slight lowering of density for KCS glass indicates that with the increase in mass, the free volume increases to a larger extent attributed to the low cationic field strength **[Table 4.1]** of K-ions. Thus, the impact of mass is less as compared to volume and field strength. The same is evident from the lowest packing density **[Table 4.2]** of KCS glass, compared to all other glasses.

4.1.4. XPS analysis

The influence of the presence of alkali oxide modifier on the nature of Si-O-Si bonds was investigated using XPS on powdered glass samples. **Figure 4.7 (a)** shows the typically indexed survey scans. The high-resolution XPS spectrum of Si2p [**Fig. 4.7 (b)**] shows the shifting of the peak to the lower binding energy for the LCS glass containing the smaller modifier ion (Li), revealing weaker bonds between Si-O.[167–169] It is in agreement with the results obtained from FTIR spectroscopy. Alkali ions (R^+) modify the silicate units ($Q^4 \rightarrow Q^3$), where Q^n is the tetrahedral structural unit with n = number of bridging oxygens (BOs))

$$\textbf{-Si-O-Si-}\ (Q^4) + \ \textbf{R}_2\textbf{O} \rightarrow \textbf{-Si-O-R}^+\ (Q^3) + \ \textbf{-Si-OR}^-\ (Q^3) \qquad \textbf{(4.4)}$$

Here, each alkali oxide breaks bonded Q^4 units to form two Q^3 units. While Q^4 units are covalently bonded to one another, the Q^3 unit is partially ionic (R-O) and partially covalent (Si-O). One can estimate that Na_2O and Li_2O are 42.74 and 43.62 % ionic, respectively whereas K_2O is 38.71 % ionic.[170] The highest ionic character and high field strength ($0.26/Å^2$) of Li tends to weaken the Si-O bonds, changing the local level symmetry in the silica tetrahedral. The stronger the bond between R-NBO, the weaker is the corresponding Si-O bond, as revealed by the shift of the Si 2p peaks.[169] A similar shift is also observed in the O 1s spectrum displaying symmetric peak of Si-O-Si bond linkages **[Fig. 4.7(c)]**. The lower binding energy for Si-O bonds in Li containing glass

(i.e., LCS) yielded the formation of stronger Li-NBO bonds, resulting in lower mobility and diffusivity of Li-ions. In comparison to SLG, the peaks corresponding to synthesized glasses are left shifted towards lower binding energy. This can also be attributed to the higher concentration of SiO_2 in SLG glass than synthesized glass (refer to experimental details). In the absence of borate units in the SLG glass, SiO_4^- forms a stronger tetrahedral network than in synthesized glasses.

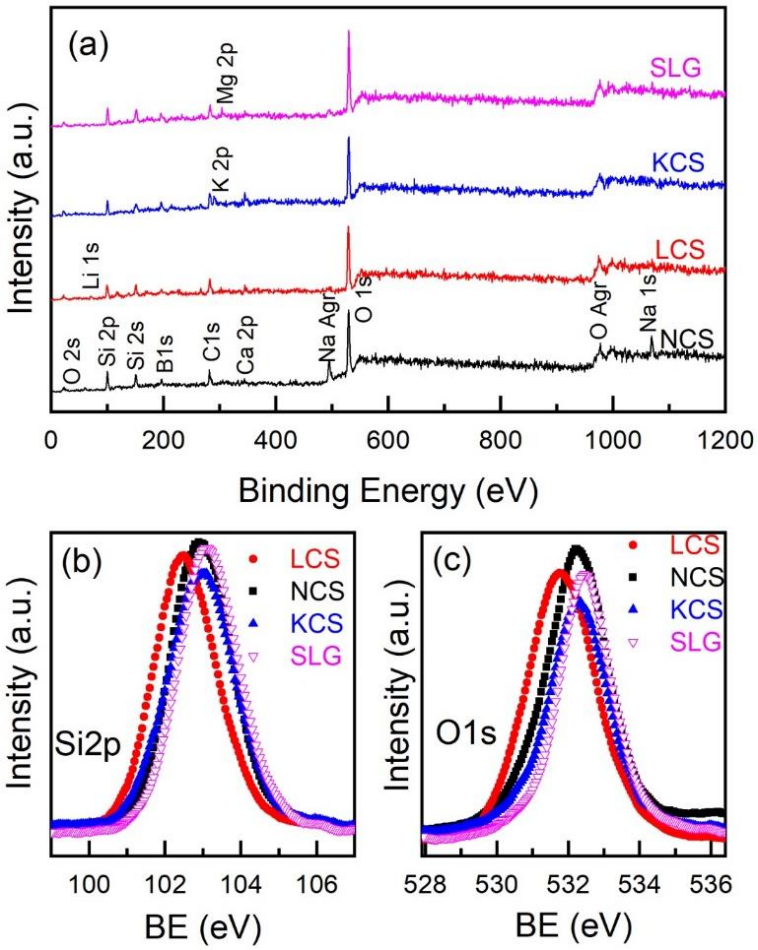

***Figure 4.7**: (a) XPS survey scan of respective glasses; High resolution scan of (b) Si2p and (c) O1s of the glasses.*

4.1.5. Mechanical properties

The variation in Vicker's microhardness with the field strength of the respective alkali ion (R) is depicted in **Fig. 4.8**. The highest hardness is observed for LCS glass i.e. 6.07 GPa. The hardness of the present glasses is higher than K_2O-Li_2O based glasses and

lower than the reported values for MgO-SiO_2-Al_2O-ZrO_2-Y_2O_3 glasses and glass-ceramics.[8,19,171] As shown in **Fig. 4.8**, the hardness varies with the type of the constituents in the initial composition. The presence of lithium oxide with stronger Li-O bonds (as deduced from XPS analysis) in the LCS sample strengthens the glass network. Therefore, the LCS glass yields maximum hardness as compared to other glasses. In contrast, the glass samples with Na_2O and K_2O exhibit the lower hardness values, due to weaker field strength associated with Na-O and K-O bonds, respectively. However, for the NCS glasses, the hardness was lower than that of K_2O containing glasses. This anomaly is associated with the mixed modifier effect attributed to the presence of CaO along with alkali oxides in the glass composition.[15,172][172] It is discussed in detail in **section 4.1.8**.

The packing density of glasses was calculated using the following formula based on the Makishima-Mackenzie model

$$\boldsymbol{V_t = \frac{1}{V_m}\sum_i (x_i V_i)} \quad \textbf{(4.5)}$$

where, x_i is the mole fraction of constituent oxides and V_i is the packing factor of the respective oxides.[173–175] Further, the packing density is used to estimate the Poisson's ratio (γ) for the glasses using the equation given below

$$\boldsymbol{\gamma = 0.5 - \frac{1}{7.2 V_t}} \quad \textbf{(4.6)}$$

The calculated results are given in **Table 4.2**. As the size of the alkali modifier ion increases, V_t of the glasses decreases, which agrees with the experimentally observed density. More loosely are the ions are packed, smaller is the Poisson's ratio.

The elastic modulus (E) is calculated using

$$\boldsymbol{E = 2V_t \sum_i (x_i G_i)} \quad \textbf{(4.7)}$$

where, G_i is dissociation energy per unit volume for the glass component.[174]

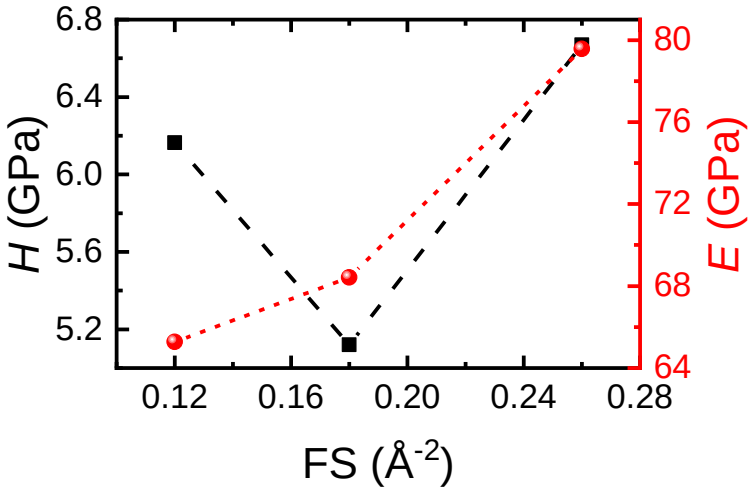

***Figure 4.8**: Field strength dependence of hardness and elastic modulus.*

***Table 4.2**: Packing density (V_t), Poisson's ratio (γ), elastic modulus (E), micro-hardness (H), fracture toughness (K) of the present glasses.*

Sample ID	**V_t ±0.001**	**γ ±0.001**	**E/GPa ±0.001**	**H/GPa ±0.001**	**K/MPa $m^{1/2}$ ±0.001**
LCS	0.589	0.264	79.571	6.669	--
NCS	0.560	0.251	68.416	5.120	0.863
KCS	0.553	0.248	65.270	6.164	0.894
SLG	0.555	0.249	67.877	5.630	0.733

Using the microhardness and the elastic modulus calculated above, the fracture toughness is obtained for different glass samples.[8] As expected, the highly packed structure of LCS has the highest elastic modulus and microhardness as compared to NCS and KCS glass samples, as shown in **Table 4.2**. However, the NCS glass has a lower microhardness, but higher elastic modulus than the SLG, which demonstrates the higher packing density of the NCS glass than that of the SLG. The higher the connectivity within the glass network more is the tendency of ion mobility. Moreover, the Poisson's ratio lying in the range of 0.248-0.264 **[Table 4.2]**, indicates good mechanical stability of the present glasses. The fracture toughness (K) of the NCS glass (0.863 MPa $m^{1/2}$) is also

higher than SLG (0.733 MPa $m^{1/2}$), which is highly desirable for use as a substrate in the solar cells.

4.1.6. Thermal properties

4.1.6.1. Differential thermal analysis

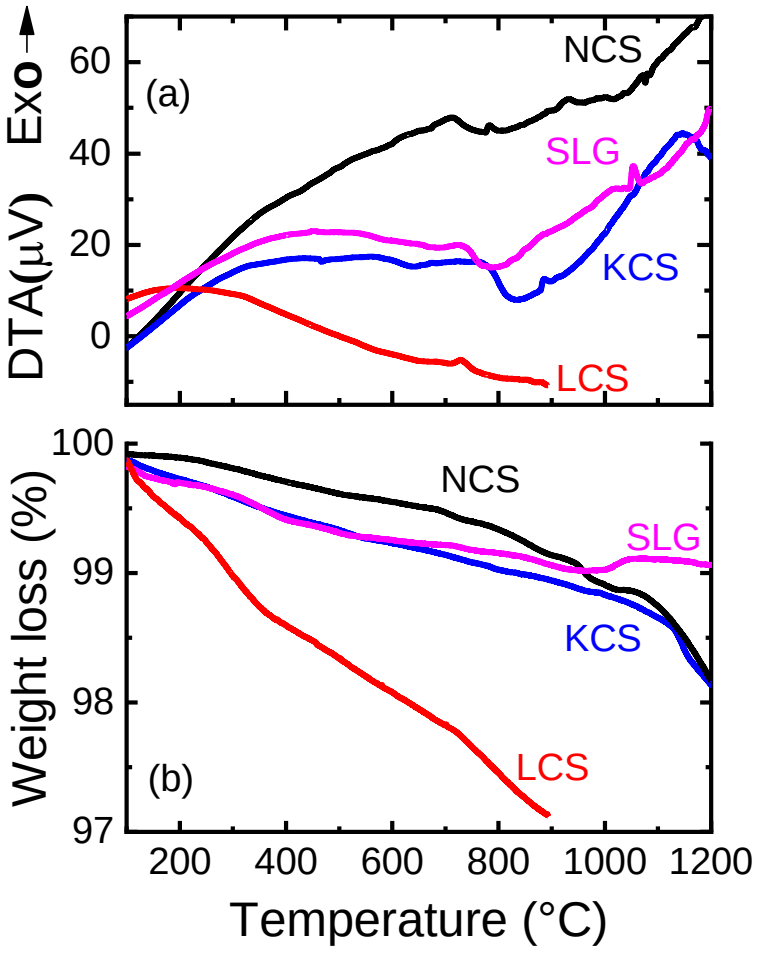

Figure 4.9: *(a) DTA (exo up) and (b) TGA curve for different glass samples.*

The DTA and TGA plots for the LCS, NCS, KCS, and SLG glass samples were obtained at a heating rate of 10°C/min and are depicted in **Fig. 4.9 (a-b).** The DTA curve for all the glass samples exhibited the glass transition temperature (T_g) in the range of 500-600 °C, similar to the previous studies.[131,134,138] The exothermic peaks above 700 °C correspond to the phase transformation or crystallization temperatures (T_c) followed by melting point beyond 1100 °C **[Fig. 4.9(a)]**. The estimated T_g and T_c for all the glass samples are given in **Table 4.3.** It is interesting to note that T_g for the NCS and KCS

glasses is higher than the commercial SLG, which was desired in the present study. However, the LCS glass exhibited the minimum T_g, which is attributed to the thermally activated volatility (or mobility) of lighter Li-ions as compared to Na and K. It also resulted in the highest weight loss ~2.5%, up to 800 °C temperature compared to 0.5%, 0.9% and 0.75% for the NCS, KCS and SLG glass samples, respectively. This suggests better thermal stability with very low weight loss for the NCS, KCS, and SLG glass samples than the LCS glasses. The thermal behavior of the NCS and SLG glasses is compared from the representative combined plot of DTA and TGA shown in **Fig. 4.10 (a-b),** respectively**.** The NCS glass exhibited a peak corresponding to one T_g, followed by three exothermic peaks of T_c (T_{c1}, $T_{c2,}$ and T_{c3}) and one endothermic peak of T_m **[Fig. 4.10 (a)]**. On the other hand, SLG depicted one T_g, two T_c (T_{c1} and T_{c2}), and one T_m. Typical weight loss and gain cycles are observed in all the samples corresponding to characteristic exothermic and endothermic peaks in DTA. Vertical gridlines passing through the characteristic temperature peaks divide the TGA curve into separate areas representing the variation in slope at characteristic temperature, which is an indirect manifestation of differential thermogravimetric analysis. Although the weight loss in present glasses is very small (0.5-3%), this loss may be attributed to the mobile nature of alkali ions, which show fast diffusion from one interstitial site to another within the glass matrix. A sharp slope of weight loss appears up to the T_g, followed by a decrease in slope close to T_c peaks and a steep slope of weight loss beyond the melting temperature. This trend is similar to the cooling curve of alloys exhibiting phase transition temperatures.

The exothermic peak maximum corresponds to the maximum rate of transformation of glass to the crystalline phase. Since the present glass composition consists of two formers and two modifiers, phase separation occurs due to the formation of a localized glass matrix within the glass matrix corresponding to alkali and Ca modified silicate and borate

units, as discussed in XRD and FTIR analysis above.[140] Similar phase separation has been observed in soda lime aluminosilicate glasses in previous studies.[176] The increased T_g for the present compositions is attributed to the higher content of Ca, as compared to that in SLG. It is in agreement with the previous studies[5,177] that a higher concentration of Ca containing glasses have higher T_g. Moreover, the role of Ca is evident from the formation of the Wollastonite phase ($CaSiO_3$) as shown from the XRD analysis. It is also noteworthy that no significant crystallization was observed in NCS glass until heat treated at 935°C. Thus, as the T_g increases, the crystallization temperature is also increased.

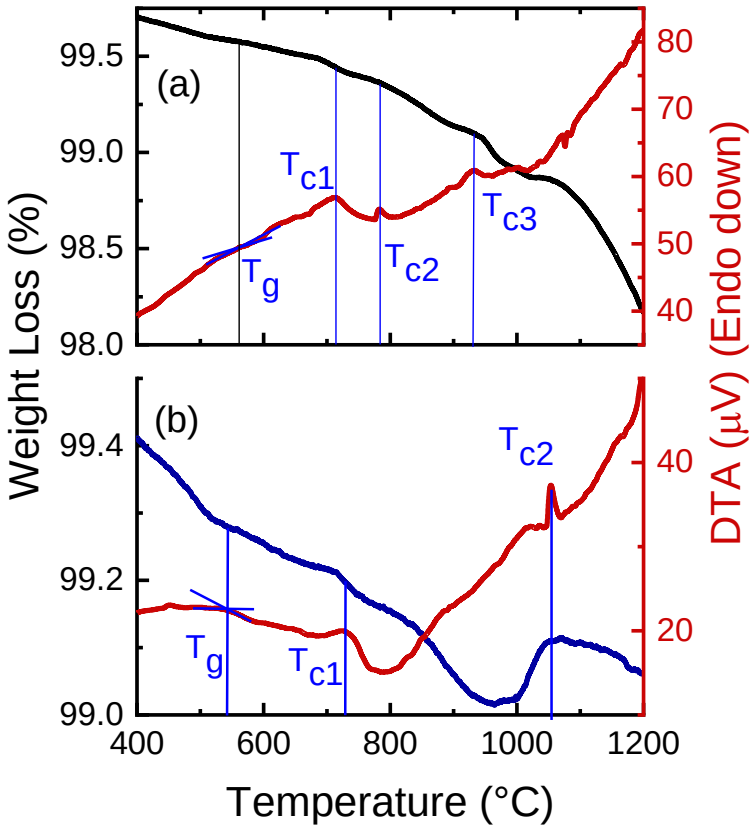

Figure 4.10: *TGA (left) and DTA (right) combined plot of (a) NCS; and (b) SLG glasses, respectively.*

***Table 4.3**: Glass transition temperature (T_g) and phase transition temperature (T_c) for different alkali oxide containing glasses.*

Sample ID	T_g /°C	T_c /°C
LCS	533	685, 730
NCS	563	712, 782, 935
KCS	574	672, 884
SLG	542	735, 1054

4.1.6.2. Thermal dilatometric analysis

Figure 4.11 represents the thermal dilatometric analysis of the present glasses performed at the heating rate of 5°C/min in air. A linear behavior from 100-500 °C demonstrated no phase transformation for the LCS, NCS, and KCS glass samples. However, a change in slope between 500-600 °C was observed that suggests a glass transformation region as also manifested in DTA. The corresponding transformation region is highlighted in the inset of **Fig. 4.11 (right)**. The dilatometric softening point (T_d) is identified at the peak maximum. On the other hand, the dilatometric glass transition (T_{gd}) was obtained at the point of inflection of the softening region. T_d and T_{gd} were found to increase from LCS to NCS to KCS.

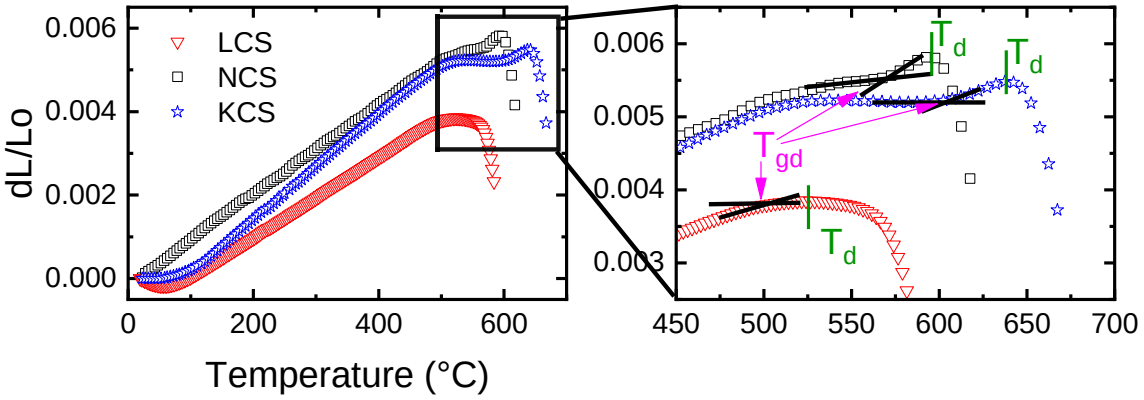

***Figure 4.11**: Thermal dilatometric plot of LCS, NCS, and KCS glasses showing T_{gd} and T_d.*

The coefficient of thermal expansion (TEC) was calculated as the slope of the linear region from 200-500°C. The variation in the TEC and T_d of the samples is depicted

as a function of the packing density of glasses in **Fig. 4.12 (a)**. As the packing density for the LCS glass is higher [**Table 4.2**], the atoms are more closely attached in the glass network, such that dilation occurs earlier than that in the NCS and KCS glasses, both having .lower packing density than LCS. Therefore, the softening temperature is lower for LCS glass, which is in agreement with the thermal behavior depicted from DTA. Moreover, the LCS glass did not exhibit the phase transition region in the range of 525-550°C in **Fig. 4.11** whereas NCS and KCS glasses exhibited two to three-phase transformation or crystallization peaks (in DTA). Thus, the phase separation is more prominent in the NCS and KCS glasses as compared to the LCS glass. On the other hand, the trend in TEC of glasses was not linear **[Fig. 4.12 (a)].** The NCS glass exhibited a TEC lower than that for both LCS and KCS glasses. This can be correlated to the lower value of the hardness of NCS glass discussed earlier. **Figure 4.12 (b)** presents the variation in T_g obtained from DTA and T_{gd} obtained from the Dilation curve. T_g and T_{gd} values are in close agreement with each other. Although both represent the glass transition temperature, the variation in values is possibly due to the difference in the method of measurement and the heating rate. The dilation measurement was carried out at a lower heating rate. A slower heating rate leads to earlier nucleation in glasses, as the glass transformation process is a time dependent phenomenon. The rate of heating or cooling largely affects the thermal characteristics of the glass materials.

Nevertheless, the glass transition and softening temperature of the present glasses lie well above the processing temperature of CIGS/CZTS thin films[24]. The coefficient of thermal expansion for LCS, NCS, and KCS glass is close to that of SLG (9×10^{-6} /°C).[24] Based on thermal stability, T_g, $T_{d,}$ and TEC, the present glasses could be considered suitable for use as a substrate for thin film solar cells.

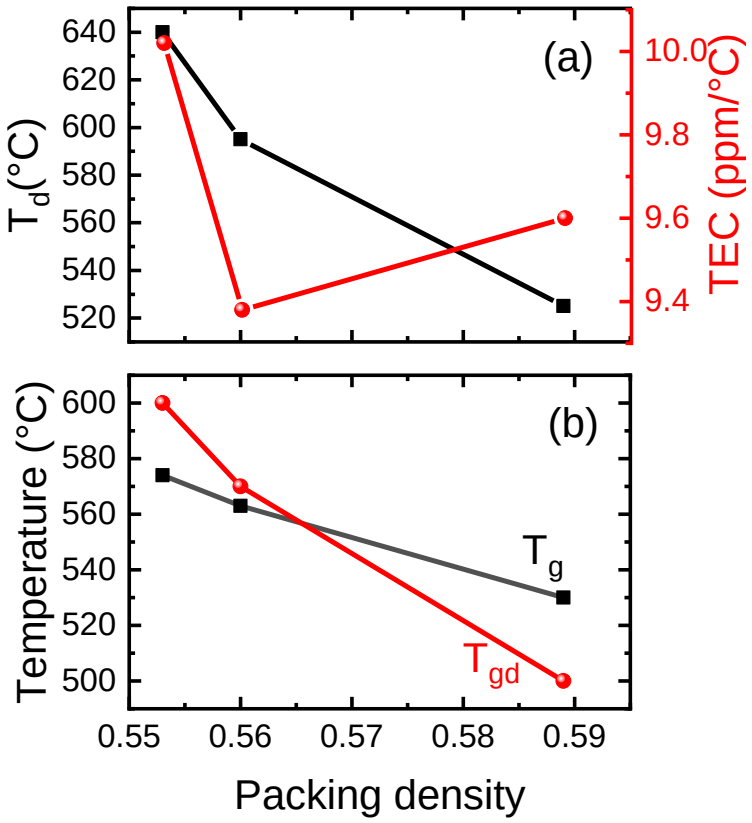

***Figure 4.12**: (a) Dilatometric softening temperature (T_d), coefficient of thermal expansion (TEC); (b) Glass transition temperature obtained from DTA and TDA for respective glasses with respect to the atomic packing density of glasses.*

4.1.7. Optical properties

Figure 4.13 shows the UV-Visible transmittance of the synthesized glasses. Irrespective of the composition, all glasses showed transmittance better than 80 % at λ ~ 400 nm. Transmittance edge was observed in the wavelength range of 280-360 nm for the present glasses. The band edge shows a redshift in wavelength with the decreasing size of alkali ions, as shown in the inset of **Fig. 4.13 (a)**. The Beer-Lambert's relation (Eq. **3.4**) was used to calculate the absorption coefficient from transmittance with the change in wavelength.

The direct optical bandgap was estimated from the linear extrapolation of the Tauc plot of $(\alpha h\nu)^2$ versus photon energy hν as depicted in **Fig. 4.13 (b)**.[8,178] The bandgap was found to be 3.77 eV for KCS, 3.86 eV for LCS, and 3.99 eV for SLG, and 4.02 eV for the

NCS glass sample. The Urbach energy (E_u) that quantizes the degree of disorder in the glass structure was calculated from the slope of the linear region in the plot of ln(α) versus hν.[10] The trend of E_u for different glass samples is represented in **Fig. 4.13 (c).** It is found that with the increase in the ionic radii, E_u increases (ionic radii for Li^+, Na^+, and K^+ ions in octahedral coordination are 0.76, 1.02, and 1.38 Å, respectively).

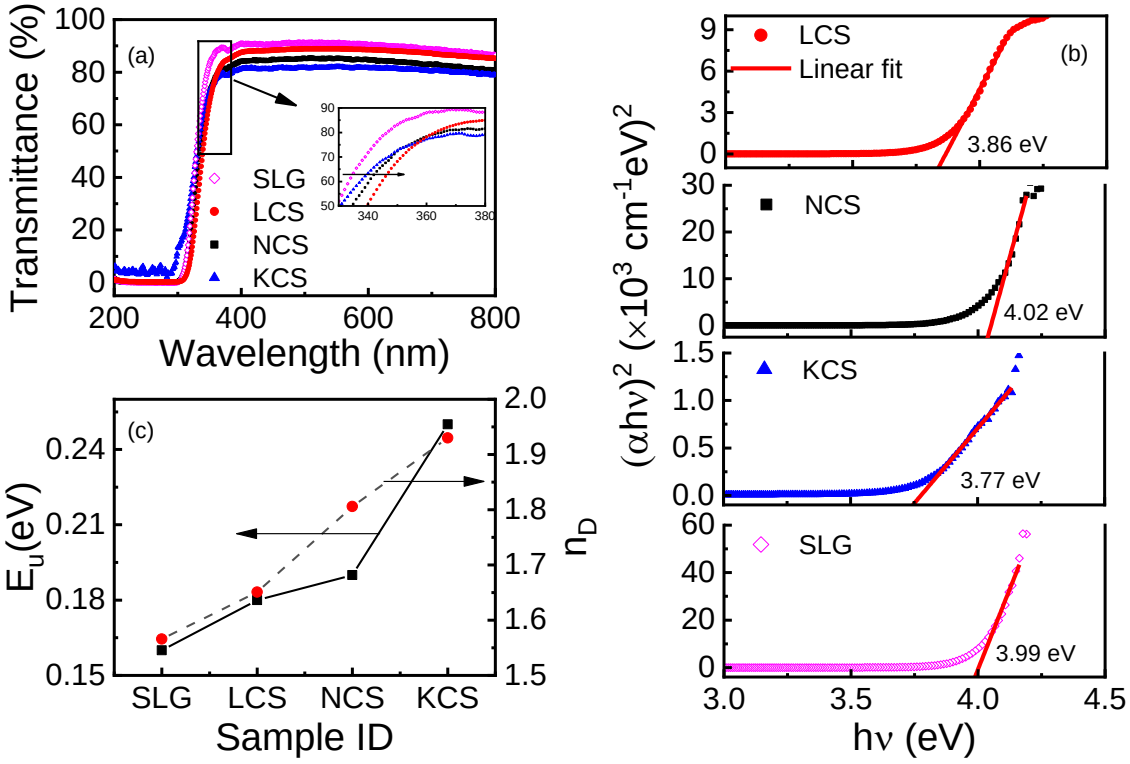

***Figure 4.13**: (a) Transmittance (%) of all glasses; (b) Tauc's Plot of $(\alpha h\nu)^2$ versus photon energy hv. The solid lines indicate liner fit to data to estimate the bandgap; (c) composition dependence of Urbach energy (E_u) and refractive index (n_D) of the glass samples.*

The variation in the refractive index of the glasses with wavelength was studied from the transmittance spectra and is given in **Fig. 4.14**.[8] The refractive index for the respective glasses at sodium D-line wavelength 589.3 nm is represented in **Fig. 4.13 (c)**. **Table 4.4** lists the refractive index, optical basicity, and oxide ion polarizability of the glass samples, which was calculated as detailed by Kaur *et al.*[10] The Urbach energy,

refractive index, optical basicity, and ionic polarizability, all show an increasing trend with the increase in the size of alkali in respective glass samples.

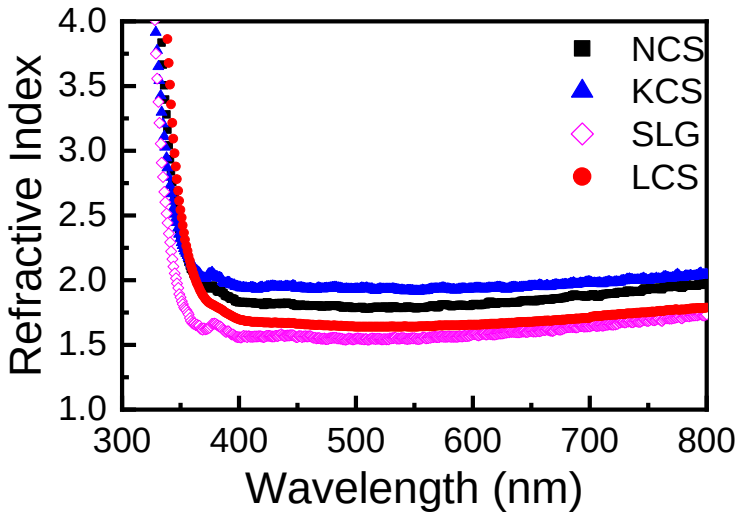

***Figure 4.14**: Refractive index with respect to wavelength for different glass samples.*

The bandgap of the present glasses corresponding to the direct transitions does not follow a trend with the size of the alkali ion, however, it can be correlated to the number of NBOs in the glass structure. The lowest bandgap and highest Urbach energy of KCS glass are attributed to the higher density of defect states, which are created due to a higher number of NBOs in the glass network exhibiting an increase in disorder in the structure[34]. A higher bandgap follows a decrease in Urbach energy for all the glass samples. However, an anomalous increase in the bandgap of NCS glass is correlated to the Na-Ca co-existence which is discussed in detail at a later stage. The increase in refractive index and ionic polarizability from LCS<NCS<KCS is attributed to higher electron density in the glasses with a higher atomic number of alkali ions. Comparing NCS with commercial SLG, n_D for SLG is 1.56 whereas that for NCS is 1.80. As the ionic polarizability **[Table 4.4]** is higher for NCS than SLG, the refractive index is also increased.

The typical device structure of CZTS is shown in **chapter 1.** Since, light is incident from the top surface,[179] the optical properties of the glass substrate do not affect

critically the device performance in this configuration. It is consistent with the other reports wherein various metallic, ceramic, or polymer based substrates have been employed for CZTS solar cells, irrespective of the optical properties of the substrate material [51,63,99,180]

***Table 4.4**: Optical basicity (□), ionic polarizability (α_o), and refractive index (n_D) of the glass samples.*

Sample ID	□	α_o **±0.001**	n_D
LCS	0.564	1.185	1.65
NCS	0.577	1.197	1.80
KCS	0.596	1.215	1.93
SLG	0.565	1.186	1.56

4.1.8. Electrical analysis

While the physical, mechanical, optical, and thermal properties are found to satisfy the suitability of the synthesized glasses as a substrate in thin film solar cells, the most desired characteristic, i.e. diffusivity of alkali ions is estimated from the dielectric and conductivity analysis of the present glasses**. Figure 4.15 (a) and (b)** show the variation in the dielectric constant ε′ at room temperature (RT) and 500 °C, respectively in the frequency range from 1 kHz to 1 MHz. At RT, the dielectric constant decreased marginally in the frequency range 10^2 to 10^3 Hz and remained constant thereafter. The highest value of ε′ (~40) was obtained for the NCS glass while the lowest was obtained for the SLG glass (~10). It might be associated with the presence of two glass network formers ($[SiO_4^{2-}]$ and $[BO_4^-]$) in the NCS, KCS, and LCS in comparison to SLG in which only one glass former is present. The tetrahedral borate units are known to enhance the polarizability of the glasses.[146,149] Thus, two glass network former containing glasses have a more asymmetric glass network leading to a higher possibility for polarization.

The obtained higher value for the NCS glass is attributed to the higher polarizability of Na-ions. On the other hand, as the molar volume of LCS glass is lower, ions are more strongly bound to the network, and hence exhibit lower polarization.

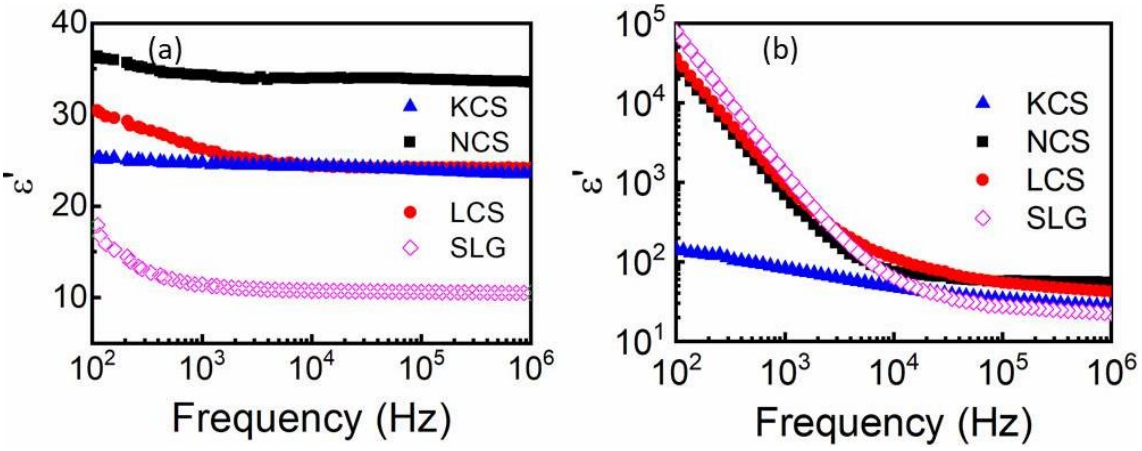

***Figure 4.15**: Dielectric constant (ε') variation with respect to the frequency at (a) RT and (b) 500°C for the glasses.*

However, as the temperature increases, the lithium ions being smaller in size, gain enough energy to actively participate in the polarization phenomenon whereas KCS glass exhibits anomalous behavior. It has the highest refractive index and polarizability but shows a lower dielectric constant. This is probably because K-ions with bigger sizes are less mobile, resulting in a lower dielectric constant of this particular glass than other glasses. At RT, the dielectric constant includes a contribution from the ionic polarization, attributed to the modifier ions creating dipoles with NBOs. In the present glasses, positively charged alkali ions (Li^+, Na^+, K^+) create dipoles with O^{2-} NBOs, which are bound to the tetrahedral network of Si^{4+}. As the temperature increases [**Fig. 4.15 (b**)], the ions creating dipoles under the influence of bias voltage get thermally activated to align towards the interfaces, thus enhancing the charge accumulation at the interfaces between glass/electrode (negative charge due to NBOs and positive charge due to R^+ and Ca^{2+}, which attributes to the space charge polarization.[181,182]

Figure 4.16 (a-b) shows the tangent of loss of the glasses at RT and 500 °C, respectively. At RT, it was found to be less than unity, for all the glasses. As the temperature

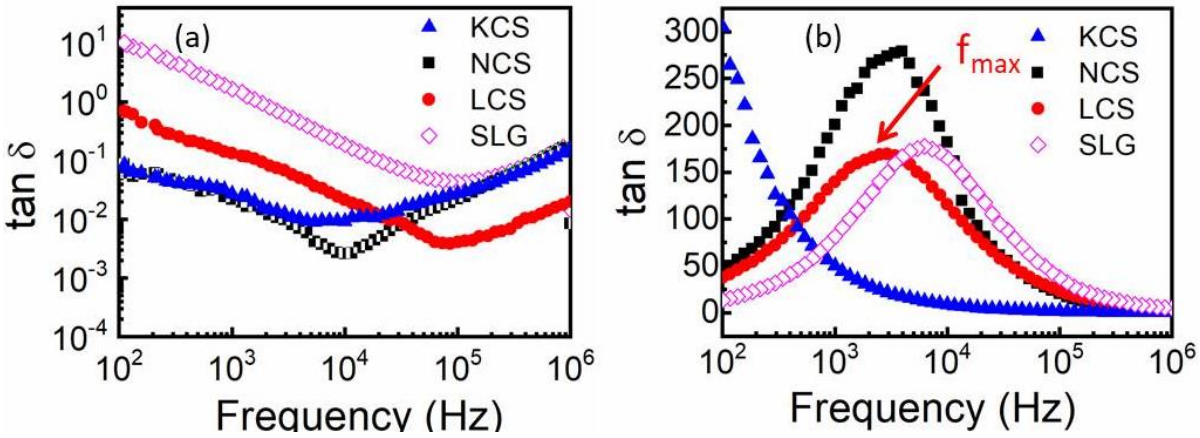

Figure 4.16: *Tangent of losses (tan δ) with frequency at (a) RT, and (b) 500°C, for all the glasses.*

increases (at 500°C) **[Fig. 4.16 (b)]**, the tangent of loss exhibit a peak (f_{max}) for all the glasses, except KCS, owing to the Debye relaxation phenomenon.[183,184] The relaxation time ($\tau = 1/f_{max}$) was calculated from the inverse of peak frequency (f_{max}).[185] The relaxation time (τ) given in **table 4.5** is lower for Na ions in NCS glass than Li ions in LCS glass. Relaxation time has a direct correlation with the diffusion time of the ions, which act as the charge carrying species in the glasses. Thus, Na ions exhibit higher diffusivity in NCS glass. This behavior is the representation of ionic conductors.[186–188] The alkali ions ($Na^+/Li^+/ K^+$ ions present in oxide glasses) with an inherent character of high mobility tend to the conduction losses in the dielectric materials. Interestingly, NCS glass has the highest dielectric constant with the lowest losses, while SLG has the least ε′, with the highest losses at RT. In all the glasses, NCS glass exhibiting characteristics of a good dielectric materials property proves to be suitable as a choice for the substrate. **Figure 4.17 (a-b)** depicts the temperature dependence of dielectric constant and tangent of losses, respectively, for all the glasses. The sharp increase in dielectric constant, on one

side, and tangent of losses, on the other side, at higher temperatures is attributed to the thermal activation of the charge carrier ions. The peak in **Fig. 4.17 (b)** corresponds to the thermal relaxation temperature of the ions, beyond which the losses sharply decrease. Thermal relaxation for Na ions in NCS and SLG occurs at the lower temperature followed by Li, and at a very high temperature for K ions.

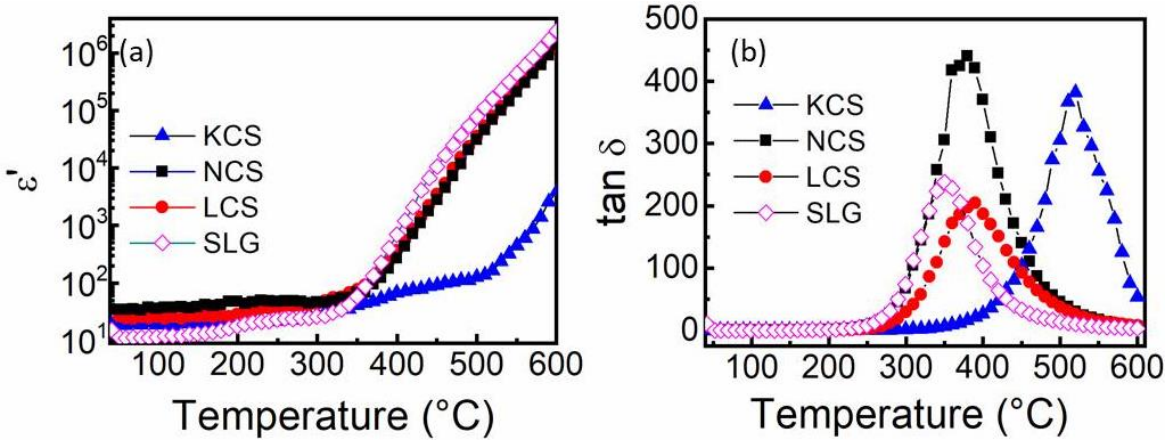

***Figure 4.17**: Temperature dependence of (a) dielectric constant, and (b) tangent of losses variation in low-frequency regime (100 Hz) for the present glasses.*

To study the conduction phenomenon, the ac conductivity was obtained from the ac loss, given by the following relation:

$$\boldsymbol{\sigma_{ac} = \epsilon_o \omega \epsilon''} \qquad \textbf{(4.8)}$$

where, ε_o is relative permittivity, ε'' is imaginary permittivity at angular frequency 'ω'. The ac conductivity (σ_{ac}) curve versus frequency (f = ω/2π) was fitted with the Jonscher's power law[185,189], given by equation below:

$$\boldsymbol{\sigma_{ac} = \sigma_{dc} + A\omega^s} \qquad \textbf{(4.9)}$$

where, σ_{dc} is the frequency limiting conductivity or dc conductivity, 'A' is a pre-exponential constant depending on the number of free mobile charge carriers, and 's' is the power of the frequency defining the power law. Thus, the curve can be divided into two components, frequency independent and frequency dependent, where frequency independence contributes to the dc conductivity.

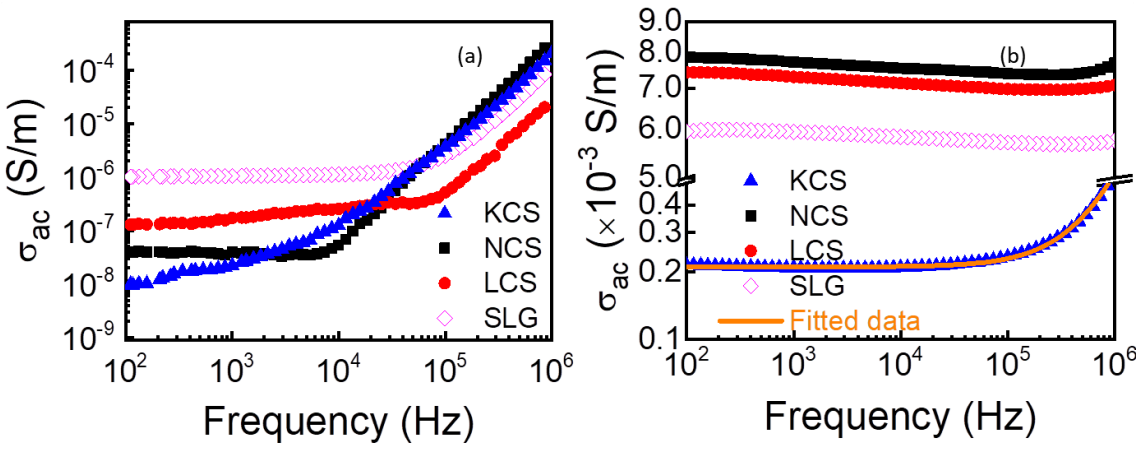

Figure 4.18: *ac conductivity dependence on the frequency at (a) RT, and (b) 500°C for the present glasses.*

Conductivity in **Fig. 4.18 (a)** for the glasses at RT exhibits two regions. The low frequency plateau exhibits the dc conductivity of the ionic conductors, while the high frequency logarithmic increase in conductivity beyond a crossover frequency corresponds to the superlinear power law dependence of conductivity.[10,190] As shown in **Fig. 4.18 (b)**, with the increase in temperature up to 500°C, the ac conductivity plot exhibits frequency independence of conductivity for NCS and LCS glasses along with the SLG. The conductivity plot (σ_{ac}) with respect to frequency is fitted with Jonscher's power law to obtain the dc-conductivity (σ_{dc}) from the plateau region, as represented in **Fig. 4.18 (b)**. Corresponding values of σ_{dc} (at 500°C), for all the glasses, are given in **Table 4.5.** The frequency-independent conductivity is attributed to thermally activated ions of the glasses, with complete contribution from the ionic conductivity excluding the charge accumulation contribution. The conductivity in these glasses is significantly ascribed to the alkali-ion migration and diffusion within the glasses.[177,191] At RT, the conductivity of SLG glass is higher than synthesized LCS, NCS, and KCS glasses. Here, the conductivity of glasses is dominated by not only the transport of alkali ions within the bulk glass network, but also the surface conduction of adsorbed water molecules.[26] In the case of synthesized glasses (LCS, NCS, and KCS), B_2O_3 intermittent within the silicate network

appears to enhance the compactness in the glass structure, restricting the movement of modifier ions.[146] This reduces the conductivity of alkali ions in synthesized glasses compared to commercial SLG. In higher temperature region, with the increase in temperature, the charge carrier dynamics within the structure due to thermal activation creates a path for the hopping of ions through the interstitial sites, owing to a higher disordered network. This results in a higher conductivity of LCS, as well as NCS, synthesized glasses than SLG. However, the anomalous behaviour of KCS with higher thermal relaxation temperature leads to the lowest conductivity. To understand the thermal activation phenomenon of the alkali ions, Arrhenius plot of dc conductivity with ln σ_{dc} vs. 1000/T is represented in **Fig. 4.19**.

$$\boldsymbol{\sigma_{dc} = \sigma_o exp(^{-E_a}/_{k_B T})} \qquad \textbf{(4.10)}$$

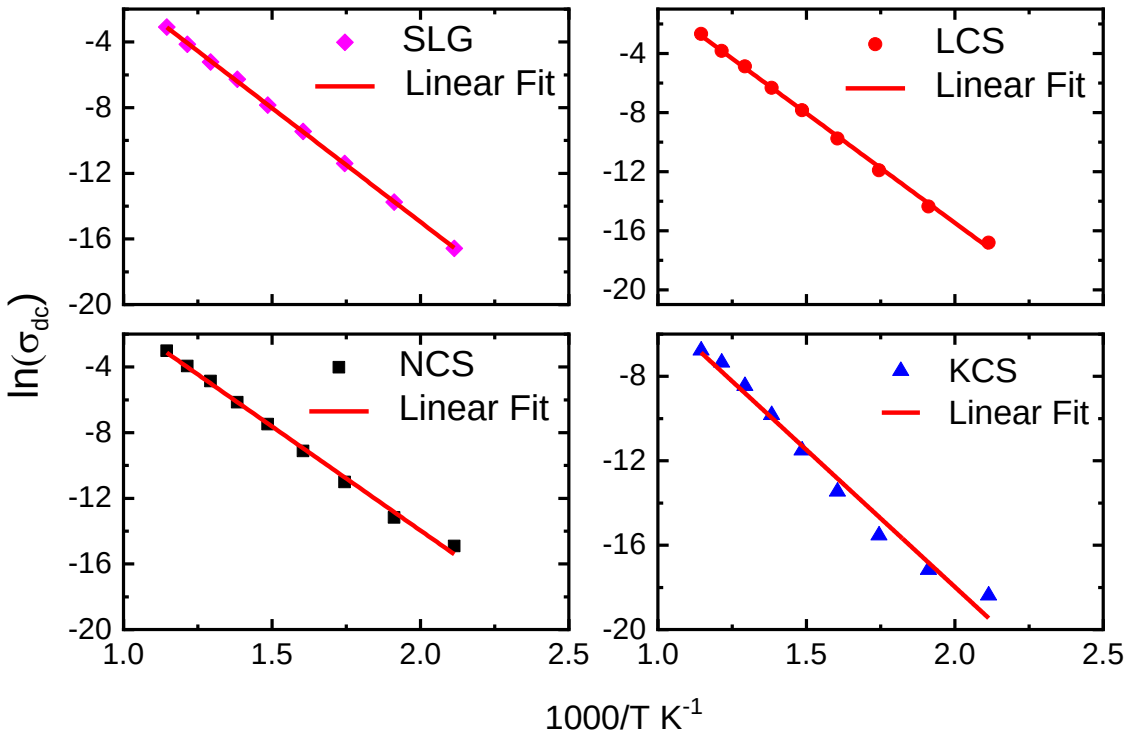

***Figure 4.19**: Arrhenius plot of dc conductivity for all the glass samples.*

The linear region is observed at a high temperature which corresponds to the conduction mechanism of thermally activated ions. The slope of the linear fit region is

used to calculate the thermal activation energy in the high temperature region[10] as given in **Table 4.5**. It is well known that the activation energy in the range of 0.9-1.5 eV is assigned to the ionic conductivity phenomenon.[5,42,192] The thermal activation energy corresponds to the alkali ion activation, which is lowest for Na ions in NCS glass. The least conductivity of KCS glass is evident from the highest E_a for K ions. This activation energy is responsible for providing a conduction path for the hopping of alkali ions ($Li^+/Na^+/K^+$) loosely attached to the NBOs. Thus, ionic conductivity is correlated to the mobility and diffusivity of the ions from one site to another within the material.[166,183,191]

In the case of silicate glasses containing alkali and alkaline earth ions as modifiers, it is well known that the conduction phenomenon is dominated by the mobility and diffusivity of alkali ions, rather than alkaline earth ions attributed to their smaller cationic size and lower charge than alkaline earth ions. The extent of diffusion/mobility of alkaline earth ions is negligible compared to the alkali ions.[177,191,193] However, in the case of NCS glass, the size difference between both the modifier ions are comparable i.e. Na^+ (0.94) and Ca^{2+} (0.98) may also affect the lower activation energy and hence higher mobility and diffusivity of Na ions in NCS glass than other two glasses. The mobility of ions was calculated using

$$\boldsymbol{\mu = \frac{\sigma_{dc}}{Ne}} \qquad \textbf{(4.11)}$$

The diffusion coefficient of the ions was calculated using the Nernst-Planck equation:

$$\boldsymbol{D = \frac{\sigma_{dc} kT}{Ne^2}} \qquad \textbf{(4.12)}$$

where, σ_{dc} is the dc conductivity, k is the Boltzmann constant, T, the temperature (in Kelvin), N is the ionic concentration of alkali ions and e is the elementary charge of the ion.[194] The diffusion coefficient for the alkali ions in respective glasses was calculated at 500°C. The variation in dc conductivity, diffusivity, mobility, and activation energy for

different glasses is represented in **Table 4.5**. It demonstrates that these parameters do not follow a fixed trend with the change in the ionic size of the alkali ion contained in the glasses.

***Table 4.5**: Activation energy (E_a), relaxation time (τ), (dc-conductivity (σ_{dc}), diffusivity (D), and mobility (μ) of the alkali ions present in the respective glasses.*

Sample ID	**E_a/eV ±0.01**	**τ/s (×10^{-4})±0.1**	**σ_{dc}/Scm^{-1} (×10^{-5})±0.01**	**D/cm^2 s^{-1} (×10^{-11})±0.01**	**μ/cm^2 $(Vs)^{-1}$ (×10^{-9})±0.01**
		500°C			
LCS	1.27	3.5	7.55	7.53	1.12
NCS	1.09	2.8	7.72	8.40	1.26
KCS	1.42	--	0.143	0.17	0.02
SLG	1.19	1.5	5.39	2.35	0.87

The lowest mobility of K ions in KCS glass is primarily attributed to the bigger ionic radii that inhibit the hopping of heavier ions through comparatively smaller interstitial sites. The mobility of Na-ions in NCS glass is highest followed by Li-ions, while that for Na ions in SLG is lower, directly correlating with the conductivity behavior discussed above. The lower mobility of Li ions than Na ions, despite having a smaller size, is affected by the higher field strength of Li ions, which enhances the coulombic interaction with the NBOs. This is also evident from the highest density of LCS glass among the present glasses. Since the diffusion process is a function of mobility and ionic concentration,[177] both are higher for Na-ions in NCS glass, resulting in the highest diffusion coefficient, which is highly recommended for alkali ion incorporation from the substrate to the overlayers. Although the Li ion concentration is higher, lower mobility due to higher field strength results in lower diffusivity.

To summarise here, NCS glass has higher elastic modulus, microhardness, and fracture toughness with a highly packed glass structure, as compared to SLG. The presence of trigonal and tetrahedral borate and different silicate structural units in synthesized glasses exhibited a more disordered structure as compared to commercial SLG, consisting of silicate structural units only. Higher refractive index and ionic polarizability of NCS glass lead to higher dielectric constant with lower losses. The highest conductivity of NCS glass at 500°C (which is the processing temperature for thin film solar cells) with the lowest thermal activation energy leads to the highest mobility and diffusion coefficient, which can be used as a substrate for thin film solar cell. It is also concluded that both Li ion (in LCS glass) and Na ion (in NCS glass) diffusion takes place to a significant extent, but K ions have very low diffusivity, which shows that while KCS glass is not suitable as substrate, but NCS and LCS glasses can surely be recommended for application as substrate material as per the structural, mechanical and thermal properties along with the higher tendency of alkali-incorporation from the substrate to overlayers in a thin film solar cell.

Till here, we discussed the effect of nature/type of alkali oxide contained in glasses on its properties. Further, we have presented the effect of mixing two alkali ions in systematic proportions on structural, mechanical, physical, optical, thermal, and electrical properties of the synthesized glasses in light of their applicability as a substrate material for thin film solar cell.

4.2. Mixed alkali effect

The structure-property correlation of a single type of alkali oxide containing glasses revealed an anomalous behavior for NCS glass with the highest diffusivity and lowest activation energy, highly suitable for substrate application. Further, selecting the NCS glass composition as the base, Na_2O is systematically replaced by Li_2O and K_2O,

respectively, by step of 5, 10, and 15 mol%, in order to investigate the influence of mixed alkali effect on the properties of glasses. The mixed alkali effect refers to the non-linearity in the properties of glasses, which occurs due to the substitution of one type of alkali ion by the other alkali ion at a fixed proportion.[123,195,196] This non-linearity is generally observed in the transport properties of the mixed-alkali oxide containing glasses, attributed to the variation in ionic mobility of different alkali ions. Basically, the local environment in the silicate glasses containing mixed R-O polyhedra disturbs the ion-migration. Conduction and diffusion of alkali ions in present glasses are expected to be strongly influenced by the mixed-alkali effect; thus forms an important part of the present study. The characteristic thermal, mechanical, physical, optical, and electrical properties of the current glass compositions were determined by similar methods and techniques as mentioned in **section 4.1**.

4.2.1. Physical, mechanical, and thermal properties

Figure 4.20 (a-f) represents the composition dependence (Na_2O mol%) of density, molar volume, elastic modulus, hardness, glass transition temperature, and coefficient of thermal expansion of Li and K substituted glasses. The error in the values is obtained as the standard deviation from measurement repeated 5 times in case of density and Vicker's hardness. Error in glass transition temperature is taken as ±5. Errors in molar volume, elastic modulus, and TEC are smaller than the size of the symbols. While the replacement of Li by Na in NL series glasses (NL05 and NL10) (for nomenclature refer to experimental details in chapter 3) exhibited a decrease in density of the glasses, a similar replacement of K in NK series glasses showed a reverse trend **[Fig. 4.20 (a)]**. The Li ions with higher field strength make a stronger bond with NBOs resulting in shrinking of the Li-NBO bond length, yielding a high glass density. This is in agreement with the XPS analysis of the LCS glass discussed in **section 4.1.4**. On the other hand, K ions being

larger in size, and having lower field strength form weak bonds. Thus, the 15 mol% K_2O glass has a lower density. The variation in the density of the glasses containing more than one type of alkali ions is attributed to the change in the R-NBO bond strength due to the replacement of one type of ions by another one. A similar trend has been observed in binary silicate glasses.[195]

The Vicker's micro-hardness (H) for the NL series glasses as well as the NK series glasses increased non-linearly **[Fig. 4.20 (d)]**. However, the hardness was found to be higher for the NL series glasses compared to the NK series glasses. Nevertheless, the values are in close agreement with other alkali silicate glass compositions.[41,146]

Since molar volume (V_m) is inversely proportional to density, therefore a reverse trend was observed, as shown in **Fig. 4.20 (b)**. V_m for the NL series glasses increased with the increase in Na_2O mol%, whereas it decreased for the NK series glasses. The estimated elastic modulus also showed a similar trend [**Fig. 4.20 (c**)]. In the case of the NL series glasses, stronger bonds influenced the network rigidity leading to a linear increase in elastic modulus, whereas a roughly linear decrease due to weaker bonds was noted for the NK series glasses **[Fig. 4.20 (c)].**

The glass transition temperature (T_g) obtained from the differential thermal analyzer was found to increase for the NL series glasses while it decreased for the NK samples as shown in **Fig. 4.20 (e)**. This is supported by the XPS binding energy in the Si-O bond. The stronger the silicate network, the higher is the T_g and vice-versa.[140] It is also evident from the higher mobility of ions in NL series glasses exhibited by SIMS depth profile and transport inhibiting nature of K-ions in NK series glasses as discussed in chapter 6. The dilatometric results of the present glasses revealed a coefficient of thermal expansion (TEC) in the range of 8-10 ppm/K **[Fig. 4.20 (f)]** which lies well in the expected range of alkali silicate glasses.[140,146] More importantly, it is in close agreement

with TEC of the commercially available soda lime glass as desired for CIGS/CZTS based solar cell substrates,[24] ruling out the possibility of device failure due to thermal expansion mismatch between substrate and thin film. It may be noted that the absorber layers (i.e., CIGS or CZTS) routinely require a post-deposition annealing at temperatures ~ 500 °C for crystallization and densification. Hence, well-matched TEC along with T_g higher than sulfurization temperature (500°C) is a crucial requirement for the substrates on which these films are grown.

The dilatometric study of glasses gives the estimated processing temperature range of all the synthesized glasses. The dilatometric softening temperature (T_d) of NCS glass lies close to 595 °C as given in **Table 4.3**, while that of NL glasses decreases up to 510-530 °C, and the same for NK series glasses increases up to 580-640 °C [**Table 4.6**]. The dilatometric glass transition temperature (T_{gd}) [**Table 4.6]** for glasses is lower than the T_g obtained from DTA owing to the lower heating rate. A variation of 20-30 °C in the measurement of T_g is acceptable from two different methods with different principles.[197]

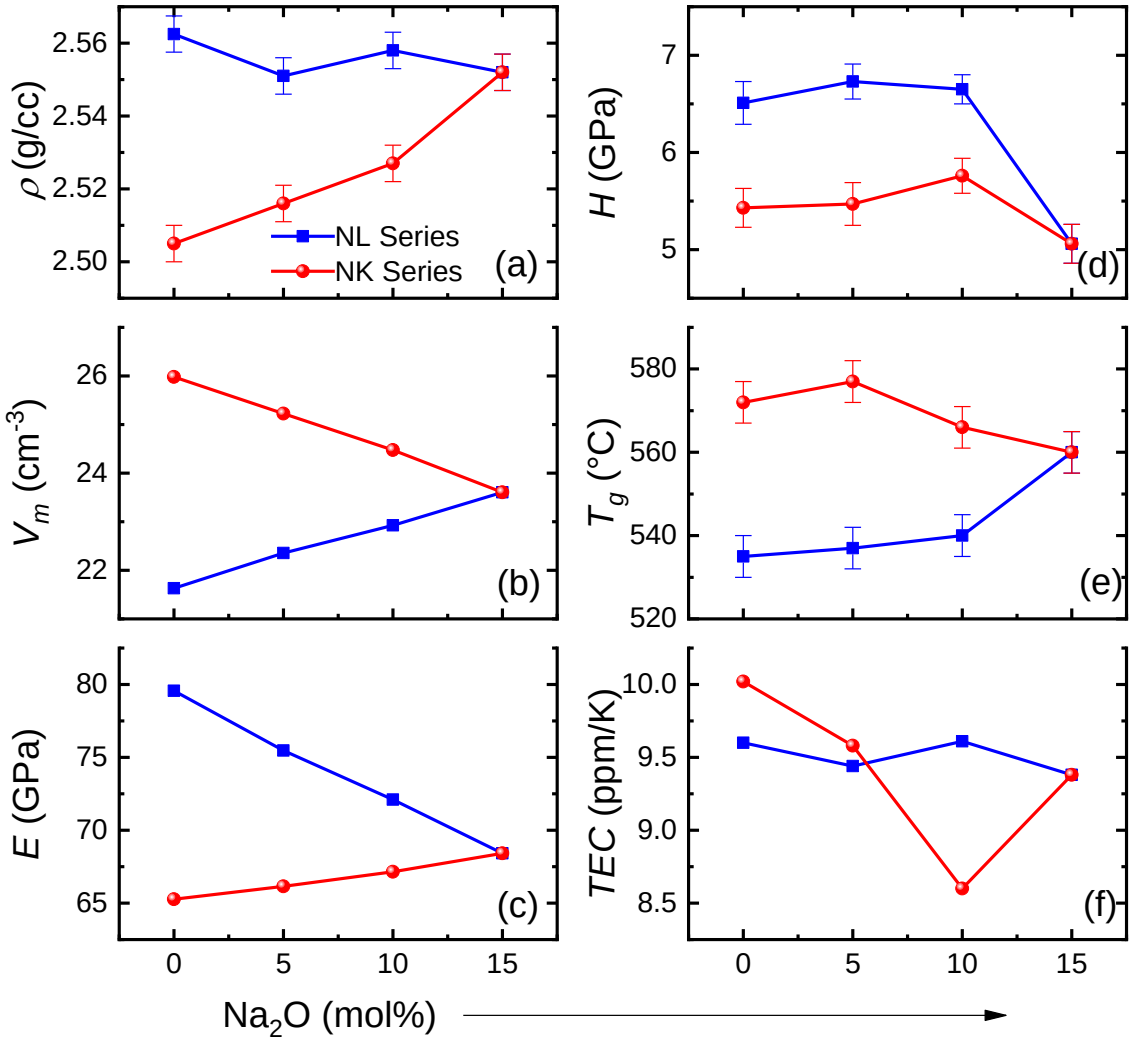

***Figure 4.20**: Composition dependence of (a) density, (b) molar volume (V_m), (c) Elastic modulus (E), (d) Vicker's microhardness (H), (e) glass transition temperature (T_g), and (f) Coefficient of thermal expansion (TEC) for NL and NK series glasses, respectively.*

***Table 4.6:** Coefficient of thermal expansion (TEC) (150-500°C), dilatometric glass transition temperature (T_{gd}) and dilatometric softening temperature (T_d) of all the glass samples.*

Sample ID	**TEC/ppmK^{-1}**	**T_{gd}/°C**	**T_d/°C**
NL05	9.61	495	512
NL10	9.44	511	529
NK05	8.60	542	579
NK10	9.58	572	623

4.2.2. Optical and electrical properties

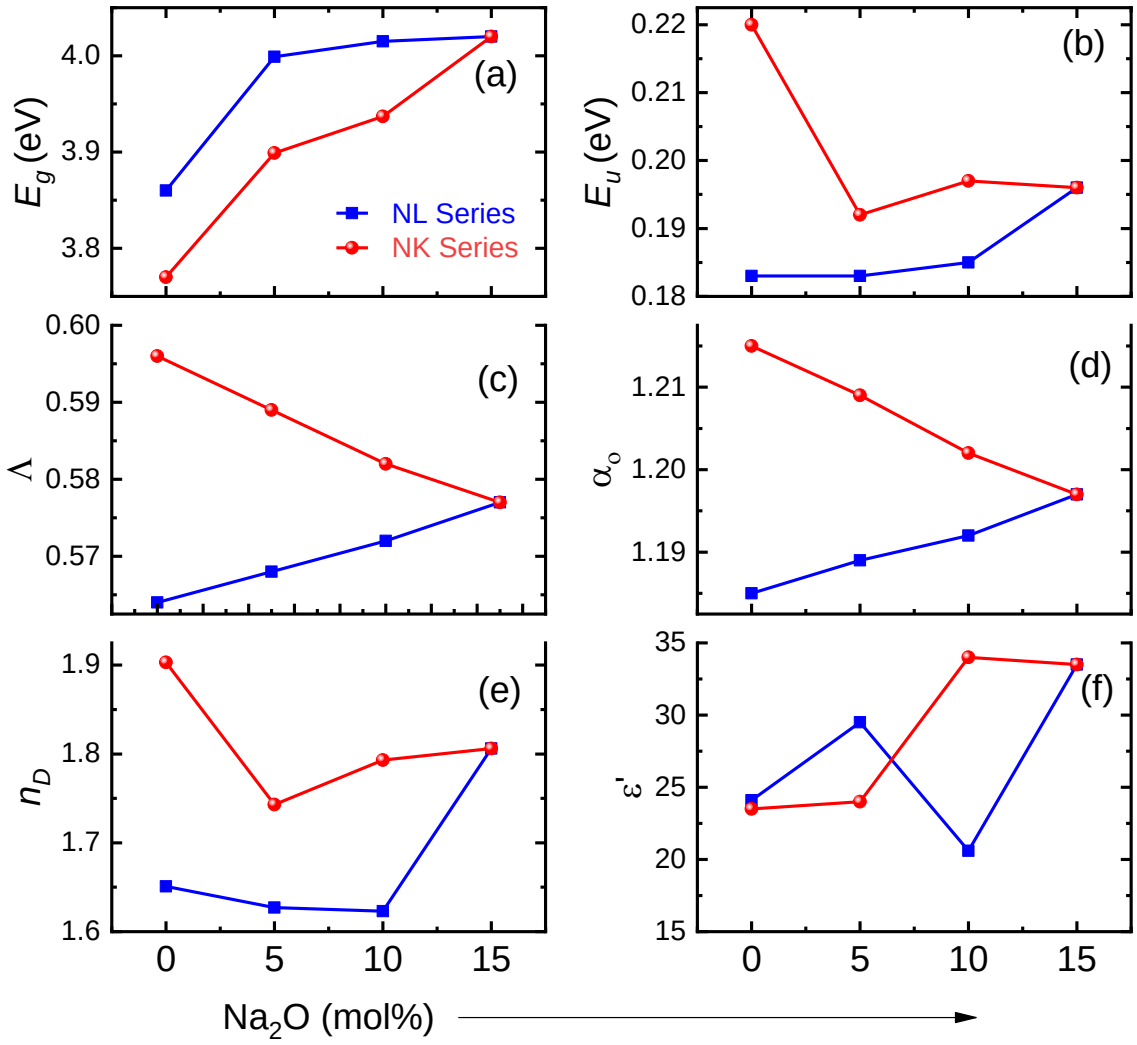

***Figure 4.21**: (a) Optical band gap (E_g); (b) Urbach energy (E_u); (c) optical basicity (Λ); (d) ionic polarizability (α_o); (e) refractive index (n_D); and (f) dielectric constant (ε') (at 1MHz) for NL and NK series glasses.*

The optical properties of glasses give an insight into the ionic and electronic behavior of the glass components when exposed to electromagnetic waves in the range of UV-visible spectrum. **Fig. 4.21 (a)** represents the optical band gap (E_g) obtained from Tauc's plot of respective glasses. With the substitution of Li_2O by Na_2O, E_g increases linearly for NL series glasses, whereas increases abruptly with 5 mol% substitution by Na_2O for NK series glasses. Since, the Li and Na ions have higher mobility as compared to K ions (as evident from electrical properties of NCS, LCS, and KCS glasses), the mixed alkali effect of Li and Na ions in NL series glasses reduces the density of defect

states, due to which E_g increases. E_g increase with the shift of the top of the valence band to the lower energy, while decreases with the increase in the number of NBOs or defect levels close to the top of the valence band.[136,171,198] Moreover, Kaur *et al.* demonstrated that the replacement of heavier ion by lighter ion lowers the top of the valence band, resulting in increasing E_g. Thus, E_g for NL series is higher than NK series.

On the other hand, Urbach energy (E_u) for NL series is lower than NK series glasses **[Fig. 4.21 (b)]**. As discussed earlier in **section 4.1.7**, E_u indicating the number of NBOs is almost similar for mixed NL series glasses, while varies significantly for NK series glasses. It is interesting to note that the difference in ionic radii of Na and K ions is higher than the difference in the Na and Li ions, which also exhibits a higher difference in the density of NK series glasses than in NL series glasses **[Fig. 4.20(a)],** which leads to a higher degree of randomness and disorder in NK series glasses, compared to NL series glasses. It may result in lower diffusivity of ions in NK series than in NL series glasses. The optical basicity of glasses shown in **Fig. 4.21 (c)** is higher for NK series glasses than NL series glasses which can be directly correlated with the higher E_u and T_g of NK series glasses. Optical basicity denotes the tendency of the formation of different structural units consisting of oxide atoms. In general, the greater the number of NBOs, the higher is the optical basicity.[199] The higher the number of NBOs greater is the charge borne by the oxygen ion. **Figure 4.21(d)** represents the oxide ion polarizability of NL and NK series glasses, which is directly derived from the optical basicity of the glass system. The higher α_o of NK series glasses **[Fig. 4.21(d)]** indicate the higher electron donating capacity of oxides in these glasses, which is a result of a higher number of NBOs. Similarly, the lower α_o for NL series glasses demonstrates a lower number of NBOs. Higher NBOs induce a higher coordination state of K ions despite lower attraction from NBOs attributed to lower field strength, as compared to Li and Na ions. Similarly, the higher

refractive index of NK series glasses than NL series glasses, shown in **Fig. 4.21 (e**) is attributed to the higher polarizability in the vicinity of oxygen ions in NK series glasses. As discussed in previous sections, Li ions make stronger bonds with the NBOs which indicate a lower coordination state in the periphery of NBOs. It is due to directionality in bonding nature originating from ion-ion interactions.[200] Thus, Li ions exhibit higher charge sharing with NBOs leading to lower polarizability and hence lower refractive index. It has also been demonstrated in previous reports, that alkali/alkaline earth ions with smaller ionic size possess lower coordination number.[8,142] As a smaller ion can accommodate a lesser number of oxide ions in its periphery, as compared to bigger ion like K, Ba, etc. On the other hand, raised coordination number restricts the mobility of the modifying ions affecting the other transport properties such as dielectric constant, conductivity, and activation energy of conduction. The dielectric constant of the glasses is represented in **Fig. 4.21 (f).** ε' for all the glasses lies in the range of 20-35 without following any fixed trend. It is due to the mixed alkali effect in which local interaction and repulsion among different modifiers ions lead to an anomaly in different properties of glasses.[196,200] While, NL10 glass exhibits a higher dielectric constant than NK10, at 5 mol% Na_2O, it shows a vice-versa character for 10 mol% containing Na_2O glasses (NL05 and NK05, respectively). This anomalous behavior could be attributed to the mixed alkali effect. In general, the dielectric constant value is governed by several phenomena in complex glass structure viz. frequency, temperature, chemical nature, and ionicity of ions. A mixed response from higher polarization in NBOs and lower polarization in BOs attached to Si, B, Ca, and respective alkali ions may have resulted in the ambiguity in the trend.

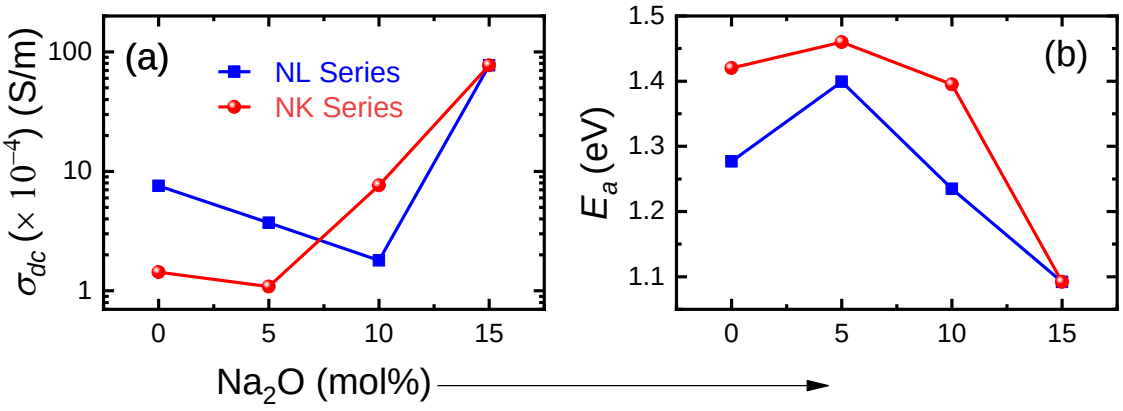

***Figure 4.22**: (a) dc-conductivity (σ_{dc}) at 500°C; and (b) activation energy (E_a) for NL and NK series glasses.*

Figure 4.22 (a) exhibits a similar anomaly in the dc-conductivity of the glasses at 500°C. The conductivity of NL10 with 5mol% Na_2O is higher than NK10, while NL05 with 10 mol% Na_2O is lower than NK05. This shows that the mobility of Li ions is inhibited with the higher percentage of Na while that of K ions is enhanced with the co-existence of Na modifying ions. The corresponding activation energy of glasses is shown in **Fig. 4.22 (b)**. It was calculated from the Arrhenius dependence of dc-conductivity as shown in **Fig. 4.23.** Interestingly, NL series glasses exhibit a saturation region towards higher temperature scales (beyond 450°C), showing saturation of conduction phenomenon. This saturation is attributed to the dominance of temperature dependent mobility in the conductivity equation. With the increase in temperature, the mean free path of mobile charge carrying species (Li/Na ions in NL glasses) reduces, due to which the saturation of conductivity takes place.[201] However, the change in slope in low temperature region from zero to positive values is probably due to the negligible ionization of strongly bonded Li-ions with NBOs in a silicate network. This behavior is not prominent in NK series glasses within the measured temperature range owing to higher ionization energy (or activation energy) corresponding to K-ions as described in **section 4.1.8.** Thus, the Arrhenius dependence of the conductivity of NL series glasses exhibited different phenomenon in three temperature regions. Since, thin-film solar cells

are grown in a particular intermediate temperature range, therefore, the low and high temperature phenomenon does not significantly affect the application of these glasses as substrates.

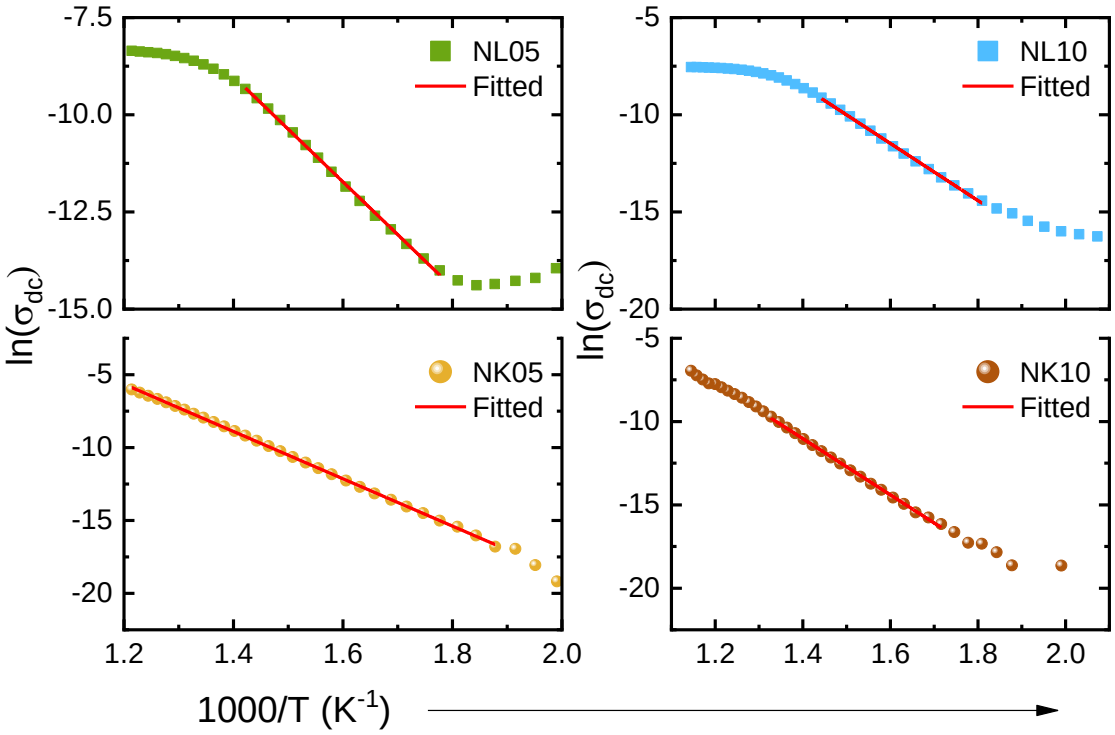

***Figure 4.23**: Arrhenius dependence of (σ_{dc}) for mixed alkali glasses.*

The activation energy of NK series glasses is higher than NL series glasses. This is evident from the higher optical basicity and T_g as discussed above, which lead to higher thermal stability. K ions with higher coordination linked NBOs need greater energy to allow hopping from one interstitial site to another. To understand the anomaly in the transport properties of mixed alkali glasses, the role of Ca as a modifier is intrigued. Ca in the local structure of glasses is believed to have an important influence as it modifies the Q^4 units as ($Q^4 \rightarrow Q^2$).

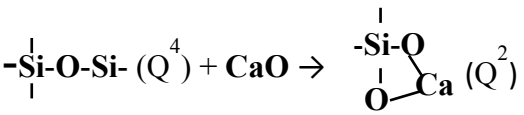

(4.13)

Thus, the simultaneous presence of R ions along with Ca as modifying ions resulted in the cation-oxygen bonds, with combinations of Q^2, Q^3, and Q^4 structural units, with different bond dissociation energies.[127,146] The presence of these units has been shown earlier in these glasses (**section 4.1.2**).[13] It is believed that the alkali ions those out-diffuse to the Mo overlayer originate from the break-down of the bonds with the existing non-bridging oxygens (NBOs) in the local glass structure.[13] It may be noted that the Ca ions in the glass, although are less mobile compared to the alkali ions, significantly influence the transport of alkali ions. The activation energy of conductivity and diffusivity for glasses containing alkali or alkaline-earth ions is influenced by the radius ratio of Ca to alkali ions (R), such that E_a is found to show a minimum for $r_{Ca}/r_R \approx 1$ [**Fig. 4.24].** Molecular dynamic simulation studies on sodium calcium silicate glasses has revealed that the Ca in glass structure has the susceptibility to coordinate with the NBOs, without any variation in coordination number.[202] With a higher field strength than the alkali ions, Ca occupies the sites close to NBOs which fulfills all the structural requirements.[202,203]

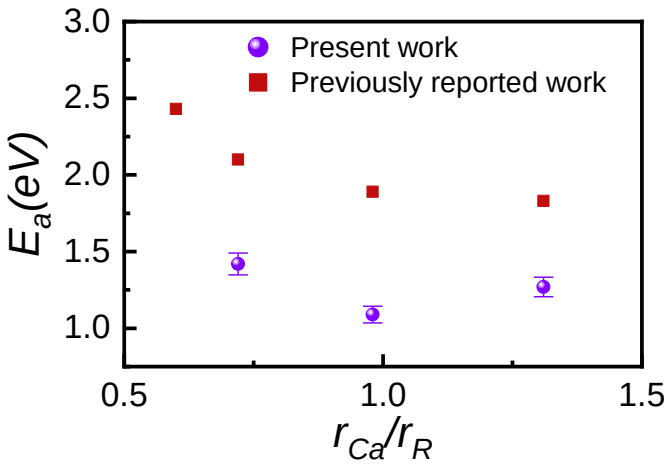

***Figure 4.24**: Variation in activation energy for conduction phenomenon in glasses with calcium to alkali ion radius ratio obtained for present LCS, NCS and KCS glasses[13] and previously reported $R_2O.2CaO.SiO_2$ glasses.*[203]

The ionic radius of both the modifier ions Ca (1.00Å) and Na (1.02Å) is very similar ($r_{Ca}/r_{Na}\approx1$), thus supporting the higher diffusion of Na ions as compared to the other two alkali cations.

Till here, we concluded that for the glasses with mixed alkali ions, the composition has a limiting role in the properties of mixed alkali glasses. In contrast to the reported size-dependent transport mechanism of the ions, we show that the activation energy and the presence of Ca ions as additional modifiers play a crucial role in transport phenomena. In addition to this, NL and NK glasses containing two alkali oxides exhibit anomalous behavior owing to the mixed alkali effect.

The synthesized glasses demonstrate properties deemed suitable for a substrate in thin film solar cells. In the following chapter, we have presented results of optimized growth parameters of Molybdenum thin films (which are typically used as a back electrode in CZTS based thin film solar cells) and diffusion of alkali ions from the glass substrates through the Mo films.

Chapter 5 Optimized parameters of molybdenum thin films

As discussed in Chapter 2, the study of the SLG/Mo/CIGS structure depicts a clear dependence of Na diffusion on the morphology and microstructure of the Mo films.[68] The Na doping level in the CIGS absorber is reportedly proportional to the concentration of Na ions that is accumulated at the interface between the CIGS and the Mo layer. On the other hand, the extent of Na accumulation depends strongly on the surface characteristics of Mo back contact layers.[57,78] Thus, it is very important to grow conducting and uniform Mo films with high control on the microstructure that can provide a better diffusion path for Na from the substrate to the absorber layer and it forms the basis of this work

5.1. Monolayer high pressure deposition (HPD)

As described in the experimental section **[Chapter 3]**, the high pressure deposition (HPD) (at 2.6×10^{-2} mbar) of a single layer (monolayer) at the DC power of 100 W for a deposition time of 20 min yielded Mo films having a black metallic luster and sheet resistance as high as 100 Ω /□. The scotch tape test revealed that the films have well adhered to the substrate as shown in **Fig. 5.1 (a).**

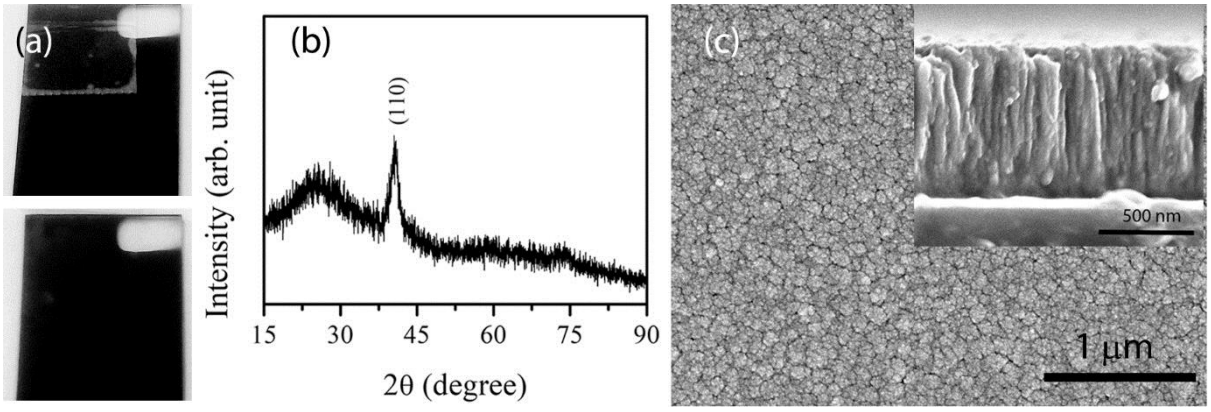

***Figure 5.1**: Properties of the HPD single layer of Mo at 100W for 20 mins: (a) Photographs of samples with the scotch tape and after removing the tape; (b) Typical XRD pattern showing a single peak corresponding to (110) plane of cubic Mo; (c) FESEM micrograph of surface microstructure of the film with cross-sectional view as the inset. Note the micro-cracks in the films.*

The XRD pattern of the film **[Fig. 5.1 (b)]** is characterized by a clear Bragg peak at about 40.55° corresponding to the (110) plane of cubic Mo (ICDD Card No. 3-065-7442). However, relatively higher full width at half maximum (FWHM) and low intensity of the peak indicates poor crystallinity of the film, despite having a film thickness as high as ~770 nm as revealed from the cross-sectional FESEM micrographs as given **in inset of Fig. 5.1 (c)**. The surface of the film was found to be covered by particles of random shape and size **[Fig. 5.1 (c)],** typical of the DC sputtering. More importantly, there were visible cracks across the films, which might be the reason for discontinuity in the granular structure of the thin film. As a metallic (conductor) Mo conducts current through grains, more cracks result in lower conductivity and hence high sheet resistance of the film. The observed film properties are consistent with the earlier studies, for example, of Li *et al.* who have reported a decrease in conductivity and improvement in adhesion with an increase in the pressure from 4×10^{-3} to 2×10^{-2} mbar. [75].

5.2. Bilayer deposition with variation in deposition power

In contrast, bi-layers offer a solution towards achieving simultaneously very low electrical resistivity and high adhesion, as demonstrated previously.[74,76] We have prepared a bilayer of Mo films through HPD (at 2.6×10^{-2} mbar) followed by LPD (at 2.6×10^{-3} mbar) at various DC power. For direct comparison, deposition time was kept constant for all samples. It may be noted that the power used in the present work is much lower than that employed previously,[71,76,204] to improve the energy cost of the process.

5.2.1 Structural and microstructural analysis

Figure 5.2 (a) shows the typical XRD pattern of the bi-layered films on the SLG glass substrates. Two peaks at about 40.35 and 73.42° with high crystallinity were observed for all patterns which are identified with the (110) and (211) planes of cubic Mo, respectively. The preferential growth of Mo along (110) plane is attributed to the

high density of (110) planes in the BCC structure of Mo film compared to (211).[205] The inset to **Fig. 5.2 (a)**, shows the zoomed-up region around the (110) peak of the films, which indicates a marginal shift of the peaks towards lower 2θ values suggesting the increase in the compressive stress in the films[76] with increasing deposition power. It is attributed to voids created in the crystalline lattice formed with the bombardment of grain boundaries with energetic ions.[75,204] It is interesting to note, however, that the average grain size calculated using Scherrer's formula remained unaffected by the power, as listed in **Table 5.1**.

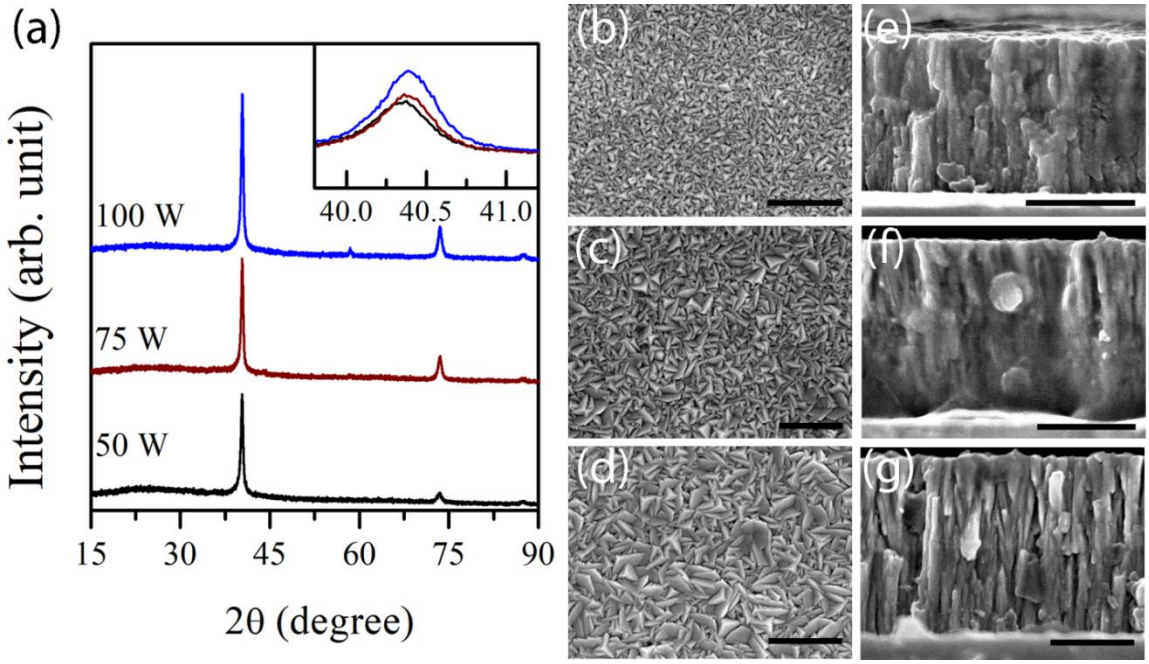

***Figure 5.2**: Typical XRD patterns of bilayered Mo films grown at 50, 75 and 100 W. For all samples bottom layer was deposited for 20 min and the top layer was for 30 min; Surface and cross-sectional microstructure of the corresponding films, (i.e, (b) & (e) for 50 W, (c) & (f) for 75 W and (d) &(g) for 100 W). Scale bar in all FESEM micrographs corresponds to 500 nm.*

The corresponding changes in the microstructure due to the increase in DC power are shown in **Figs. 5.2 (b-g)**. The FESEM micrographs indicate a leafy microstructure at the top surface of LPD film for all powers, which is very different from that observed in **Fig. 5.1 (c)** (single HPD layer). A close inspection of the micrographs **[Figs. 5.2 (b-d)]** reveals that with an increase in power, the average size of the particles covering the

surface increased, which resulted in lower packing density. This is also reflected in the cross-sectional micrographs in **Figs. 5.2 (e-g).** These micrographs also show that the thickness of the films increased from 0.7 μm at 50 W to 1.0 μm at 100 W, which is understood on the basis of increased sputtered yield at higher DC power.

Table 5.1*: Details of the samples, deposition condition and the analysis of the (110) peak in the XRD patterns.*

Sample ID	Deposition condition*			Analysis of the (110) peak			
	DC power (W)	HPD time (min)	LPD time (min)	2θ (degree)	FWHM (degree)	Crystallite size (nm)	Strain $(\frac{\Delta a}{a} \times 100)$
100 W (20/0)	100	20	0	40.55	1.8908	4.68	0.09825
100 W (20/30)	100	20	30	40.37	0.5106	17.32	0.30613
75 W (20/30)	75	20	30	40.35	0.4971	17.79	0.35106
50 W (20/30)	50	20	30	40.32	0.5107	17.31	0.44093
50 W (30/30)	50	30	30	40.38	0.5681	15.57	0.30613
75 W (20/40)	75	20	40	40.37	0.5566	15.89	0.30613

** HPD (high pressure deposition) ~ 2.6×10^{-2} mbar; LPD (low pressure deposition) ~ 2.6×10^{-3} mbar; Base pressure was better than 5.0×10^{-6} mbar.*

5.2.2. Electrical and adhesion test

The electrical properties and the results of the adhesion test are summarized in **Figs. 5.3 (a)** and **5.3 (b-g)**, respectively. The sheet resistance of the 50 W bi-layered film was determined to be ~13 Ω/□, which is very low compared to that obtained for the single HPD film grown with 100 W (~104 Ω/□). The sheet resistance further decreased sharply with an increase in the DC power and remained constant at ~4 Ω/□. On the other hand, all samples exhibited equally good adhesion to the substrate. The results clearly show that the LPD improved the electrical conductivity of the samples, for example from the comparison of sheet resistance of the 100 W HPD (of 20 min) sample with the bi-layered 100 W (20/30) (i.e., HPD of 20 min followed by LPD of 30 min).

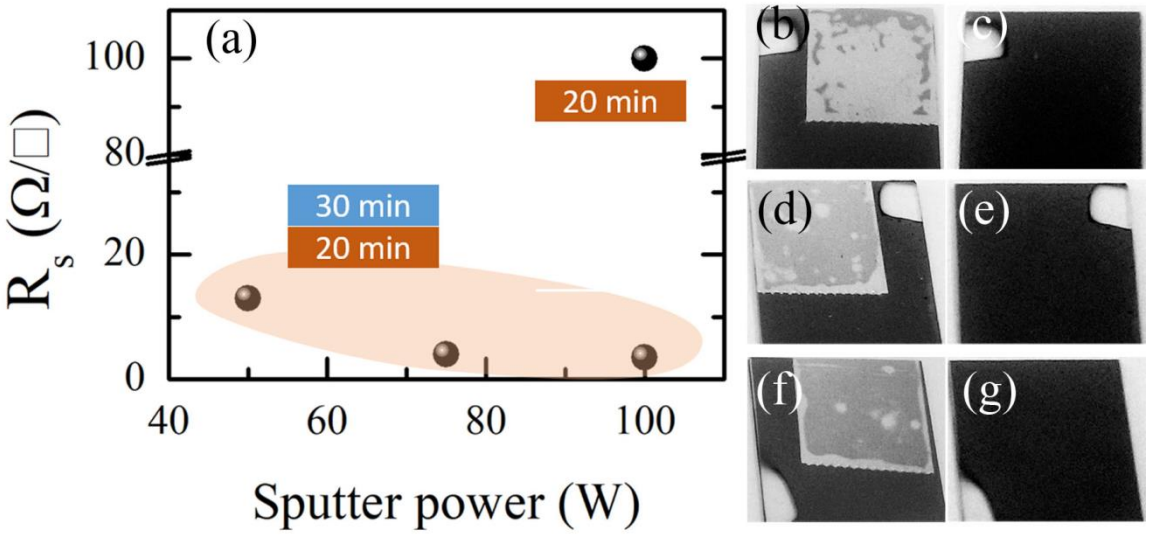

Figure 5.3: *(a) Plot of variation in sheet resistance versus DC sputtering power. The highlighted data points correspond to the bi-layered samples shown in the figure. The value for the single-layer film gown at 100 W is also shown. Photographs of the samples with the scotch tape and after removing the tape grown at 50 W (b & c), 75 W (d & e), and 100 W (f & g). The films clearly show strong adhesion to the substrate.*

5.3. Bilayer deposition with variation in deposition time

While the LPD is clearly shown to improve the conductivity of the samples, we investigated the role of HPD by preparing a bi-layered sample grown at 50 W (30/30) (i.e., with HPD of 30 min followed by LPD of 30 min). It provides easy access to compare with the sample 50 W (20/30), just discussed above. The XRD pattern of this film is given in **Fig. 5.4 (a),** which shows the presence of a low intensity peak at 58.5° corresponding to the (200) plane of cubic Mo and two unidentifiable peaks at ~ 43° and 50°, in addition to the (110) and (211) peaks. These additional peaks which were not present in the 50 W (20/30) sample **[Fig. 5.2 (a)]** are clearly due to the increased thickness of the HPD layer. The analysis of the (110) peak revealed a decrease in the lattice strain **[Table 5.1]** suggesting that with an increase in thickness the stress is relieved in the films. However, there was no significant change in the microstructure as observed from the FESEM micrographs of the surface and cross-section of the films **[Fig. 5.4 (b-c)]**. The sheet resistance of the film marginally decreased to 10 Ω/□ from 13 Ω/□

for the 50 W (20/30). The results indicate that the electrical conductivity is nearly independent of the thickness of the bottom HPD layer beyond a reasonable thickness, and hence, the top LPD layer must be further optimized to obtain lower resistivity.

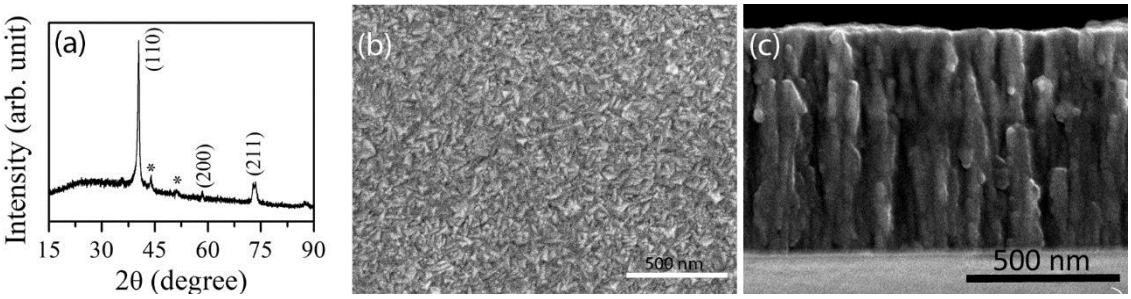

Figure 5.4: (a) *Typical XRD pattern, (b) surface micrograph from FESEM and (c) cross-sectional micrograph of bi-layered Mo film deposited at 50 W (30/30). The asterisk (*) in the XRD pattern indicates un-identified peaks. The scale bar in FESEM micrographs corresponds to 500 nm.*

5.4. Optimized deposition condition

Since there was not a significant difference between the sheet resistance of the 100 W (20/30) sample and the 75 W (20/30) sample, we proceeded to optimize the films at 75 W as deposition at lower power indicates a lower energy budget. While the duration of the HPD was kept fixed at 20 min, we increased the duration of the LPD to 40 min.

Fig. 5.5 shows the typical XRD pattern, optical transmittance and reflectance curves, surface and cross-sectional microstructure of the film. The results revealed the formation of a strongly (110) oriented film. As expected, the films exhibited high reflectance and negligible transmittance in the wavelength range of 350-1400 nm. Zero transmittance in the optical region indicates the opaque nature of the Mo-thin film. This also verifies that no transmission of sunlight takes place from the bottom contact layer through a transparent glass substrate to the p-type absorber layer. The curves are typical of good quality Mo films and are similar to the ones reported in the literature [68,71]. More importantly, the surface morphology was found to change from leafy structure (75 W (20/30), **Fig. 5.2 (c)**) to densely packed pyramidal type structure [**Fig. 5.5 (c**)], which was

also supported by the cross-sectional micrograph shown in **Fig. 5.5 (d)**. The resistivity of the sample was found to be 1.8×10^{-4} Ω.cm, which is the lowest among all samples studied in this work and is smaller by at least an order of magnitude than the 50W (30/30) sample (20.4×10^{-4} Ω.cm). It may be noted here that Mo films of similar resistivity are used in CIGS based solar cells.[206] This remarkable improvement in electrical conductivity is clearly due to the increased thickness of the LPD layer. In addition, this sample (75 W (20/40)) passed the adhesion test.

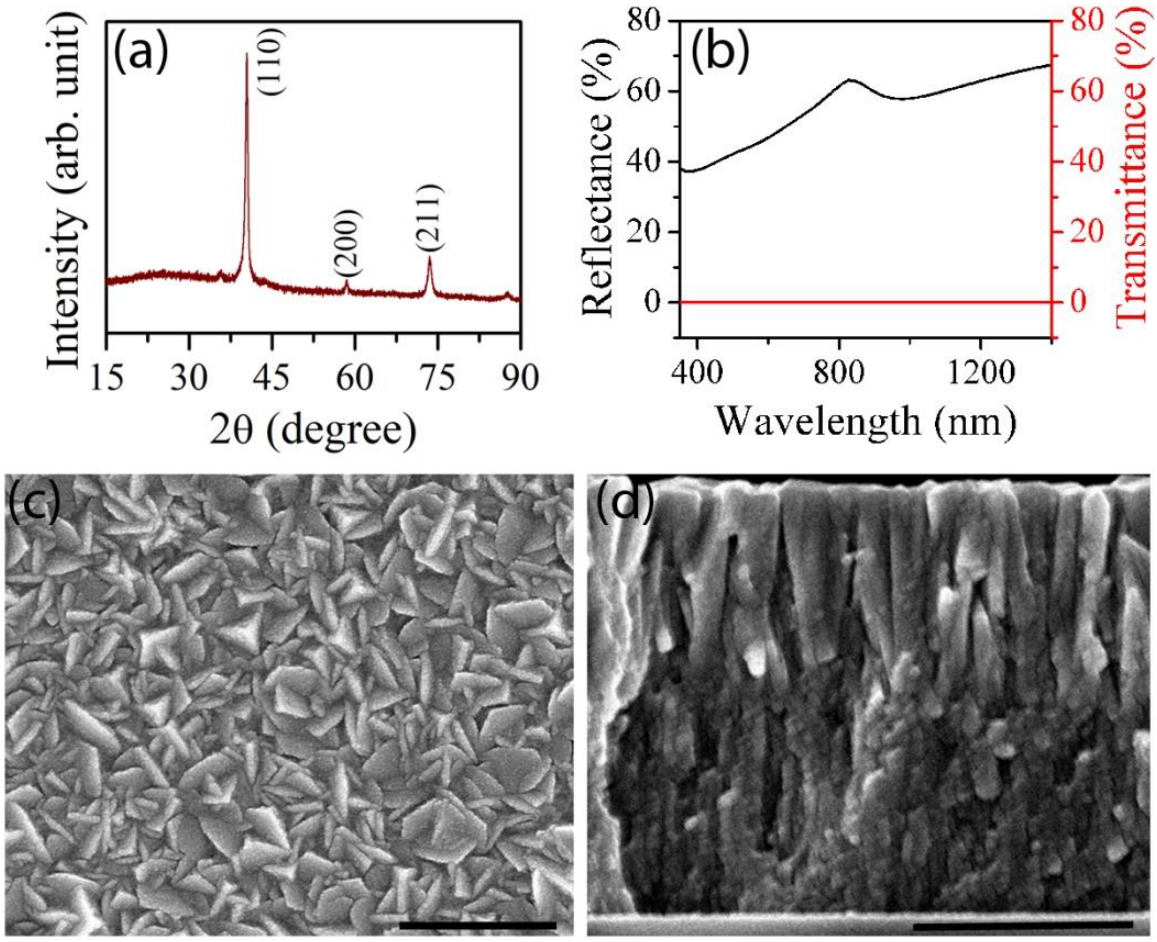

***Figure 5.5**: (a) XRD pattern, (b) optical transmittance and reflectance curve, (c) surface micrograph from FESEM and (d) cross-sectional micrograph of bi-layered Mo film deposited at 75 W (20/40). The scale bar in FESEM micrographs corresponds to 500 nm.*

As discussed previously, apart from very low resistivity and high adhesion to the substrate, the back electrode in the CZTS based solar cells is expected to have a

microstructure that allows efficient Na diffusion. Thus, Na as well as K, and Li diffusion profile is evaluated using SIMS in the next chapter.

Chapter 6 Effect of glass composition on out-diffusion of alkali ions into Mo thin films

The Mo films were deposited as per the optimized conditions of 75W (20/40 min) as discussed in the previous chapter onto the synthesized NL and NK series glass substrates. The as-deposited Mo films on different substrates were annealed at 500 °C for 1 h in a vacuum. This annealing profile is similar to the sulfurization process commonly adopted during the growth of phase pure CZTS absorber layers. The extent of diffusion of the alkali ions into the Mo overlayer was examined by SIMS. Since the Mo films were sputter deposited in identical conditions, the observed variations in the SIMS profiles clearly indicate the limiting role of substrate composition on alkali ions diffusion. It may be noted that the intensity (counts) pertaining to a particular element can vary due to the variation in sputter rate during the SIMS measurements; hence we have normalized the alkali ion intensity with the Mo intensity and plotted the normalized intensity ([R]/[Mo]) (R=Na/Li/K) with respect to thickness for different samples. The normalized profiles assist in an easy comparison since the Mo films were grown on glass substrates (GS) in identical conditions, thus minimizing the error in estimating the intensities of the alkali ions.

6.1. Diffusion of alkali ions from glass substrates

Typical SIMS profiles of individual alkali ions such as Li, Na, and K from NCS, LCS, and KCS, respectively, normalized with respect to Mo are shown in **Fig. 6.1.** The figure exhibits the highest diffusion concentration for Na compared to Li and K. Furthermore, although the glasses contain equal mole percentage of the alkali ions in their respective glass substrates (i.e., 15 mol%), their extent of diffusion from glass to the Mo film varies significantly. Considering that the Mo films on different glass substrates were deposited in the same conditions, the structure or morphology of the Mo films resulting in

the observed variation in the diffusion profiles is ruled out.[166,191,207] This indicates the critical influence of the composition on the out-diffusion of the alkali ions. The higher potential of Na ion to escape from the glass surface as compared to the other alkali ions is in agreement with our earlier study **(section 4.1.8)**, which revealed the self-diffusion coefficient of Na-ions in NCS glass is higher followed by Li and K-ions in LCS and KCS glasses.[13]

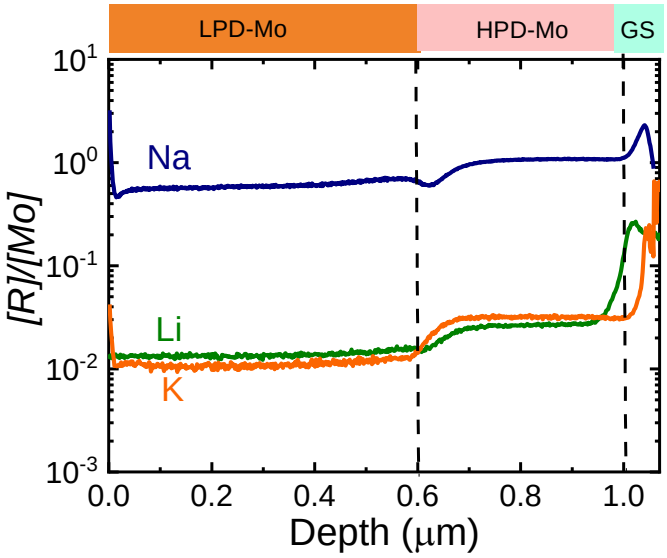

Figure 6.1: *Normalized SIMS depth profile of [R]/[Mo], where R stands for Li, Na and K from LCS, NCS and KCS glass substrate (GS), respectively, to high pressure deposited-Mo (HPD-Mo) followed by low pressure deposited-Mo (LPD-Mo) thin films, respectively.*

The trend in diffusivity obtained experimentally from impedance spectroscopy and that from the SIMS are in direct correlation. Similar and comparative diffusivity statement has been established by Natrup *et al*. as revealed from the tracer method, SIMS, and impedance analyses.[177] While, the ionic radii are considered to govern the transport phenomenon of alkali ions in glasses,[131,138] the out-diffusion profile of the alkali ions in the present case does not follow any trend. In order to understand the above anomaly, the local chemical environment of the glasses was studied using the XPS spectra as discussed in **section 4.1.4**. The lower binding energy for Si-O bonds in Li containing glass (i.e., LCS) yielded the formation of stronger Li-NBO bonds, resulting in lower mobility and

diffusivity of Li-ions. On the other hand, the hindrance to the diffusion of K-ions is evident from the bigger ionic radii.

6.2. Diffusion of alkali ions from mixed alkali containing glass substrates

Glasses with two types of alkali ions (mixed alkali glasses) are known to exhibit a typical non-linearity in their properties.[195,196,208] Though not well defined, the non-linearity is by the virtue of mobility of one alkali ion in the presence of another alkali ion with a different ionic radius.[195,196] It seems that the presence of two or more alkali ions in glasses has a localized competitive effect, analogous to localized electron-electron interactions in conductors.[209,210] In the following sections a detailed analysis of the diffusion of the alkali ions in an environment containing multiple ions is presented.

6.2.1. Out-diffusion of Na ions

Figure 6.2 (a) shows the normalized depth profile corresponding to Na-ions for NL05 (10 mol% Na_2O and 5 mol% Li_2O) and NK05 (10 mol% Na_2O and 5 mol% K_2O) glasses. Although, the concentration of Na in both the glasses is the same (i.e., 10 mol%), the extent of diffusion is higher in NL05 glass containing Li_2O than that in NK05 glass containing K_2O. Similar results were also obtained for NL10 (5 mol% Na_2O and 10 mol% Li_2O) and NK10 (5 mol% Na_2O and 10 mol% K_2O) glasses, as depicted in **Fig 6.2 (b).** It appears that the presence of Li facilitated the out-diffusion of Na whereas the K ions inhibited the same. It can be evidently correlated to the mobility of alkali-ions, which influences their diffusivity and hence, the conductivity of the glasses owing to the mixed alkali effect.[13]

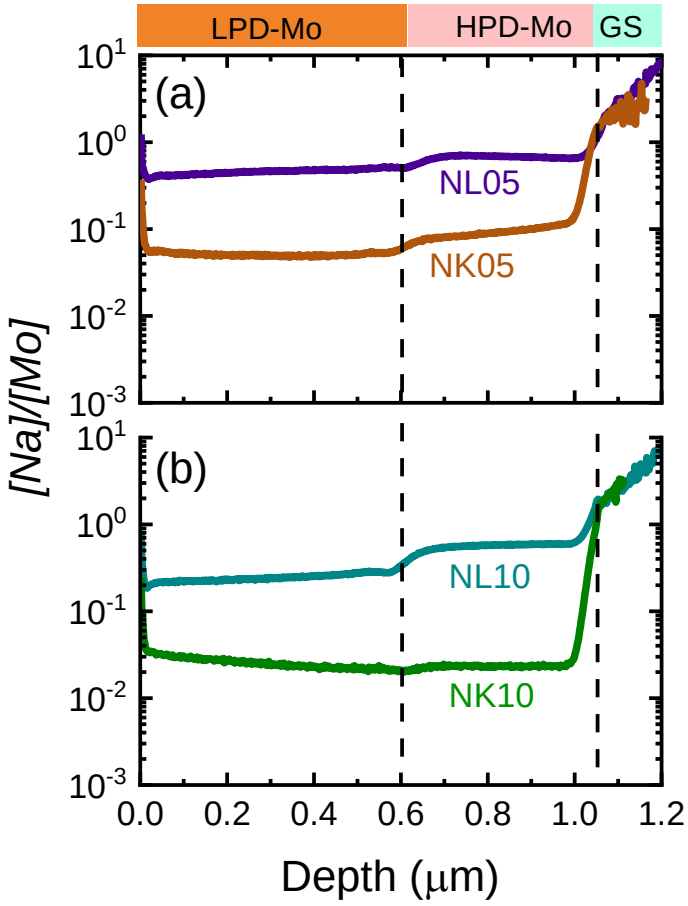

Figure 6.2: *Normalized [Na]/[Mo] depth profile as obtained from SIMS for glasses containing (a) 10 mol% Na_2O with 5 mol% Li_2O and K_2O and (b) 5 mol% Na_2O with 10 mol% Li_2O and K_2O, respectively.*

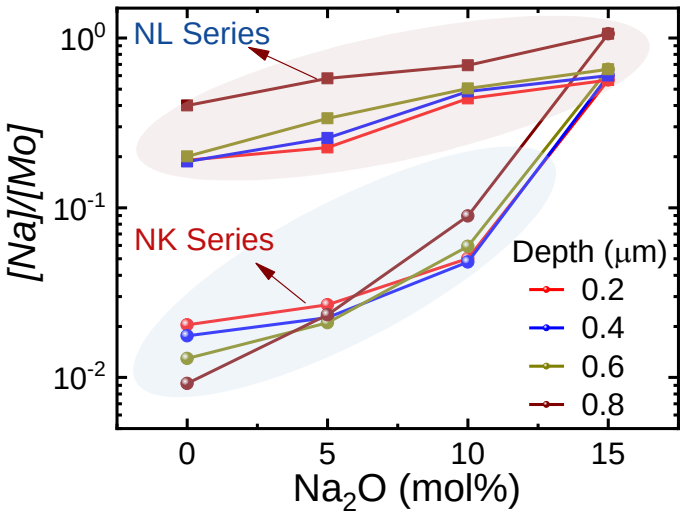

Figure 6.3: *Variation in Normalized [Na]/[Mo] content with mol% Na_2O present in substrate composition for NL and NK series glass substrates, respectively, taken at different depth positions.*

The presence of multiple modifier ions (Na, Li, K, and Ca) in the glass composition leads to a complex structural role of different ions in the modification of the glass network that critically affects the out-diffusion of the Na ions, as evident from **Fig 6.3**. The figure shows the variation of Na concentration (normalized with respect to Mo) with the composition of the glasses at different depths from the surface. The figure clearly shows a higher amount of Na at all depths for the NL series glasses than that of the NK series glasses. The trend is in direct correlation with the glass activation energy E_a (**Fig. 4.22 (b)**). For both NL and NK series glasses, the values of E_a decreased non-linearly with an increase in the Na composition in the glasses. However, always a higher value of E_a was obtained for the NK series glasses, suggesting a decreased mobility of ions due to localized interaction among different ions or a potentially higher energy barrier for out-diffusion of Na ions into the Mo overlayer.

6.2.2. Out-diffusion of Li/K ions

The anomalous behavior of Li and K-ions is intrigued by studying the diffusion profile of Li and K-ions in the respective glasses. **Figures 6.4 (a-b)** present the normalized Li/K depth profile for the NL and NK series glasses, respectively. The diffusion extent of Li and K ions in respective glasses is lower by 2 orders of magnitude as compared to that of Na. The extent of diffusion of Li **(Fig. 6.4 (a))** increased with the concentration of Li in the substrate composition, while that of K **(Fig. 6.4 (b))** remained nearly the same and negligible irrespective of the K-composition. It indicates that the diffusivity of Li-ions is not much influenced by the presence of Na ions. On the other hand, the diffusivity of K-ions from glasses containing 5 and 10 mol% Na_2O is slightly higher than KCS glass without having Na. It shows that Na-ions support the diffusivity of both Li-ions as well as K-ions. The higher activation energy **(Fig. 4.22 (b))** and glass

transition temperature **(Fig. 4.20 (e))** for NK series glasses evidently show that the K-ions are strongly bound in the glass network that yields negligible mobility of ions.

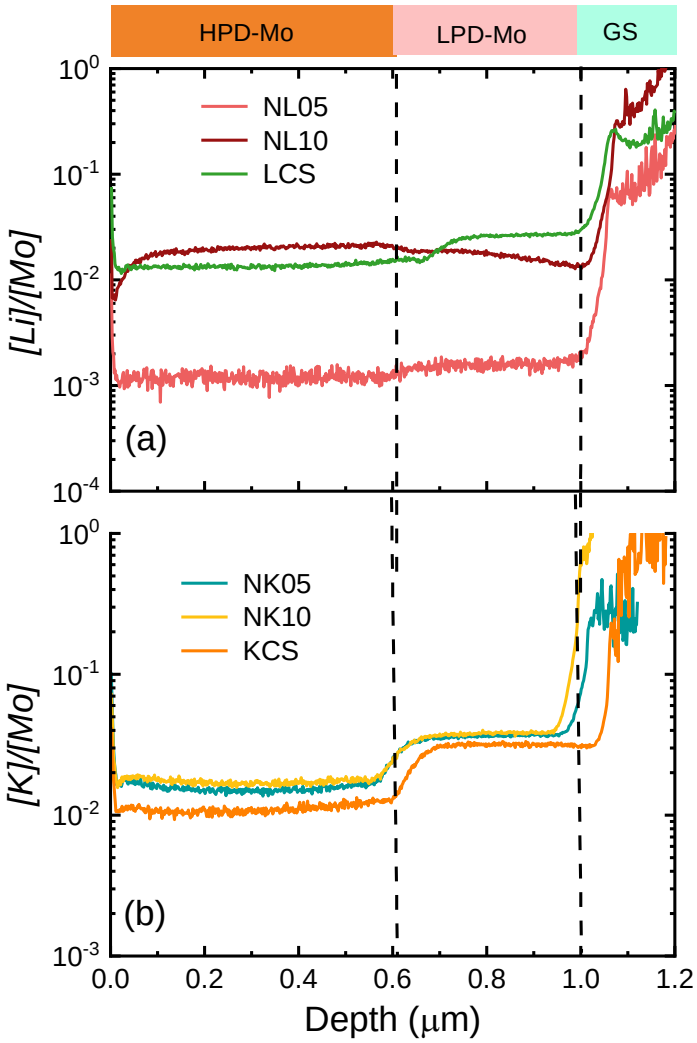

Figure 6.4: *Normalized depth profile of (a) [Li]/[Mo] and (b) [K]/[Mo] in the bilayer Mo films from respective glass substrates.*

Discussions in the preceding sections elucidated the limiting factors for out-diffusion of alkali ions in the glasses with intentionally incorporated excess alkali ions. The diffusion of alkali ions into the sputter-deposited Mo overlayer is revealed to have a complex dependence on the composition and the local glass structure. The Na ions exhibit the highest extent of diffusion among the alkali ions present in glass substrates, while that for the K-ions is the lowest. For the glasses with mixed alkali ions, the presence of Li

facilitated the out-diffusion of Na, whereas K ions appear to inhibit the same. Mechanism behind this is discussed in detail in **section 6.4.** Similar composition dependence of alkali ion diffusion is discussed by Neeway *et al*. in nuclear waste glasses.[211] Moreover, the NCS glass substrates exhibited comparably better properties than commercial SLG (as evidenced from **section 4.1**). Thus, we have carried out a comparative study on the diffusion of Na ions from NCS and SLG glass substrates in different deposition and annealing conditions.

6.3. Comparison of diffusion of Na in SLG and NCS

Figure 6.5 shows the normalized SIMS profiles of the as-deposited and annealed bi-layered 75 W (20/40) Mo film on the NCS and SLG substrates, respectively. Interestingly, the normalized count rate for Na remained constant up to a depth of about 600 nm, then increased by an order of magnitude till a depth of 1000 nm from surface followed by a further increase by another order of magnitude. These three regions correspond to the LPD, HPD layers, and the SLG substrate, respectively. From the FESEM cross-sectional micrograph (**in chapter 5, Fig 5.5**), this depth corresponds to the interface between the LPD and HPD Mo layers. The normalized profile of Na with respect to Mo counts suggests out-diffusion of Na from the substrate into the Mo film even for deposition at room temperature. This might be due to the energy transfer of the depositing species to the glass substrate. Furthermore, the three-step variation in the concentration of Na indicates that as Na diffuses from substrate to the Mo layer, the Na concentration drops for HPD layer in comparison to that in the bulk of the substrate. A further decrease in Na concentration in the LPD layer is observed, which is attributed to the change in packing density and compactness of grains from the HPD to the LPD layer. The quantitative observation presented in this work is similar to the earlier reports of

change in Na concentration due to a change in deposition pressure that affected the microstructure of the Mo films.[68]

For the samples annealed at 500 °C (the temperature similar to the post-deposition sulfurization treatment given to the CZTS films in solar cells), significant out-diffusion of Na was observed. The HPD layer appears to act as a reservoir for Na ions in its voids/cracks, owing to its cracked/porous morphology. A similar trend was also noted for the NCS sample as shown in **Fig. 6.5.**

While the commercially available SLG has ~15 mol% Na_2O,[13] similar to the synthesized NCS glass, the rest of the composition slightly varies. The Na depth profiles shown in **Fig. 6.5** demonstrates significantly higher diffusion of Na from synthesized NCS glass substrate in comparison to the SLG, in both as-deposited and annealed Mo films. Such enhanced diffusion of Na in NCS is evident as a consequence of the structural and compositional variance as discussed earlier in **section 4.1.** The Na diffusion in substrates is in agreement with the diffusion results obtained using conductivity analysis from the Nernst-Planck equation (4.14), which revealed a higher Na diffusion in NCS glass in comparison to that in SLG.

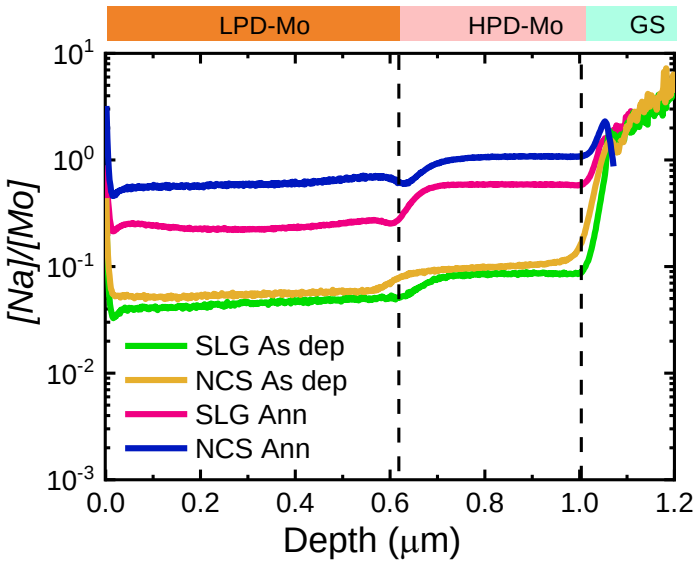

***Figure 6.5**: Comparative Na diffusion profile from NCS and SLG substrates to as-deposited and annealed Molybdenum thin films, respectively.*

Furthermore, in order to understand the interfacial mechanism of the alkali ion diffusion from the substrate to Mo film, a detailed mathematical formulation, and analysis of the diffusion profile is discussed in the following sections.

6.4. Mechanisms of alkali ion diffusion

The variation in the extent of diffusion of alkali ions clearly suggests a strong dependence of out-diffusion on the composition of the glass substrates. While the enhanced out-diffusion of alkali ions from the substrate to overlayers is highly desired in thin film solar cells,[212] the kinetics behind this transport of ions via the interface between the glass and Mo films is of keen interest.

Self- and inter-diffusion of alkali ions from glass substrate to other neighboring parts of the device has been an intriguing subject by virtue of its effect on the functioning of devices. For instance, in Li/Na ion solid state batteries consisting of glass electrolytes,[129,183,213] thin film solar cells, bioactive glasses, and glass-ceramics[3,145,214] the mobility and inter-diffusivity of alkali-ions play a very important role in interlayer compatibility and performance of the device. The mobile nature of charge-invariant monovalent alkali ions is primarily dependent on its ionic size and the size of the vacant sites.[215] These ions undergo diffusion via hopping from one interstitial site to another.[216] The diffusion of alkali ions in glasses can be categorized in three ways: (i) diffusion of alkali ions within the glass, termed as self-diffusion hereafter. It is perpetuated by the presence of vacant interstitial sites close to non-bridging oxygens (NBOs) in the glass structure[149,191] and is primarily investigated on the basis of the electrical transport properties;[13] (ii) out-diffusion of alkali ions from glass to the interface, termed as leaching in the glass/aqueous environment;[217] which is expected to deteriorate the chemical durability of the glasses, and (iii) impurity diffusion, termed as

inter-diffusion, perpetuated by the concentration gradient of ions at the interface of two materials such as glass/thin film.[211]

The alkali ion migration from the glass to a thin film is a function of local structure and composition of glass,[211,218] structure and morphology of the thin film deposited onto the glass substrate,[219] and the quality of the interface between glass and thin film. The ion transport is caused by thermal energy and a concentration gradient, as defined by Fick's laws of diffusion. In addition, the diffusion also depends on the structure of solid, such as glassy materials having more open structure exhibit a higher probability of diffusion than its crystalline counterpart.

6.4.1. Diffusion profile fitting using the Fick's law

Assuming that the glass substrates act as a reservoir of alkali ions those diffuse into the Mo overlayer, we have fitted the diffusion profile using Fick's second law The diffusion of alkali ions via the glass/Mo interface is directly measured from the SIMS depth profile. The counts in the SIMS data correspond to the concentration *C(x,t)* that varies with depth (*x*) and diffusion time (t). It can be modeled using Fick's second law of diffusion given by

$$\frac{\partial C(x,t)}{\partial t} = D(x)\frac{\partial^2 C(x,t)}{\partial x^2} \qquad \textbf{(6.1)}$$

Where, *D(x)* is the diffusion coefficient, assuming that the diffusion of alkali ions in Mo film takes place primarily through grain boundaries.

The typical SIMS diffusion profile is divided into two portions, as shown in **Fig. 6.6.** The first portion corresponds to lattice diffusion in region I (the interfacial region between the glass substrate and Mo thin film) and the second portion corresponds to grain boundary diffusion in region II (Mo film away from the interface).[220,221] The lattice diffusion part is fitted with **Eq. 6.4 (given below)** to estimate the lattice diffusion constant (D_L) with boundary conditions mentioned in **eqs. 6.2-6.3**.[191,221]

In the numerical fitting of the data, it is assumed that there are no alkali ions at any position ($0< x \leq L$) in the Mo film at the beginning of the diffusion process, *i.e.*

$$C(x, t) = C_o \text{ ; when } t=0 \qquad \textbf{(6.2)}$$

Furthermore, the glass substrate is treated as a constant source of alkali ions, such that the concentration at the glass surface (i.e., $x = 0$) for all times is

$$C(x, t) = C_s \text{; when } x=0 \qquad \textbf{(6.3)}$$

The solution of equation 6.1 is given by

$$\frac{C_s - C(x,t)}{C_s - C_\infty} = erf\frac{x}{2\sqrt{(D_L.t)}} \qquad \textbf{(6.4)}$$

where, C_∞ is the concentration of diffusing ions at an infinite distance from the source. In the present case, since we are considering the diffusion of alkali ions in a few hundred nanometre range of the film, we assume C_∞ as the concentration of alkali ions where the grain boundary diffusion region begins (**Fig. 6.6**).

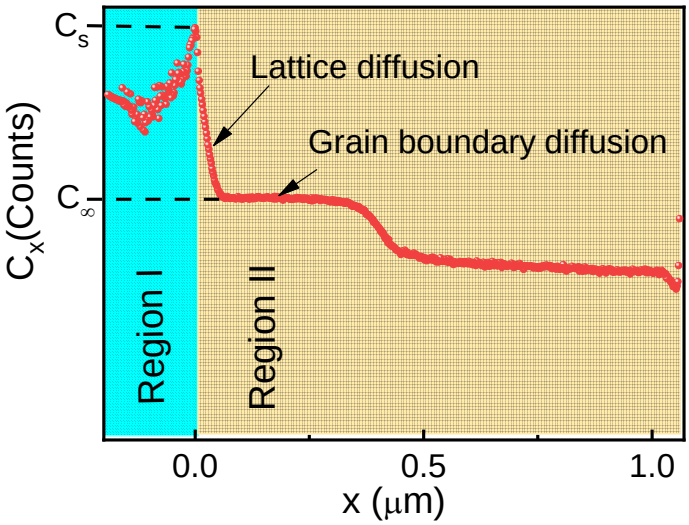

***Figure 6.6**: Representative SIMS depth profile showing region I corresponding to glass/Mo interface and region II belonging to Mo-bilayer thin film.*

The fitted diffusion profiles for Na, Li, and K ions in the region from the glass surface to the point where grain boundary contribution begins for NCS, LCS, and KCS glass substrates, respectively are shown in **Fig.6.7**.

The error function fitted profiles of Na and Li ions for NL05 and NL10 glass substrates and of Na and K ions for NK05 and NK10 glass substrates are presented in **Figs 6.8.** The corresponding lattice diffusion coefficient (D_L) for all the profiles is tabulated in **Table 6.1**. The adj. R^2 values exhibit a good quality fitting of the depth profiles **(Table 6.1)**. The diffusion coefficient provides information about the rate of diffusion, i.e., the higher the D_L, the faster is the process of diffusion. Alongside, the lattice diffusion length (d) and Le Claire's parameter (β) have been estimated, as mentioned in detail in the latter part of this section.

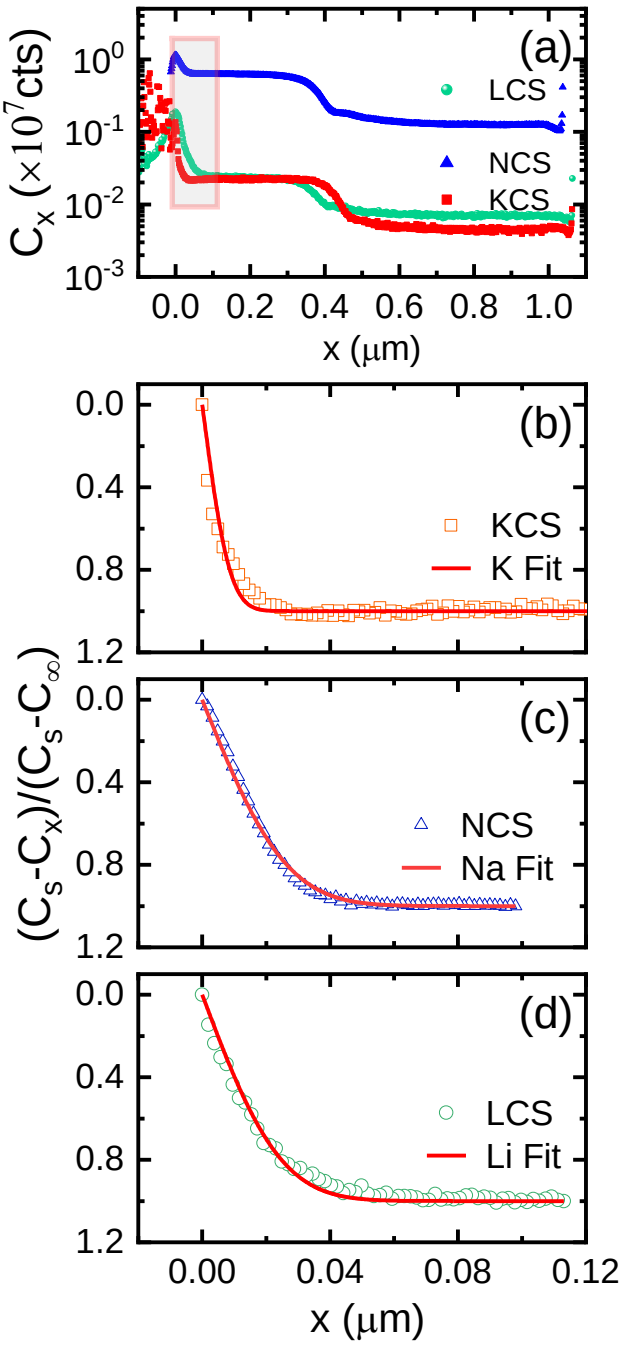

***Figure 6.7**: (a) Raw SIMS profile of Li, Na and K in LCS, NCS and KCS glasses. The portion of the curves outlined in (a) is fitted using Eq. 6.4 for (b) KCS, (c) NCS, and (d) LCS glasses, respectively.*

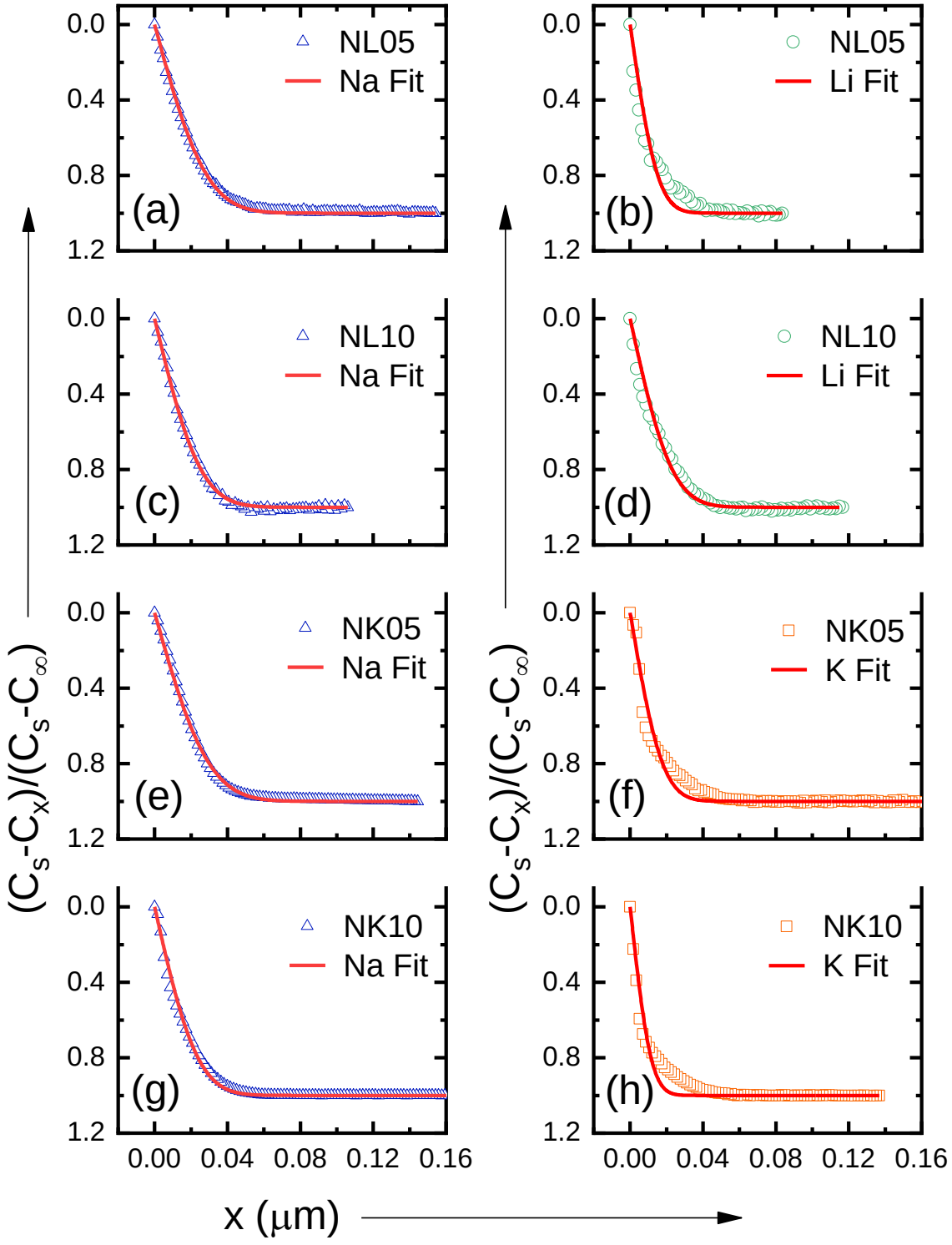

***Figure 6.8**: Error function **(Eq. 6.4)** fitted profiles of (a,c) Na and (b,d) Li for NL05 and NL10 glass substrates, respectively; and (e,g) Na and (f,h) K for NK05 and NK10 glass substrates, respectively.*

On the other hand, the grain boundary diffusion in region II **(Fig. 6.6)** is estimated from Whipple's analysis for a constant source of impurity ions.[191,221] The grain boundary

diffusion coefficient was calculated from the slope of the *ln(I)* versus $x^{6/5}$ curve **(Fig 6.9)** using the formula given by

$$s\delta D_b = 1.322 \times \left(\frac{\partial ln C_x}{\partial x^{\frac{6}{5}}}\right)^{-\frac{5}{3}} \sqrt{\frac{D_L}{t}} \qquad (6.5)$$

where, *'C_x'* is the intensity of the diffusing ion obtained from SIMS at a depth *'x'* from the source; D_b corresponds to the grain boundary diffusion coefficient; δ is the width of the grain boundary (~0.5 nm)[191]; s is the segregation factor corresponding to impurity segregation at the grain boundaries. It is difficult to obtain a segregation factor in the present study, so the triple product ($s\delta D_b$) is obtained to give an estimate of the grain boundary diffusion coefficient. The triple product was obtained from **Eq. 6.5** for alkali ions diffusing from respective substrates is given in **Table 6.1**. Generally, faster the lattice diffusion faster is the diffusion through grain boundaries. However, in the case of impurity diffusion, if grain boundary segregation factor (s) is higher, the grain boundary diffusion is inhibited.[191] Therefore, as seen from the table, the triple product does not follow a fixed trend as obtained for D_L. The grain boundary diffusion is expected to pave the way for the ions to pass through the film towards the surface.

It may be noted that the presence of mixed alkali ions at the interfaces may also affect the rate of diffusion of alkali ions. The Gaussian peak in the raw SIMS profile of alkali ions indicates the segregation of ions at the glass/Mo interface **(Fig. 6.10)**.[222] The area under the Gaussian peak reportedly indicates the interfacial excess ion concentration (Z*) **(Fig. 6.10).**[223]

The values of Z* obtained from the fitting of alkali ion profiles from respective glass substrates are tabulated in **Table 6.1**. The values of Z* are in agreement with the D_L values. The higher the interfacial excess of alkali ion in the interfacial realm, the larger is the lattice diffusion coefficient indicating faster diffusion. From Fick's law, it is well

known that the higher the concentration gradient of diffusing species, the faster is the rate of diffusion.

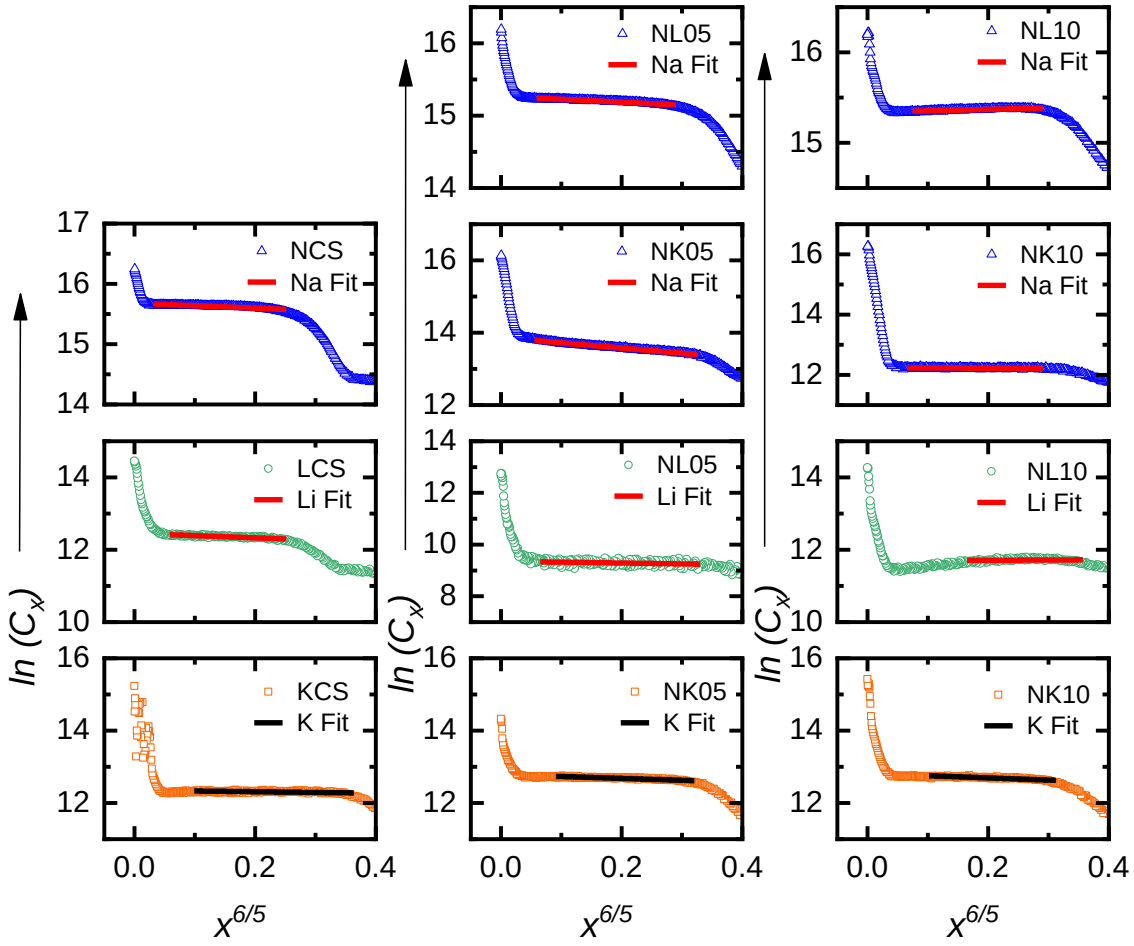

***Figure 6.9**: Fitting (via Eq. (6.5)) of grain boundary diffusion region for Na, Li, and K ions for respective glass substrates.*

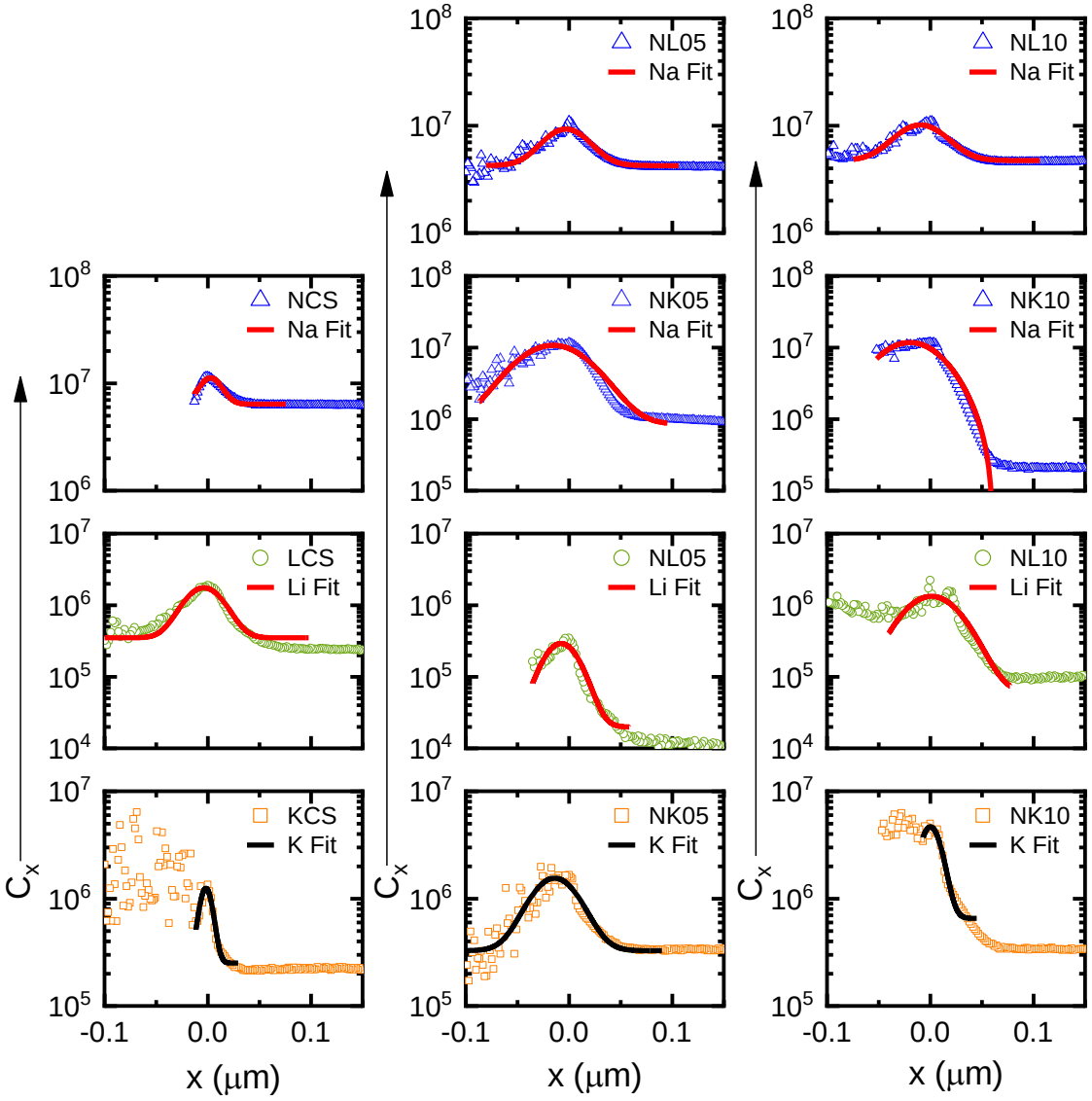

***Figure 6.10**: Interfacial region between substrate and Mo-film showing Gauss' fitting of Na, Li and K depth profiles from respective glass substrates.*

Table 6.1**: Diffusion coefficient (**D_L**) with adj. R^2 values, diffusion length (**d**), grain boundary diffusion triple product (**$s\delta D_b$**), Le-Claire's parameter (**β**) and interfacial excess ion (**Z) for different glass substrates.*

Sample ID	Alkali Ion Profile	D_L (cm^2/s) ($\times 10^{-16}$)	Adj. R^2	d (nm)	$s\delta D_b$ ($\times 10^{-17}$)	β ($\times 10^4$)	Z* ($\times 10^5$)
LCS	Li	5.18	0.9835	13.65	1.25	8.86	0.59
NCS	Na	5.83	0.9963	14.48	3.46	2.05	1.28
KCS	K	0.62	0.9382	4.75	10.63	178	0.14
NL05	Na	6.99	0.9980	15.86	2.71	1.22	2.46
	Li	1.95	0.9187	8.37	0.94	2.88	0.11
NL10	Na	5.48	0.9980	14.04	2.78	15.20	2.83
	Li	4.53	0.9799	12.77	2.39	2.07	0.27
NK05	Na	7.60	0.9978	16.54	0.31	0.12	7.44
	K	2.70	0.9584	9.89	1.51	12.40	0.64
NK10	Na	4.78	0.9944	13.11	25.80	20.60	5.61
	K	1.11	0.9222	6.32	1.21	8.60	0.97

For the glasses with single alkali ions (i.e., LCS, NCS, and KCS), the parameters tabulated in **Table 6.1** indicate that the lattice diffusion of Na ions was the fastest for the NCS glass substrate followed by Li for LCS and K for KCS glasses. This trend is in agreement with the mobility of alkali ions estimated from the electrical properties of respective glasses **(Chapter 4, section 4.1.8).** Similar trend is observed in alkali silicate glasses by Natrup *et al.*[177] The Na ions that showed higher mobility in the glasses have exhibited higher D_L followed by Li and K- ions, respectively. As per the Anderson-Stuart Model, the activation energy of conduction, and hence diffusion, of Na ions is lower than Li and K ions. Conduction activation energy is a combination of binding energy (E_b) of cation-NBO pair and strains energy corresponding to the elastic strain (E_s) required for

dilating the opening between interstices. The diffusion of Li is inhibited by the higher E_b and K by the higher E_s.[224] The excess concentration at the interfaces (Z*) exhibits a direct correlation with the lattice diffusion coefficient (D_L). The higher the Z*, the faster is the lattice diffusion of ions in the Mo film. This interfacial excess is actually an indication of a higher amount of alkali ions transported to the glass/Mo interface (or glass surface) from the bulk glass. Thus, Na ions are transported by a higher extent compared to Li and K ions. It is also in agreement with the extent of diffusion of respective alkali ions shown in **Fig. 6.4,** for single alkali containing glass substrates. The highest Z* and D_L for NCS glass reveals the highest extent of diffusion compared to LCS and KCS. On the other hand, the grain boundary diffusion triple product ($s\delta D_b$) for NCS was higher than that for LCS, but lower than that obtained for KCS glasses. The higher value of ($s\delta D_b$) for K-ions diffusing from KCS glass may be attributed to the higher segregation of heavier K-ions in the grain boundaries owing to lowest mobility of K- ions **(Table 4.5)**.

However, a different trend is observed in mixed alkali glasses. For the glasses containing 5 mol% Na_2O (i.e., NL05 and NK05), faster lattice diffusivity of Na as indicated by a higher value of D_L was observed for NK05 glass compared to the NL05 glass, whereas a reverse trend is seen for glasses containing 10 mol% Na_2O (i.e., NL10 and NK10). The high D_L for Na ions in NK05 glasses is understood from the fact that K ions having lower mobility occupy states close to the NBOs let Na ions diffuse through the glass to the overlayer at a faster rate. For similar concentration with Li (i.e., NL05 glass), as Li itself has higher mobility, it competes with Na ions, which leads to slower diffusion of Na ions, resulting in a lower value of D_L. Furthermore, as the K (and Li) to Na concentration ratio increases (=2 in NK10 and NL10, respectively), the characteristics of major alkali ion (K/Li) dominate the diffusion process. For the NL series glasses, as the Li concentration increases, the D_L values for Na decrease and as expected, the

diffusivity for Li increased from NL05 to NL10 glass. However, for the NK series glasses with an increase in K concentration, diffusivity for both Na and K decreased. The lower D_L for K in NK10 is due to the lower mobility and higher coordination states of K-ions at higher concentrations. This trend is in agreement with the similar anomaly observed in the transport properties viz. dielectric constant and dc-conductivity of NL and NK series glasses at 500 °C **(Figs. 4.21 and 4.22),** which is attributed to the mixed alkali effect, as discussed in detail in **section 4.2.2**. Thus, it is worth to mention here, that the glass substrate properties critically influence the diffusivity parameters of out-diffusing ions.

Similar to the trend in D_L, a higher Z* was observed for Na ions than Li ions and K-ions for NL series and NK series glass substrates, respectively. Interestingly, Z* for Na ions for NL series glass substrates is lower than for NK series glass substrates. This shows that Na-ions out-diffusing from the bulk of glass is accumulated at the interface to a higher extent in the presence of the K ions than the Li ions. This is supported by the lower field strength and higher coordination of K ions which loosely hold the Na ions in the glass network. This creates a higher concentration gradient between the interface and Mo film, resulting in higher values of D_L, as mentioned above. On the other hand, in the presence of Na ions, K ions have slightly higher Z* as compared to Li ions for NK and NL series glass substrates, respectively. This correctly explains the higher extent of diffusion of K ions in NK glasses than Li ions in NL glasses **(Fig. 6.4).**

The triple product of grain boundary diffusion $s\delta D_b$ and segregation exhibits a reverse trend in mixed alkali glasses. The NK05 glass having the highest D_L value for Na ions showed the lowest value for the triple product. It also showed a high $s\delta D_b$ for K ions, indicating the dominance of segregation phenomenon at the grain boundaries. The segregation of bigger sized K ions in the grain boundaries inhibits the grain boundary diffusion of Na ions, unlike lattice diffusion. However, the smaller sized Li ions are

expected to exhibit lesser segregation in grain boundaries due to Li may occupy some of the regular or interstitial sites in crystalline Mo film, since ionic radii of Li and Mo is comparable, resulting in higher grain boundary diffusion of Na-ions from NL05 glass. In the case of NL10 glass, the mobility of Li and Na ions overpower the segregation phenomenon, resulting in higher D_L and $s\delta D_b$ for the Li ions compared to the K ions. Due to the higher mobility of Li and Na ions, they diffuse faster through grain boundaries, with a probability of lesser segregation.[225] On the other hand, high segregation of Na, as well as K ions in NK10 glass, lowers the triple product, due to which lower extent of Na ion diffusion takes place in NK series glasses than in NL series glasses, as shown in **Fig. 6.2**.

From the diffusion studies of the synthesized glasses, the NCS glass was found to exhibit the highest extent of diffusion of Na ions and low interfacial accumulation. Thus, for comparison, we have fitted the diffusion profiles for the as-deposited and annealed (at 500 °C) Mo thin films on commercially available SLG glass substrates similar to the procedure outlined above. The results are summarized in **Fig. 6.11**. The fitting parameters are compared to those obtained for the NCS glass substrate (discussed in **section 6.3**) and are given in **Table 6.2**.

From **Table 6.2**, it is noted that the Na ions in as-deposited Mo thin film on SLG exhibited lower D_L by an order of magnitude than that on synthesized NCS glass substrates. This suggests faster lattice diffusion for NCS compared to SLG. This is in correlation with the higher interfacial excess ion for NCS than that in the SLG glass, which indicates that the Na ions from NCS glass substrate out-diffused towards interfaces up to a higher extent than from SLG. This is in agreement with the higher mobility of Na ions in NCS glass than in SLG, as discussed in **section 4.1.8.** On the other hand, the grain boundary diffusion remained comparable, suggesting a similar rate of diffusion in the as-deposited Mo overlayer, as expected.

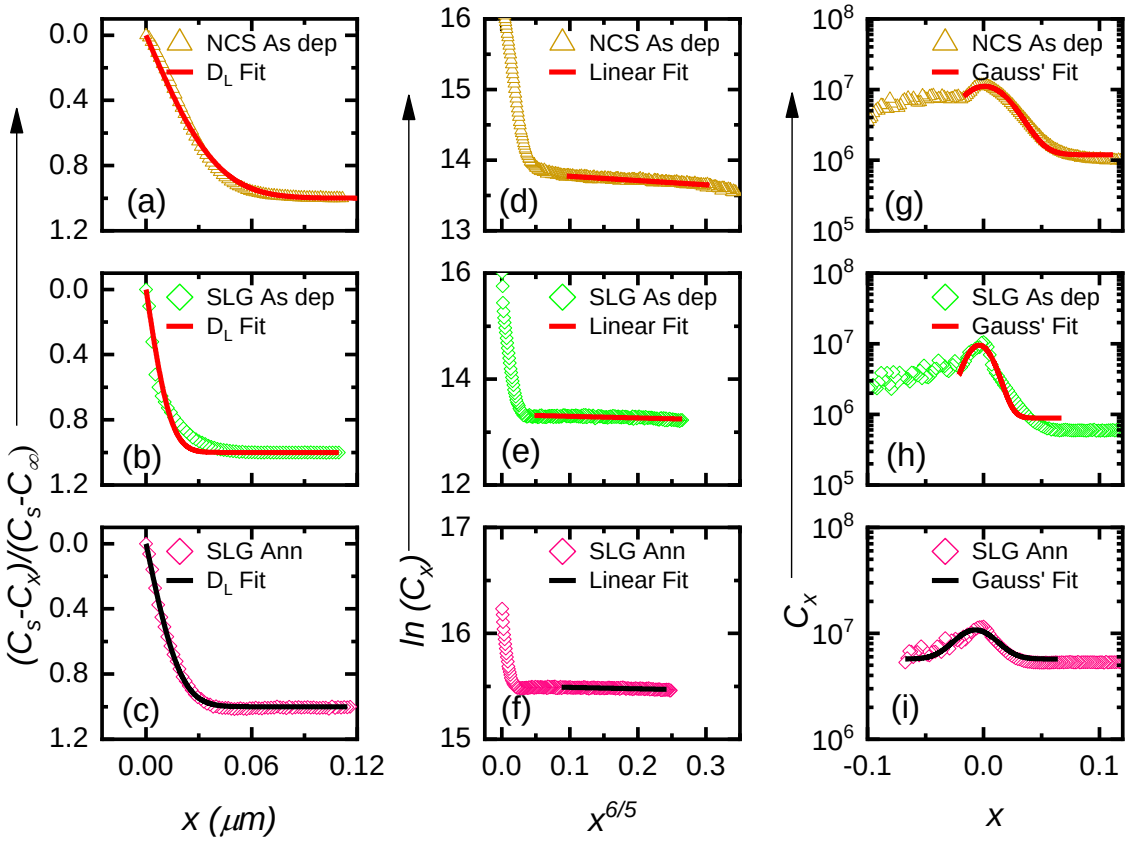

Figure 6.11:(a-c) *Error function fitting (Eq. 6.4) to find D_L;* ***(d-f)*** *Linear fitting using Whipple's analysis (Eq. 6.5);* ***(g-i)*** *Gaussian fitting of the interfacial region of the Na- SIMS profile on NCS As deposited, SLG As deposited and SLG Annealed glass substrates, respectively.*

Table 6.2*: Diffusion coefficient (D_L) with adj. R^2 values, diffusion length (d), grain boundary diffusion triple product ($s\delta D_b$), Le-Claire's parameter (β) and interfacial excess ion (Z*) for NCS glass and SLG.*

Sample ID (Na profile)	**D_L (cm^2/s) ($\times 10^{-17}$)**	**Adj. R^2**	**d (nm)**	**$s\delta D_b$ ($\times 10^{-18}$)**	**β ($\times 10^5$)**	**Z* ($\times 10^5$)**
SLG As-deposited	0.15	0.9333	7.77	0.18	0.75	2.33
SLG Annealed	33.2	0.9977	10.93	119.0	0.16	1.75
NCS As-deposited	1.24	0.9977	21.2	0.17	0.03	4.90
NCS Annealed	58.3	0.9963	14.48	96.0	5.68	1.28

For the annealed samples, the values of D_L were significantly higher than the as-deposited samples. For example, D_L increased from 1.52 $x10^{-18}$ cm^2/s for as-deposited

SLG to 3.32 x10^{-16} cm^2/s for annealed SLG samples. A similar increase from 1.24 x10^{-17} to 5.83 x10^{-16} cm^2/s in the NCS glasses was observed. These values are comparable to the lattice diffusivity of Cd ions in CIGS thin films.[220] Interestingly, the triple product ($s\delta D_b$) also increased almost by three orders of magnitude. This shows that high temperature treatment facilitated grain boundary diffusion.

However, the decrease in Z* on annealing indicated that the Na ions accumulated at the interfaces in the as-deposited sample diffused through lattice and grain boundaries at a faster rate, resulting in lowering the concentration of Na ions at interfaces. Thus, higher diffusion in annealed NCS glass substrate has a lower Z* than annealed SLG substrate. This is in agreement with the higher extent of Na-ion diffusion from NCS than SLG glasses showed previously in **Fig. 6.5.**

The complete mechanism of diffusion of alkali ions from glass substrate to Mo-thin films is understood from the lattice diffusion coefficient (D_L), triple product ($s\delta D_b$) corresponding to grain boundary diffusion and Z*. The diffusion length (d) and LeClaire's parameter (β) were estimated[191] using the following equations:

$$\boldsymbol{d = \sqrt{D_L t}} \qquad \textbf{(6.6)}$$

$$\boldsymbol{\beta = \frac{s\delta D_b}{2D_L(D_L t)^{1/2}}} \qquad \textbf{(6.7)}$$

The significance of '*d*' is correlated with the spacing between the grain boundaries or indirectly with the grain size. The grain size for the optimized Mo films deposited in these samples was found to be ~16 nm as obtained from the XRD analysis given in the previous chapter **(Table 5.1)** and grain boundary width (δ) of the order of inter-atomic distance is assumed as 0.5 nm.[191,221] The values for 'd' and 'β' obtained from the fitting parameters are such that:

$$\boldsymbol{\delta \leq d \leq Grain\ size} \qquad \textbf{(6.8)}$$

$$\boldsymbol{\beta \gg 10} \qquad \textbf{(6.9)}$$

The obtained values satisfy the condition for Harrison's type B kinetic regime for diffusion,[226] where the maximum extent of diffusion of impurity ions takes place through grain boundaries within the metals.[191]

The parameter 'β' determines the extent of grain boundary diffusion to the lattice diffusion. If 'β'>>1, the lattice diffusion depth is much smaller than the penetration depth along the grain boundaries.[227] The smaller the β, the diffusion approaches Harrison's type A regime of diffusion where most of the diffusion takes place in the bulk and not in the grain boundaries. This happens mostly at very high annealing temperatures and extremely long annealing durations.

In summary, the out-diffusion of Li, Na, and K ions from the composition tuned glass substrates to the Mo overlayer has been studied from a detailed analysis of the SIMS data. The lattice diffusion parameter was interpreted from the solution of Fick's second law of diffusion, while the grain boundary diffusion was estimated from Whipple's analysis. The values of the parameters indicate Harrison's B type kinetic regime of diffusion of alkali ions from the substrate to the Mo thin films via grain boundaries. The values of lattice diffusion, an estimate of grain boundary diffusion, and interfacial excess were found to be highly influenced by the composition of the substrate in terms of the nature and amount of the modifier ions in the glass. Lastly, the NCS glass containing Na ions exhibited the highest alkali ion diffusion among all glasses synthesized and was higher than the commercial SLG glass. Thus, the synthesized NCS glass is proposed as a better choice for substrate in the study of CZTS/CIGS based thin film solar cells due to its physical properties as well as due to enhanced Na out-diffusion in it.

Chapter 7 Conclusion and future scope

7.1. Conclusion

This chapter contains the major conclusions of the present research work. The future scope of studies evolved from this work is also given in brief.

Composition tuned glasses with varying amounts of alkali oxides have been synthesized via melt-quench technique. The physical parameters, thermal, mechanical, optical, and electrical properties of the synthesized glasses were examined to determine the suitability of the glasses as substrate materials for CIGS/CZTS based-thin film solar cells. In addition to this, a systematic study is carried out to investigate the effect of Li, Na, and K, individually and in combination (mixed alkali effect), on the out-diffusion of alkali ions (which is highly desired for thin films solar cells) from these glass substrates to Mo-overlayer.

Table 7.1: *Properties of synthesized glasses along with commercially available soda lime glass.*

Sample ID	**Density [g cm^{-3}] ±0.005**	**Hardness [GPa]**	**ε' (at 1 MHz)**	**σ_{dc} (at 500°C) (×10^{-4}) [S/m]**	***E_a [eV]***	***TEC* [ppm/K]**	***T_g* [°C]**
NCS	2.55	5.06±0.20	33.5	77.2	1.09	9.38	563
NL05	2.56	6.65±0.15	20.6	1.8	1.23	9.61	495
NL10	2.55	6.73±0.18	29.5	3.71	1.39	9.44	511
LCS	2.56	6.51±0.22	24.1	75.5	1.27	9.60	533
NK05	2.52	5.76±0.18	34	7.63	1.39	8.60	542
NK10	2.51	5.47±0.22	24	1.08	1.46	9.58	572
KCS	2.50	5.43±0.20	23.5	1.43	1.42	10.02	574
SLG	2.53	5.63±0.22	10	5.39	1.19	9.00	542

The individual effect of Li, Na, and K ions present in the glasses is studied in light of the structure-property correlation in the glasses. Further, the variation in properties of glasses arising with the co-existence of two types of alkali ions viz Na with Li and Na

with K was investigated in NL and NK series glass substrates. The properties of the synthesized glasses were compared to those of commercially available soda lime glass (SLG). The characteristic properties of the synthesized glasses in comparison to commercial SLG are tabulated in **Table 7.1**.

The major conclusions drawn from the study of structure-property correlation of the synthesized glasses are as follows:

- The presence of trigonal and tetrahedral borate and different silicate structural units in the synthesized glasses exhibited a more disordered glass structure as compared to the commercial SLG consisting of silicate structural units only. Moreover, the presence of B_2O_3 enhances compactness in glass structural units.
- Higher field strength and higher binding energy of modifier ions with NBOs significantly increase the packing density of structural units of glasses, which increases the hardness of the glasses.
- Thermal activation of modifier ions at higher temperatures alters the trend in dielectric constant and conductivity of glasses, in turn changing the transport properties like diffusivity.
- The non-linearity in the properties were influenced by the mixed modifier effect in glasses.
- Both Li (in LCS glass) and Na ion (in NCS glass) diffusion take place to a significant extent, but K ions had very low diffusivity in the Mo layer.
- In contrast to the reported size dependent transport mechanism of the ions, we showed that the activation energy and the presence of Ca ions as additional modifiers play a crucial role in the transport properties of the alkali ions in the present glasses.

- The glass transition temperature and thermal expansion coefficient of the synthesized glasses are in the desired range exhibiting suitability as a substrate in thin film solar cells.

To study the feasibility of synthesized glasses as substrates for thin film solar cells, we fabricated a crack-free, well-adherent, and high conductivity bilayer structured Mo film for potential application as a back electrode in CZTS thin film solar cells. By carrying out a comparative study, the effects of the thickness of bilayers and the sputter power on the microstructure and electrical property of the Mo films were elucidated. We found that the deposition at relatively higher pressure followed by low pressure yielded films with simultaneously improved electrical conductivity and adhesion to the substrate compared to those grown with constant pressure. This work is expected to serve as a guideline of optimized deposition conditions by DC magnetron sputtering for Mo back contact layer for the CZTS based thin film solar cells.

Considering the critical requirement of out-diffusion of alkali ions into the over layers in thin film photovoltaic technology, we have investigated the limiting factors for out-diffusion of these ions onto the Mo-overlayer. The diffusion profile for the alkali ions was established using the SIMS results. The qualitative analysis of SIMS data revealed that the bottom layer deposited at higher pressure acts as a reservoir for Na ions in its voids/cracks, owing to its cracked/porous morphology, which however is beneficial for the CZTS solar cells. The diffusion of alkali ions into the sputter-deposited Mo overlayer is revealed to have a complex dependence on the composition and the local glass structure. The Na ions exhibited the highest extent of diffusion among the alkali ions present in glass substrates, while that for the K-ions was the lowest. For the glasses with mixed alkali ions, the presence of Li facilitated the out-diffusion of Na, whereas K ions appear to inhibit the same. Typically, a stronger alkali ion-non bridging oxygen bond

limits the overall diffusion profile of the alkali ion into the Mo overlayer as depicted in the schematic given in **Fig. 7.1**:

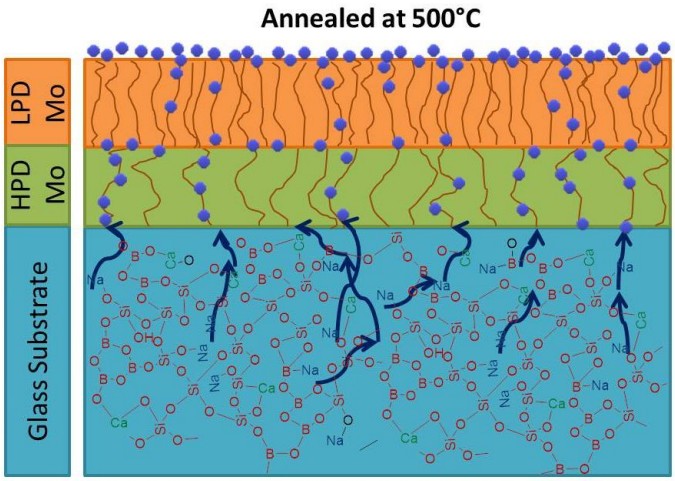

Figure 7.1: *Schematic diagram depicting the diffusion of Na ions from substrate toe overlayers*

The alkali ion diffusion profile obtained from SIMS was fitted using an error function solution of Fick's second law of diffusion to evaluate the lattice diffusion coefficient. Alongside, grain boundaries, as well as interfacial characteristics of the diffusion profiles, were also established. The mechanism of alkali ion diffusion was found to obey Harrison's type B kinetic regime of diffusion for all the samples. Lastly, the comparative study of synthesized NCS and commercial SLG glass substrate showed that the synthesized NCS glass substrate containing Na-ions exhibited higher alkali ion diffusion. Thus, the synthesized NCS glass is proposed as a better choice for substrate in the CZTS/CIGS based thin film solar cells in terms of substrate properties as well as with the facilitation of a higher extent of Na out-diffusion.

7.2. Future scope

Since the synthesized glass substrates are found suitable in all regards as a substrate for CIGS/CZTS based thin film solar cells, in the future the following studies can be carried out:

- Effect of substrate composition on the CIGS/CZTS absorber layer characteristics influenced by the out-diffusion of alkali ions from the substrate.
- Comparative study of the efficiency of thin film solar cells deposited on synthesized glass substrates with commercially available SLG.
- Also, the composition of the substrate glass can be further varied to change their characteristic temperature and their effect on alkali ions diffusivity in the Mo layer.
- Electron scattering measurement can be performed to know about the homogeneity and distribution of different structural units.
- Anderson-Stuart model can be applied to validate the experimental mechanical properties of the present glass substrates.

References

[1] R. K. Brow, M. L. Schmitt, *J. Eur. Ceram. Soc.* **2009**, *29*, 1193.

[2] E. Axinte, *Mater. Des.* **2011**, *32*, 1717.

[3] G. Kaur, O. P. Pandey, K. Singh, D. Homa, B. Scott, G. Pickrell, *J. Biomed. Mater. Res. - Part A* **2014**, *102*, 254.

[4] G. Sharma, M. Kaur, S. Punj, K. Singh, *Biofuels, Bioprod. Biorefining* **2020**, *14*, 673.

[5] J. E. Shelby, *Introduction to Glass Science and Technology*, New York, **1999**.

[6] A. K. Varshneya, *Fundamentals of Inorganic Glasses*, Harcourt Brace & Company, New York, **1994**.

[7] W. D. Kingery, H. K. Bowen, D. R. Uhlmann, *Introduction to Ceramics (2nd Edition)*, New York, **1976**.

[8] G. Kaur, O. P. Pandey, K. Singh, *J. Non. Cryst. Solids* **2012**, *358*, 2589.

[9] M. K. Mahapatra, K. Lu, *J. Power Sources* **2010**, *195*, 7129.

[10] N. Bansal, G. Kaur, K. Singh, *Mater. Res. Bull.* **2018**, *98*, 34.

[11] S. Khan, G. Kaur, K. Singh, *Ceram. Int.* **2017**, *43*, 722.

[12] S. Singh, K. Singh, *J. Non. Cryst. Solids* **2014**, *386*, 100.

[13] N. Bansal, B. C. Mohanty, K. Singh, *J. Alloys Compd.* **2020**, *819*, 152984.

[14] R. Gy, *Mater. Sci. Eng. B Solid-State Mater. Adv. Technol.* **2008**, *149*, 159.

[15] J. Kjeldsen, M. M. Smedskjaer, J. C. Mauro, Y. Yue, *Appl. Phys. Lett.* **2014**, *104*.

[16] K. F. Frederiksen, K. Januchta, N. Mascaraque, R. E. Youngman, M. Bauchy, S. J. Rzoska, M. Bockowski, M. M. Smedskjaer, *J. Phys. Chem. B* **2018**, *122*, 6287.

[17] M. M. Smedskjaer, M. Jensen, Y. Yue, *J. Non. Cryst. Solids* **2010**, *356*, 893.

[18] N. Kaur, G. Kaur, D. Kumar, K. Singh, *J. Phys. Chem. Solids* **2018**, *118*, 248.

[19] S. Seidel, C. Patzig, W. Wisniewski, A. Gawronski, Y. Hu, T. Höche, C. Rüssel,

Sci. Rep. **2016**, *6*, 34965.

[20] J. Fournier, J. Néauport, P. Grua, V. Jubera, E. Fargin, D. Talaga, S. Jouannigot, *Phys. Procedia* **2010**, *8*, 39.

[21] T. Prabhakar, N. Jampana, *Sol. Energy Mater. Sol. Cells* **2011**, *95*, 1001.

[22] K. Singh, *Trans. Indian Ceram. Soc.* **2012**, *71*, 203.

[23] Y. S. Chou, J. P. Choi, J. W. Stevenson, *Int. J. Hydrogen Energy* **2012**, *37*, 18372.

[24] P. M. P. Salomé, H. Rodriguez-Alvarez, S. Sadewasser, *Sol. Energy Mater. Sol. Cells* **2015**, *143*, 9.

[25] N. Murakami, K. Moriwaki, M. Nangu, T. Ohgoh, S. Yuuya, S. Ishizuka, S. Niki, *Conf. Rec. IEEE Photovolt. Spec. Conf.* **2011**, 001310.

[26] M. Nogami, R. Nagao, C. Wong, *J. Phys. Chem. B* **1998**, *102*, 5772.

[27] R. Prasada Rao, T. D. Tho, S. Adams, *Solid State Ionics* **2011**, *192*, 25.

[28] K. Funke, *Solid State Ionics* **2002**, *105*, 195.

[29] S. Khan, G. Kaur, K. Singh, *Ceram. Int.* **2017**, *43*, 722.

[30] N. Kaur, G. Kaur, S. Khan, K. Singh, *Ionics (Kiel).* **2018**, *24*, 2343.

[31] M. Poulain, *Thermochim. Acta* **1996**, *280–281*, 343.

[32] D. Ghosh, K. Biswas, S. Balaji, K. Annapurna, *J. Lumin.* **2017**, *183*, 143.

[33] O. B. Ajayi, M. S. Akanni, J. N. Lambi, C. Jeynes, J. F. Watts, *Thin Solid Films* **1990**, *185*, 123.

[34] G. Sharma, S. K. Arya, K. Singh, *Ceram. Int.* **2018**, *44*, 947.

[35] D. Caurant, A. Quintas, O. Majérus, T. Charpentier, I. Bardez, *Adv. Mater. Resear* **2008**, *39–40*, 19.

[36] N. Chouard, D. Caurant, O. Majérus, N. Guezi-Hasni, J. L. Dussossoy, R. Baddour-Hadjean, J. P. Pereira-Ramos, *J. Alloys Compd.* **2016**, *671*, 84.

[37] J. R. Jones, *Acta Biomater.* **2013**, *9*, 4457.

[38] L. L. Hench, *J. Mater. Sci. Mater. Med.* **2006**, *17*, 967.

[39] M. Montazerian, E. D. Zanotto, *J. Mater. Sci.* **2017**, *52*, 8695.

[40] M. Kaur, K. Singh, *Mater. Sci. Eng. C* **2019**, *102*, 844.

[41] G. Sharma, K. Singh, *J. Mater. Chem. Phys.* **2020**, *246*, 122754.

[42] S. K. Arya, S. S. Danewalia, K. Singh, *J. Mater. Chem. C* **2016**, *4*, 3328.

[43] G. Kaur, D. Homa, K. Singh, O. P. Pandey, B. Scott, G. Pickrell, *J. Power Sources* **2013**, *242*, 305.

[44] V. Kumar, O. P. Pandey, K. Singh, K. Lu, *Fuel Cells* **2014**, *14*, 635.

[45] P. Jackson, D. Hariskos, R. Wuerz, O. Kiowski, A. Bauer, T. M. Friedlmeier, M. Powalla, *Phys. Status Solidi - Rapid Res. Lett.* **2015**, *9*, 28.

[46] S. R. Kodigala, *Thin Film Solar Cells from Earth Abundant Materials: Growth and Characterization of Cu2(ZnSn)(SSe4) Thin Films and Their Solar Cells*, Elsevier Inc., London, UK, **2013**.

[47] S. Adachi, *Earth-Abundant Materials for Solar Cells:Cu2-II-IV-VI4 Semiconductors*, John Wiley & Sons, Ltd., West Sussex, UK, **2015**.

[48] H. Katagiri, K. Jimbo, S. Yamada, T. Kamimura, W. S. Maw, T. Fukano, T. Ito, T. Motohiro, *Appl. Phys. Express* **2008**, *1*, 0412011.

[49] W. Wang, M. T. Winkler, O. Gunawan, T. Gokmen, T. K. Todorov, Y. Zhu, D. B. Mitzi, *Adv. Energy Mater.* **2014**, *4*, 1.

[50] F. Lahoz, C. Pérez-Rodríguez, S. E. Hernández, I. R. Martín, V. Lavín, U. R. Rodríguez-Mendoza, *Sol. Energy Mater. Sol. Cells* **2011**, *95*, 1671.

[51] M. Dhankhar, O. Pal Singh, V. N. Singh, *Renew. Sustain. Energy Rev.* **2014**, *40*, 214.

[52] P. Reinhard, A. Chirilă, P. Blösch, F. Pianezzi, S. Nishiwaki, S. Buechelers, A. N. Tiwari, *IEEE J. Photovoltaics* **2013**, *3*, 572.

[53] P. Blösch, S. Nishiwaki, L. Kranz, C. M. Fella, F. Pianezzi, T. Jäger, C. Adelhelm, E. Franzke, S. Buecheler, A. N. Tiwari, *Sol. Energy Mater. Sol. Cells* **2014**, *124*, 10.

[54] E. S. Mungan, X. Wang, M. A. Alam, *IEEE J. Photovoltaics* **2013**, *3*, 451.

[55] W. J. Lee, D. H. Cho, J. H. Wi, W. S. Han, Y. D. Chung, J. Park, J. M. Bae, M. H. Cho, *J. Phys. Chem. C* **2015**, *119*, 20231.

[56] S. Ishizuka, A. Yamada, M. M. Islam, H. Shibata, P. Fons, T. Sakurai, K. Akimoto, S. Niki, *J. Appl. Phys.* **2009**, *106*, 034908.

[57] W. Septina, M. Kurihara, S. Ikeda, Y. Nakajima, T. Hirano, Y. Kawasaki, T. Harada, M. Matsumura, *ACS Appl. Mater. Interfaces* **2015**, *7*, 6472.

[58] D. Shin, J. Kim, T. Gershon, R. Mankad, M. Hopstaken, S. Guha, B. T. Ahn, B. Shin, *Sol. Energy Mater. Sol. Cells* **2016**, *157*, 695.

[59] L. E. Oikkonen, M. G. Ganchenkova, A. P. Seitsonen, R. M. Nieminen, *J. Appl. Phys.* **2013**, *114*, 083503.

[60] D. Braunger, D. Hariskos, G. Bilger, U. Rau, H. W. Schock, *Thin Solid Films* **2000**, *361*, 161.

[61] A. Garg, *J. Electrochem. Soc.* **1994**, *141*, 1566.

[62] J. Kiss, T. Gruhn, G. Roma, C. Felser, *J. Phys. Chem. C* **2013**, *117*, 25933.

[63] M. Ruckh, D. Schmid, M. Kaiser, R. Schäffler, T. Walter, H. W. Schock, *Sol. Energy Mater. Sol. Cells* **1996**, *41–42*, 335.

[64] M. Igalson, A. Kubiaczyk, P. Zabierowski, M. Bodegard, K. Granath, *Thin Solid Films* **2001**, *387*, 225.

[65] A. Chirilă, S. Buecheler, F. Pianezzi, P. Bloesch, C. Gretener, A. R. Uhl, C. Fella, L. Kranz, J. Perrenoud, S. Seyrling, R. Verma, S. Nishiwaki, Y. E. Romanyuk, G. Bilger, A. N. Tiwari, *Nat. Mater.* **2011**, *10*, 857.

[66] P. Jackson, D. Hariskos, E. Lotter, S. Paetel, R. Wuerz, R. Menner, W. Wischmann, M. Powalla, *Prog. Photovoltaics Res. Appl.* **2011**, *19*, 894.

[67] J. H. Scofield, A. Duda, D. Albin, B. L. Ballard, P. K. Predecki, *Thin Solid Films* **1995**, *260*, 26.

[68] J. H. Yoon, S. Cho, W. M. Kim, J. K. Park, Y. J. Baik, T. S. Lee, T. Y. Seong, J. H. Jeong, *Sol. Energy Mater. Sol. Cells* **2011**, *95*, 2959.

[69] K. Orgassa, H. W. Schock, J. H. Werner, *Thin Solid Films* **2003**, *431–432*, 387.

[70] W. N. Shafarman, L. Stolt, in *Handb. Photovolt. Sci. Eng.*, **2003**, pp. 567–616.

[71] N. Akçay, N. Akın, B. Cömert, S. Özçelik, *J. Mater. Sci. Mater. Electron.* **2017**, *28*, 399.

[72] W. Li, X. Yan, A. G. Aberle, S. Venkataraj, *Int. J. Photoenergy* **2016**, *2016*, 2124087.

[73] S. A. Pethe, E. Takahashi, A. Kaul, N. G. Dhere, *Sol. Energy Mater. Sol. Cells* **2012**, *100*, 1.

[74] M. Jubault, L. Ribeaucourt, E. Chassaing, G. Renou, D. Lincot, F. Donsanti, *Sol. Energy Mater. Sol. Cells* **2011**, *95*, S26.

[75] Z. H. Li, E. S. Cho, S. J. Kwon, *Appl. Surf. Sci.* **2011**, *257*, 9682.

[76] P. Huang, C. Huang, M. Lin, C. Chou, C. Hsu, C. Kuo, *Int. J. Photoenergy* **2013**, *2013*, 390824.

[77] J. H. Yoon, T. Y. Seong, J. H. Jeong, *Prog. Photovoltaics Res. Appl.* **2013**, *21*, 58.

[78] K. S. Gour, A. K. Yadav, O. P. Singh, V. N. Singh, *Vacuum* **2018**, *154*, 148.

[79] D. Rudmann, A. F. Da Cunha, M. Kaelin, F. Kurdesau, H. Zogg, A. N. Tiwari, G. Bilger, *Appl. Phys. Lett.* **2004**, *84*, 1129.

[80] R. B. Bergmann, J. Kohler, R. Dassow, C. Zaczek, J. Werner, *Phys. Status Solidi Appl. Res.* **1998**, *166*, 587.

[81] E. Rudigier, C. Pietzker, M. Wimbor, I. Luck, J. Klaer, R. Scheer, B. Barcones, T. Jawhari Colin, J. Alvarez-Garcia, A. Perez-Rodriguez, A. Romano-Rodriguez, *Thin Solid Films* **2003**, *431–432*, 110.

[82] A. Chirilă, P. Reinhard, F. Pianezzi, P. Bloesch, A. R. Uhl, C. Fella, L. Kranz, D. Keller, C. Gretener, H. Hagendorfer, D. Jaeger, R. Erni, S. Nishiwaki, S. Buecheler, A. N. Tiwari, *Nat. Mater.* **2013**, *12*, 1107.

[83] J. Hedstrom, H. Ohlsén, M. Bodegard, A. Kylner, L. Stolt, D. Hariskos, M. Ruckh, H. Schock, *Photovolt. Spec. Conf. 1993., Conf. Rec. Twenty Third IEEE* **1993**, 364.

[84] R. Mainz, A. Singh, S. Levcenko, M. Klaus, C. Genzel, K. M. Ryan, T. Unold, *Nat. Commun.* **2014**, *5*, 3133.

[85] H. Nukala, J. L. Johnson, A. Bhatia, E. A. Lund, W. M. Hlaing Oo, M. M. Nowell, L. W. Rieth, M. A. Scarpulla, in *Mater. Res. Soc. Symp.*, **2010**, pp. 1–6.

[86] N. Song, Y. Wang, Y. Hu, Y. Huang, W. Li, S. Huang, X. Hao, *Appl. Phys. Lett.* **2014**, *104*, 092103.

[87] M. Kumar, A. Dubey, N. Adhikari, S. Venkatesan, Q. Qiao, *Energy Environ. Sci.* **2015**, *8*, 3134.

[88] D. H. Kuo, J. P. Hsu, *J. Cryst. Growth* **2013**, *372*, 34.

[89] W. M. Hlaing Oo, J. L. Johnson, A. Bhatia, E. A. Lund, M. M. Nowell, M. A. Scarpulla, *J. Electron. Mater.* **2011**, *40*, 2214.

[90] D. Rudmann, D. Brémaud, A. F. Da Cunha, G. Bilger, A. Strohm, M. Kaelin, H. Zogg, A. N. Tiwari, *Thin Solid Films* **2005**, *480–481*, 55.

[91] S. Kermadi, S. Sali, L. Zougar, M. Boumaour, R. Gunder, S. Schorr, V. Izquierdo-Roca, A. Pérez-Rodríguez, *Sol. Energy* **2018**, *176*, 277.

[92] T. Nakada, D. Iga, H. Ohbo, A. Kunioka, *Japanese J. Appl. Physics, Part 1 Regul. Pap. Short Notes Rev. Pap.* **1997**, *36*, 732.

[93] C. Y. Liu, Z. M. Li, H. Y. Gu, S. Y. Chen, H. Xiang, X. G. Gong, *Adv. Energy Mater.* **2017**, *7*, 1601457.

[94] L. Kronik, D. Cahen, H. W. Schock, *Adv. Mater.* **1998**, *10*, 31.

[95] D. Cahen, R. Noufi, *Sol. Cells* **1991**, *30*, 53.

[96] S. H. Wei, S. B. Zhang, A. Zunger, *J. Appl. Phys.* **1999**, *85*, 7214.

[97] A. Rockett, *Thin Solid Films* **2005**, *480–481*, 2.

[98] P. T. Erslev, J. W. Lee, W. N. Shafarman, J. D. Cohen, *Thin Solid Films* **2009**, *517*, 2277.

[99] J. V. Li, D. Kuciauskas, M. R. Young, I. L. Repins, *Appl. Phys. Lett.* **2013**, *102*, 163905.

[100] M. Bodeg Ård, K. Granath, L. Stolt, *Thin Solid Films* **2000**, *361*, 9.

[101] V. Probst, J. Rimmasch, H. Harms, *Solar Cell with Chalcopyrite Absorber Layer*, **1997**, US 5626688.

[102] P. Jackson, R. Wuerz, D. Hariskos, E. Lotter, W. Witte, M. Powalla, *Phys. Status Solidi - Rapid Res. Lett.* **2016**, *10*, 583.

[103] M. Hartmann, M. Schmidt, A. Jasenek, H. W. Schock, F. Kessler, K. Herz, M. Powalla, *Conf. Rec. IEEE Photovolt. Spec. Conf.* **2000**, *2000-Janua*, 638.

[104] K. H. Ong, R. Agileswari, B. Maniscalco, P. Arnou, C. C. Kumar, J. W. Bowers, M. B. Marsadek, *Int. J. Photoenergy* **2018**, *2018*, 9106269.

[105] K. Herz, A. Eicke, F. Kessler, R. Wächter, M. Powalla, *Thin Solid Films* **2003**, *431–432*, 392.

[106] F. Kessler, D. Rudmann, *Sol. Energy* **2004**, *77*, 685.

[107] W. K. Batchelor, M. E. Beck, R. Huntington, I. L. Repins, A. Rockett, W. N. Shafarman, F. S. Hasoon, J. S. Britt, *Conf. Rec. IEEE Photovolt. Spec. Conf.* **2002**, 716.

[108] C. Y. Shi, Y. Sun, Q. He, F. Y. Li, J. C. Zhao, *Sol. Energy Mater. Sol. Cells* **2009**, *93*, 654.

[109] S. Wiedeman, M. E. Beck, R. Butcher, I. Repins, N. Gomez, B. Joshi, R. G. Wendt, J. S. Britt, *Conf. Rec. IEEE Photovolt. Spec. Conf.* **2002**, 575.

[110] R. Wuerz, A. Eicke, F. Kessler, S. Paetel, S. Efimenko, C. Schlegel, *Sol. Energy Mater. Sol. Cells* **2012**, *100*, 132.

[111] E. Jo, M. G. Gang, H. Shim, M. P. Suryawanshi, U. V. Ghorpade, J. H. Kim, *ACS Appl. Mater. Interfaces* **2019**, *11*, 23118.

[112] L. Sun, H. Shen, H. Huang, A. Raza, Q. Zhao, S. Li, *Ceram. Int.* **2020**, *46*, 1982.

[113] A. N. Tiwari, M. Krejci, F.-J. Haug, H. Zogg, *Prog. Photovoltaics Res. Appl.* **1999**, *7*, 393.

[114] B. M. Başol, V. K. Kapur, C. R. Leidholm, A. Halani, K. Gledhill, *Sol. Energy Mater. Sol. Cells* **1996**, *43*, 93.

[115] P. Reinhard, F. Pianezzi, B. Bissig, A. Chirilə, P. Blösch, S. Nishiwaki, S. Buecheler, A. N. Tiwari, *IEEE J. Photovoltaics* **2015**, *5*, 656.

[116] R. Carron, S. Nishiwaki, T. Feurer, R. Hertwig, E. Avancini, J. Löckinger, S. C. Yang, S. Buecheler, A. N. Tiwari, *Adv. Energy Mater.* **2019**, *9*, 1900408.

[117] F. Kessler, D. Herrmann, M. Powalla, *Thin Solid Films* **2005**, *480–481*, 491.

[118] P. M. P. Salomé, A. Hultqvist, V. Fjällström, M. Edoff, B. Aitken, K. Vaidyanathan, K. Zhang, K. Fuller, C. Kosik Williams, *IEEE J. Photovoltaics* **2013**, *3*, 852.

[119] J. Haarstrich, H. Metzner, M. Oertel, C. Ronning, T. Rissom, C. A. Kaufmann, T. Unold, H. W. Schock, J. Windeln, W. Mannstadt, E. Rudigier-Voigt, *Sol. Energy Mater. Sol. Cells* **2011**, *95*, 1028.

[120] B. Belfore, O. Ayala, T. Ashrafee, G. Rajan, S. Karki, S. Marsillac, *IEEE J.*

Photovoltaics **2019**, *9*, 339.

[121] Y. T. Hsieh, Q. Han, C. Jiang, T. Bin Song, H. Chen, L. Meng, H. Zhou, Y. Yang, *Adv. Energy Mater.* **2016**, *6*, 1502386.

[122] X. Ma, Y. Ma, S. Yang, C. Yang, T. Lin, K. Wang, X. Xiao, *Sol. Energy* **2018**, *173*, 1080.

[123] B. C. Bunker, G. W. Arnold, E. K. Beauchamp, *J. Non. Cryst. Solids* **1983**, *58*, 295.

[124] S. A. MacDonald, C. R. Schardt, D. J. Masiello, J. H. Simmons, *J. Non. Cryst. Solids* **2000**, *275*, 72.

[125] Y. Miura, H. Kusano, T. Nanba, S. Matsumoto, *J. Non. Cryst. Solids* **2001**, *290*, 1.

[126] J. Serra, P. González, S. Liste, C. Serra, S. Chiussi, B. León, M. Pérez-Amor, H. O. Ylänen, M. Hupa, *J. Non. Cryst. Solids* **2003**, *332*, 20.

[127] H. Miyoshi, D. Chen, H. Masui, T. Yazawa, T. Akai, *J. Non. Cryst. Solids* **2004**, *345–346*, 99.

[128] T. Akai, K. Kuraoka, D. Chen, Y. Yamamoto, T. Shirakami, K. Urabe, T. Yazawa, *J. Am. Ceram. Soc.* **2005**, *88*, 2962.

[129] S. H. Lee, K. I. Cho, J. B. Choi, D. W. Shin, *J. Power Sources* **2006**, *162*, 1341.

[130] A. Grandjean, M. Malki, C. Simonnet, *J. Non. Cryst. Solids* **2006**, *352*, 2731.

[131] Z. Wang, Y. Hu, H. Lu, F. Yu, *J. Non. Cryst. Solids* **2008**, *354*, 1128.

[132] G. Padmaja, P. Kistaiah, *J. Phys. Chem. A* **2009**, *113*, 2397.

[133] F. Angeli, O. Villain, S. Schuller, S. Ispas, T. Charpentier, *Geochim. Cosmochim. Acta* **2011**, *75*, 2453.

[134] F. He, C. Ping, Y. Zheng, *Phys. Procedia* **2013**, *48*, 73.

[135] M. N. Svenson, T. K. Bechgaard, S. D. Fuglsang, R. H. Pedersen, A. O. Tjell, M. B. Østergaard, R. E. Youngman, J. C. Mauro, S. J. Rzoska, M. Bockowski, M. M.

Smedskjaer, *Phys. Rev. Appl.* **2014**, *2*, 024006.

[136] P. Jha, K. Singh, *Silicon* **2016**, *8*, 437.

[137] M. Barlet, J. M. Delaye, T. Charpentier, M. Gennisson, D. Bonamy, T. Rouxel, C. L. Rountree, *J. Non. Cryst. Solids* **2015**, *417–418*, 66.

[138] M. Neyret, M. Lenoir, A. Grandjean, N. Massoni, B. Penelon, M. Malki, *J. Non. Cryst. Solids* **2015**, *410*, 74.

[139] S. Singh, G. Kalia, K. Singh, *J. Mol. Struct.* **2015**, *1086*, 239.

[140] S. K. Arya, B. Kaur, G. Kaur, K. Singh, *J. Therm. Anal. Calorim.* **2015**, *120*, 1163.

[141] D. Aboutaleb, B. Safi, *Int. J. Chem. Mol. Eng.* **2015**, *9*, 425.

[142] Y. Tokuda, Y. Takahashi, H. Masai, S. Kaneko, Y. Ueda, S. Fujimura, T. Yoko, *J. Asian Ceram. Soc.* **2015**, *3*, 412.

[143] S. S. Gundale, V. V. Behare, A. V. Deshpande, *Solid State Ionics* **2016**, *298*, 57.

[144] T. K. Bechgaard, A. Goel, R. E. Youngman, J. C. Mauro, S. J. Rzoska, M. Bockowski, L. R. Jensen, M. M. Smedskjaer, *J. Non. Cryst. Solids* **2016**, *441*, 49.

[145] A. Hein, J. Martin, M. Schäfer, K. M. Weitzel, *J. Phys. Chem. C* **2017**, *121*, 3203.

[146] Y. T. Shih, J. H. Jean, *J. Am. Ceram. Soc.* **2017**, *100*, 5482.

[147] C. Mansas, J. M. Delaye, T. Charpentier, F. Bruguier, O. Bouty, B. Penelon, H. Arena, D. Rébiscoul, *J. Phys. Chem. C* **2017**, *121*, 16201.

[148] Y. Onodera, Y. Takimoto, H. Hijiya, T. Taniguchi, S. Urata, S. Inaba, S. Fujita, I. Obayashi, Y. Hiraoka, S. Kohara, *NPG Asia Mater.* **2019**, *11*, 75.

[149] S. W. Martin, R. Christensen, G. Olson, J. Kieffer, W. Wang, *J. Phys. Chem. C* **2019**, *123*, 5853.

[150] S. J. Japari, A. K. Yahya, R. Hisam, *Results Phys.* **2020**, *16*, 102905.

[151] C. D. Wagner, *The NIST X-Ray Photoelectron Spectroscopy (XPS) Database*, Washington DC, **1991**.

[152] A. S. Al-Kabbi, S. K. Tripathi, *J. Nanoeng. Nanomanufacturing* **2016**, *6*, 161.

[153] N. Bansal, G. Kaur, K. Singh, *Mater. Res. Bull.* **2018**, *98*, 34.

[154] A. Quintas, D. Caurant, O. Majérus, T. Charpentier, J.-L. Dussossoy, in *Atalante*, **2008**, pp. 2–5.

[155] P. Jha, K. Singh, *Silicon* **2016**, *8*, 437.

[156] S. Agathopoulos, D. U. Tulyaganov, J. M. G. Ventura, S. Kannan, A. Saranti, M. A. Karakassides, J. M. F. Ferreira, *J. Non. Cryst. Solids* **2006**, *352*, 322.

[157] T. K. Aboud, L. Stoch, M. Toda, *Opt. Appl.* **2005**, *35*, 829.

[158] D. Eniu, C. Gruian, E. Vanea, L. Patcas, V. Simon, *J. Mol. Struct.* **2015**, *1084*, 23.

[159] M. Liu, L. Zhao, Y. Liu, Z. Lan, L. Chang, Y. Li, H. Yu, *J. Mater. Sci. Technol.* **2014**, *30*, 1213.

[160] K. El-Egili, *Phys. B* **2003**, *325*, 340.

[161] P. K. Ojha, S. K. Rath, T. K. Chongdar, N. M. Gokhale, A. R. Kulkarni, *New J. Glas. Ceram.* **2011**, *01*, 21.

[162] E. I. Kamitsos, M. A. Karakassides, G. D. Chryssikos, *J. Phys. Chem.* **1987**, *91*, 1073.

[163] C. I. Merzbacher, W. B. White, *J. Non. Cryst. Solids* **1991**, *130*, 18.

[164] E. M. A. Khalil, F. H. ElBatal, Y. M. Hamdy, H. M. Zidan, M. S. Aziz, A. M. Abdelghany, *Phys. B Condens. Matter* **2010**, *405*, 1294.

[165] M. S. Gaafar, S. Y. Marzouk, *Phys. B Condens. Matter* **2007**, *388*, 294.

[166] M. Park, X. Zhang, M. Chung, G. B. Less, A. M. Sastry, *J. Power Sources* **2010**, *195*, 7904.

[167] R. Sawyer, H. W. Nesbitt, R. A. Secco, *J. Non. Cryst. Solids* **2012**, *358*, 290.

[168] D. A. Hensley, S. H. Garofalini, *Appl. Surf. Sci.* **1994**, *81*, 331.

[169] H. W. Nesbitt, G. M. Bancroft, G. S. Henderson, R. Ho, K. N. Dalby, Y. Huang, Z.

Yan, *J. Non. Cryst. Solids* **2011**, *357*, 170.

[170] D. R. Lide, *CRC Handbook of Chemistry and Physics*, CRC Press, **2003**.

[171] P. Jha, K. Singh, *Ceram. Int.* **2016**, *42*, 436.

[172] P. Jha, S. S. Danewalia, K. Singh, *J. Therm. Anal. Calorim.* **2017**, *128*, 745.

[173] D. Souri, *Meas. J. Int. Meas. Confed.* **2011**, *44*, 1904.

[174] A. Makishima, J. D. Mackenzie, *J. Non. Cryst. Solids* **1973**, *12*, 35.

[175] A. Makishima, J. D. Mackenzie, *J. Non. Cryst. Solids* **1975**, *17*, 147.

[176] B. Kaur, Study of Glass-Steel Interface for Corrosion Resistant Applications, Thapar University, Patiala, **2013**.

[177] F. V. Natrup, H. Bracht, S. Murugavel, B. Roling, *Phys. Chem. Chem. Phys.* **2005**, *7*, 2279.

[178] S. Sachdeva, D. Singh, S. K. Tripathi, *Opt. Mater. (Amst).* **2020**, *101*, 109717.

[179] N. Bansal, K. Pandey, K. Singh, B. C. Mohanty, *Vacuum* **2019**, *161*, 347.

[180] A. Bollero, M. Andrés, C. García, J. De Abajo, M. T. Gutiérrez, *Phys. Status Solidi Appl. Mater. Sci.* **2009**, *206*, 540.

[181] L. Holland, *Br. J. Appl. Phys.* **1958**, *9*, 410.

[182] B. S. Patial, Neha, J. Prakash, R. Kumar, S. K. Tripathi, N. Thakur, *J. Nano-Electron. Phys.* **2013**, *5*, 02019.

[183] A. Munar, A. Andrio, R. Iserte, V. Compañ, *J. Non. Cryst. Solids* **2011**, *357*, 3064.

[184] S. Bhardwaj, J. Paul, S. Chand, K. K. Raina, R. Kumar, *J. Electron. Mater.* **2015**, *44*, 3710.

[185] T. Badapanda, R. Harichandan, S. Nayak, A. Mishra, S. Anwar, *Process. Appl. Ceram.* **2014**, *8*, 145.

[186] P. Lunkenheimer, A. Loidl, *Phys. Rev. Lett.* **2003**, *91*, 17.

[187] W. Schirmacher, *Solid State Ionics* **1988**, *28–30*, 129.

[188] A. K. Varshneya, M. E. Milberg, *J. Am. Ceram. Soc.* **1974**, *57*, 165.

[189] S. S. Vadla, R. Ade, A. R. Kulkarni, N. Venkataramani, *Thin Solid Films* **2018**, *661*, 16.

[190] A. A. Bahgat, M. G. Moustafa, E. E. Shaisha, *J. Mater. Sci. Technol.* **2013**, *29*, 1166.

[191] H. Mehrer, *Diffusion in Solids: Fundamentals, Methods, Materials, DIffusion-Controlled Processes*, Springer Berlin Heidelberg, New York, **2007**.

[192] P. Dash, E. Furman, C. G. Pantano, M. T. Lanagan, *Appl. Phys. Lett.* **2013**, *102*, 082904.

[193] H. Mehrer, A. W. Imre, E. Tanguep-Nijokep, *J. Phys. Conf. Ser.* **2008**, *106*, 012001.

[194] A. R. Kulkarni, H. S. Maiti, A. Paul, *Bull. Mater. Sci.* **1984**, *6*, 201.

[195] D. E. Day, *J. Non. Cryst. Solids* **1976**, *21*, 343.

[196] R. Terai, *J. Non. Cryst. Solids* **1971**, *6*, 180.

[197] P. K. Jha, O. P. Pandey, K. Singh, *J. Non. Cryst. Solids* **2016**, *440*, 76.

[198] G. Kaur, O. P. Pandey, K. Singh, *Phys. Status Solidi Appl. Mater. Sci.* **2012**, *209*, 1231.

[199] G. Kaur, M. Kumar, A. Arora, O. P. Pandey, K. Singh, *J. Non. Cryst. Solids* **2011**, *357*, 858.

[200] J. Habasaki, K. L. Ngai, *Phys. Chem. Chem. Phys.* **2007**, *9*, 4673.

[201] V. Raghavan, *Materials Science and Engineering*, Prentice-Hall Of India Pvt.Ltd, New Delhi, **2011**.

[202] A. N. Cormack, J. Du, *J. Non-Crystalline Solids* **2001**, *283*, 293.

[203] F. Natrup, H. Bracht, C. Martiny, S. Murugavel, B. Roling, *Phys. Chem. Chem. Phys.* **2002**, *4*, 3225.

[204] S.-F. Chen, S.-J. Wang, W.-D. Lee, M.-H. Chen, C.-N. Wei, H.-Y. Y. Bor, *Atlas J. Mater. Sci.* **2015**, *2*, 54.

[205] G. Gordillo, M. Grizalez, L. C. Hernandez, *Sol. Energy Mater. Sol. Cells* **1998**, *51*, 327.

[206] K. Tanaka, M. Oonuki, N. Moritake, H. Uchiki, *Sol. Energy Mater. Sol. Cells* **2009**, *93*, 583.

[207] R. V. Forest, K. Han, E. Eser, J. G. Chen, R. W. Birkmire, in *Conf. Rec. IEEE Photovolt. Spec. Conf.*, IEEE, **2013**, pp. 371–375.

[208] J. O. Isard, *J. Non-Crystalline Solids* **1969**, *1*, 235.

[209] M. Pollak, *Philos. Mag. Part B Phys. Condens. Matter* **1980**, *42*, 781.

[210] B. L. Altshuler, A. G. Aronov, in *Mod. Probl. Condens. Matter Sci.*, USSR, **1985**, pp. 1–153.

[211] J. J. Neeway, S. N. Kerisit, J. Liu, J. Zhang, Z. Zhu, B. J. Riley, J. V. Ryan, *J. Phys. Chem. C* **2016**, *120*, 9374.

[212] P. M. P. Salome, A. Hultqvist, V. Fjallstrom, M. Edoff, B. G. Aitken, K. Zhang, K. Fuller, C. Kosik Williams, *IEEE J. Photovoltaics* **2014**, *4*, 1659.

[213] R. Prasada Rao, T. D. Tho, S. Adams, *Solid State Ionics* **2010**, *181*, 1.

[214] G. Kaur, G. Pickrell, N. Sriranganathan, V. Kumar, D. Homa, *J. Biomed. Mater. Res. - Part B* **2016**, *104B*, 1248.

[215] G. Ara, J. G. Mullen, *Phys. Rev.* **1966**, *143*, 663.

[216] T. F. Soules, R. F. Busbey, *J. Chem. Phys.* **1981**, *75*, 969.

[217] S. H. Hahn, A. C. T. Van Duin, *J. Phys. Chem. C* **2019**, *123*, 15606.

[218] L. Wang, A. K. Tieu, H. Zhu, S. Cui, G. Deng, G. Hai, J. Yang, *J. Phys. Chem. C* **2019**, *123*, 14468.

[219] R. J. Araujo, N. J. Binkowski, F. P. Fehlner, *Alkali Metal Ion Migration Control*,

1996, US5578103.

[220] N. J. Biderman, S. W. Novak, T. Laursen, R. Sundaramoorthy, P. Haldar, J. R. Lloyd, *IEEE J. Photovoltaics* **2015**, *5*, 1497.

[221] M. Matsuda, *Solid State Ionics* **1998**, *111*, 301.

[222] H. S.E., F. A. Stevie, H. Ade, *Macromolecules* **2005**, *38*, 7.

[223] H. S.E., F. A. Stevie, H. Ade, *J. Vac. Sci. Technol. A Vacuum, Surfaces, Film.* **2006**, *24*, 362.

[224] O. L. Anderson, D. A. Stuart, *J. Am. Ceram. Soc.* **1954**, *37*, 573.

[225] Y. Mishin, C. Herzig, *Mater. Sci. Eng. A* **1999**, *260*, 55.

[226] L. G. Harrison, *Trans. Faraday Soc.* **1961**, *57*, 1191.

[227] S. Swaroop, M. Kilo, C. Argirusis, G. Borchardt, A. H. Chokshi, *Acta Mater.* **2005**, *53*, 4975.

[228] O. Ayala, T. Ashrafee, G. Rajan, S. Karki, K. Aryal, V. Ranjan, A. A. Rockett, S. Marsillac, in *2017 IEEE 44th Photovolt. Spec. Conf. PVSC 2017*, **2017**, pp. 1–3.

[229] R. V. Forest, E. Eser, B. E. McCandless, R. W. Birkmire, J. G. Chen, *Am. Inst. Chem. Eng.* **2014**, *60*, 2365.